TERA

NUREG/CR-1398
LA-8301

Evaluation of Techniques for Dynamic Measurement of Fuel Motion in Liquid-Metal-Cooled Fast-Breeder Reactor Safety Experiments

University of California

LOS ALAMOS SCIENTIFIC LABORATORY
Post Office Box 1663 Los Alamos, New Mexico 87545

8101260127

Edited by Nancy Shera

Photocomposition by Cleo H. Gutierrez

NUREG/CR-1398
LA-8301

R7

Evaluation of Techniques for Dynamic Measurement of Fuel Motion in Liquid-Metal-Cooled Fast-Breeder Reactor Safety Experiments

Albert E. Evans
John D. Orndoff*

Manuscript submitted: March 1980
Date published: October 1980

*Consultant. 997-B 48th St., Los Alamos, NM 87544

Prepared for
Division of Reactor Safety Research
Office of Nuclear Regulatory Research
US Nuclear Regulatory Commission

NRC FIN No. A7046

UNITED STATES
DEPARTMENT OF ENERGY
CONTRACT W-7405-ENG. 36

FOREWORD

This report covers work performed in fiscal years 1976-79 under Projects R-283 and R-414, "Review of Safety Test Facilities for Fast Reactors." The work constitutes a portion of Task 3 of this project, "Experiment Diagnostic Systems Evaluation." Work commenced in October 1975 under the direction of John D. Orndoff; upon his retirement in June 1977, the work was continued by Albert E. Evans.

In the spring of 1978, after a decision had been made to defer or cancel plans to build new safety test facilities for liquid-metal-cooled fast-breeder reactors (LMFBRs), the Nuclear Regulatory Commission was directed to cease support of research aimed toward providing design data for such facilities. Accordingly, the program effort was redirected to support development of the upgraded Transient Reactor Test Facility of Idaho National Engineering Laboratory and to provide assistance in the development of coded-aperture fuel-motion monitoring techniques for use at the Annular-Core Research Reactor of Sandia Laboratories, Albuquerque. The redirected program was supported under Program R-414 for the purpose of determining whether presently planned fuel-motion diagnostics techniques for scheduled destructive tests of LMFBR fuel assemblies would produce data adequate for verification of the SIMMER code. Experimental work terminated on September 21, 1979.

CONTENTS

TABLES

EVALUATION OF TECHNIQUES FOR DYNAMIC MEASUREMENT OF FUEL MOTION IN LIQUID-METAL-COOLED FAST-BREEDER REACTOR SAFETY EXPERIMENTS

by

Albert E. Evans and John D. Orndoff

ABSTRACT

The purpose of the Los Alamos Scientific Laboratory program for evaluation of fuel-motion diagnostics instrumentation is to determine whether fuel-motion monitoring techniques for planned liquid-metal-cooled fast-breeder reactor safety tests can yield information adequate for verification of reactor-safety calculations. Neutron and gamma-ray hodoscope scans of fuel assemblies containing from 1 to 127 pins were obtained. It was found that a single-pin void can be detected in fuel assemblies containing up to 127 pins and that, for both 37- and 127-pin fuel assemblies, the image of a single-pin void varies with the depth of the void within the assembly. The effect of a thick steel casing on image quality and the use of in-core detectors as fuel-motion monitors were investigated. It was shown that PARKA is a suitable driver reactor for static testing of coded-aperture fuel-motion monitoring systems. The use of PARKA in a pulsed mode to study transient phenomena in safety tests is discussed.

I. INTRODUCTION

Complete evaluation of the safety of liquid-metal-cooled fast-breeder reactors (LMFBRs) requires facilities where quantities of LMFBR fuel pins, ranging from a single pin to multiple subassemblies containing thousands of pins, can be tested to destruction under conditions simulating those that may exist during a reactor accident. Such tests have already been performed at the Transient Reactor Test Facility (TREAT) of Argonne National Laboratory, located at Idaho National Engineering Laboratory (INEL), on assemblies containing from one to seven pins. This facility is being upgraded to permit tests on assemblies of 19, 37, or 61 pins. Complementary work is also being done at the Engineering Test Reactor of INEL and at the Annular-Core Research Reactor (ACRR) of Sandia Laboratories, Albuquerque (SLA). In addition, requirements have been established for larger facilities[1,2] where destructive tests could be performed on a full subassembly of LMFBR fuel (217 or 271 pins) or on more than one subassembly.

The ability to monitor fuel motion in a disintegrating test assembly is vital to the understanding of the test results and to the verification of reactor-safety calculations with these results. Criteria have been established[3] for the performance of fuel- and clad-motion measurement systems. These criteria are based upon the sensitivity, accuracy, and time and spatial resolution necessary to derive useful information from tests intended to simulate various types of core-disruptive accidents in LMFBRs, and include specifications for field of view, spatial resolution, time duration and resolution, and mass resolution. In general, the requirements vary with the size of the assembly undergoing test. For instance, horizontal spatial resolution requirements vary from 2 mm for tests of a few pins to 50 mm for tests of multiple subassemblies that may contain over 1000 pins. The fuel-motion measurement system will also be required to have a capability for depth measurement comparable to its horizontal resolution and to detect the motion of as little as 0.04 g of fuel in small-bundle tests or of 50 g in multiple-subassembly tests. Time-resolution requirements vary from 0.2 to 100 ms, depending on the type of test.

Since the test assemblies are immersed in liquid sodium, one is constrained to monitor fuel motion with the image formed by neutrons or gamma rays emitted by the assembly or by x-rays transmitted through the assembly. The quality of this image is strongly influenced by scattering and absorption within the test assembly of radiation emitted not only by the test assembly but also by the reactor that drives the test assembly to destruction. The time resolution (the minimum time during which information must be gathered to obtain an image with the required spatial and mass resolution) is limited ultimately by the statistics of radiation emission from the test assembly. In practice, however, time resolution is limited either by the data-acquisition system in the case of radiation-counting system or by mechanical or electronic considerations in the case of photo-imaging systems.

Techniques being applied to or being studied as candidates for fuel- and clad-motion monitoring include flash-x-ray cinematography,[4] single- and multiple-pinhole self radiography,[5] radiography with Fresnel and other coded apertures,[6] use of in-core radiation detector networks,[7] and use of multi-aperture collimating hodoscopes.[8] Acoustical holography has also been considered as a means to monitor fuel motion.[9] The selection of a fuel-motion monitoring system must be done before design of the test facility because the system selected will strongly influence facility requirements.

The purpose of the work described herein was to provide a facility where the applicability of the various proposed fuel-motion monitoring techniques could be determined and where instrumentation could be tested and optimized before installation in full-scale test facilities. The facility has been applied to the study of hodoscopes, coded-aperture imaging systems, and in-core detectors. Some guidance is provided for the future application of these techniques.

II. THE FACILITY

A. PARKA

The PARKA critical assembly at Los Alamos Scientific Laboratory (LASL) has been modified to serve as a driver for arrays of from 1 to 127 highly enriched UO_2 fuel pins representing LMFBR fuel. PARKA is a Rover-Project Kiwi reactor loaded with graphite-uranium fuel elements. These are one-hole bead-loaded hexagonal elements that were used for critical-assembly studies for Rover reactor design. Enriched-uranium (93% ^{235}U) loadings of 100, 200, 300, and 400 kg/m^3 are distributed to give approximately flat fission density across the fueled diameter. Figure 1 is a photograph of the PARKA core with a 37 fuel-pin test assembly at the center. The active core, 0.91 m in diameter by 1.32 m high, is surrounded by a 15-cm-thick beryllium reflector containing 12 rotary beryllium control drums faced on half their circumferences with B_4C. Rotation of the control drums is controlled to the nearest 0.01° by stepping-motor-driven actuators. Control drums may be operated singly or in unison. A differential power-level sensor operates one control drum to maintain a power level constant to within 0.1% during runs lasting several hours.

The control system has a reactivity worth in excess of 9 \$. A shutdown reactivity of −5 \$ is required to assure safe facility operation. If an assembly is to be tested that will cause the reactor to have a shutdown reactivity greater than −5 \$, the reactor is shimmed by the removal of 6.5-mm-diam graphite rods from some of the 10-mm-diam holes in the centers of the fuel elements. Conversely, more graphite rods may be added to the core if the test assembly has negative reactivity.

ONETRAN [10] transport-code calculations have been run for a 37-pin test assembly in the center of PARKA. The 16-group neutron spectra at the center and at the edge of the test assembly are shown in Fig. 2. Figure 3 shows the fission densities at these two positions as functions of the energy of the neutron causing fission. The median energy of neutrons causing fission at the edge of the test assembly is between 0.55 and 3 keV. At the center this shifts to between 3 and 17 keV. These

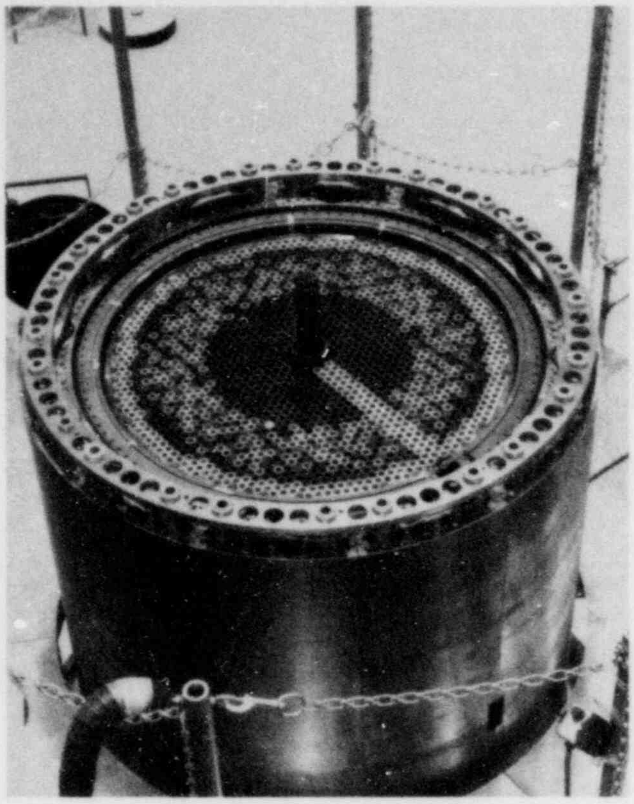

Fig. 1.
Photograph of the top of the PARKA core with a 37-pin LMFBR test assembly at the center. The fuel elements in the light-colored band leading from the center to the lower right of the core have been cut to form a viewing slot. The penetration through the beryllium reflector for this viewing slot can be seen at the lower right of the figure.

figures show that PARKA is an intermediate-spectrum reactor with neutronic characteristics typical of those required of a driver reactor for large-bundle LMFBR safety tests in which a test assembly must be reasonably uniformly irradiated throughout its volume.

In addition to the requirement for uniform irradiation is the requirement that the ratio, referred to as figure of merit (FOM), of minimum fission density in the test specimen to maximum fission density in the driver be large, so that the test specimen can be driven to destruction without harming the driver reactor. A high FOM also improves the signal-to-background (S/B) ratio in fuel-motion diagnostics measurements. A high FOM is obtained by fueling the test object with fully enriched uranium, either as pure metal or oxide, and maintaining a relatively low fuel density (400 kg/m^3 near the center of PARKA) in the driver.

Figure 4 shows the results of a ONETRAN calculation of the fission density for a 37-pin test assembly in PARKA with water, sodium, or void between the pins. Note that water as a filler improves the FOM by a factor of 2, an advantageous situation when only gamma-ray information is desired. For fast-neutron self-imaging of a test assembly, the presence of water would probably be intolerable. For single-pin experiments, it is possible to increase the FOM to as high as 80 with a polyethylene flux trap just outside the test region. It should also be noted that there is very little difference between sodium and void as fillers. Aluminum grid blocks have been used as a substitute for sodium in most of our tests.

Figure 5 shows the radial fission distributions for 37- to 127-pin hexagonal fuel assemblies in the test region of PARKA. These measurements were made by irradiating fresh fuel pins in selected positions as the test assembly was built up from minimum to maximum size. The selected fuel pins were removed and the gross fission-product gamma activity of each pin was compared to the activity of the central pin, which was used as a reference. The results show that variation in power density across a test assembly, although correctable in most cases, will be a factor in interpreting fuel-motion diagnostic data. Graded fuel loading or graded fuel enrichment could be used where a more uniform power density is required in the test assembly. The data shown in Fig. 3 suggest that filtering of low-energy neutrons by inserting a cadmium or boron sleeve around the test section could improve fission-density uniformity within this region.

Consideration has been given to how large a test bundle could be accommodated in PARKA. Fission-density calculations for four subassemblies in PARKA approximate proposed Safety Test Facility (STF) test geometries including appropriate sodium content and stainless steel containers. For this 868-pin array, the fuel was assumed to be highly enriched UO_2.The large self-multiplication of the four subassemblies increases the PARKA system reactivity by 23 \$. The test assembly depresses fissions in the adjacent PARKA fuel by approximately 25%. The FOM is approximately 11, with a peak-to-minimum ratio across the test assembly of 1.33. The 23 \$ of excess reactivity in PARKA can be reduced easily either by enlarging the hole in the hexagonal fuel elements to increase core void fraction or by adding boron-loaded graphite rods near the central hole. Boron should harden the PARKA spectrum to give both a smaller peak-to-minimum variation across the test assembly and an increased FOM.

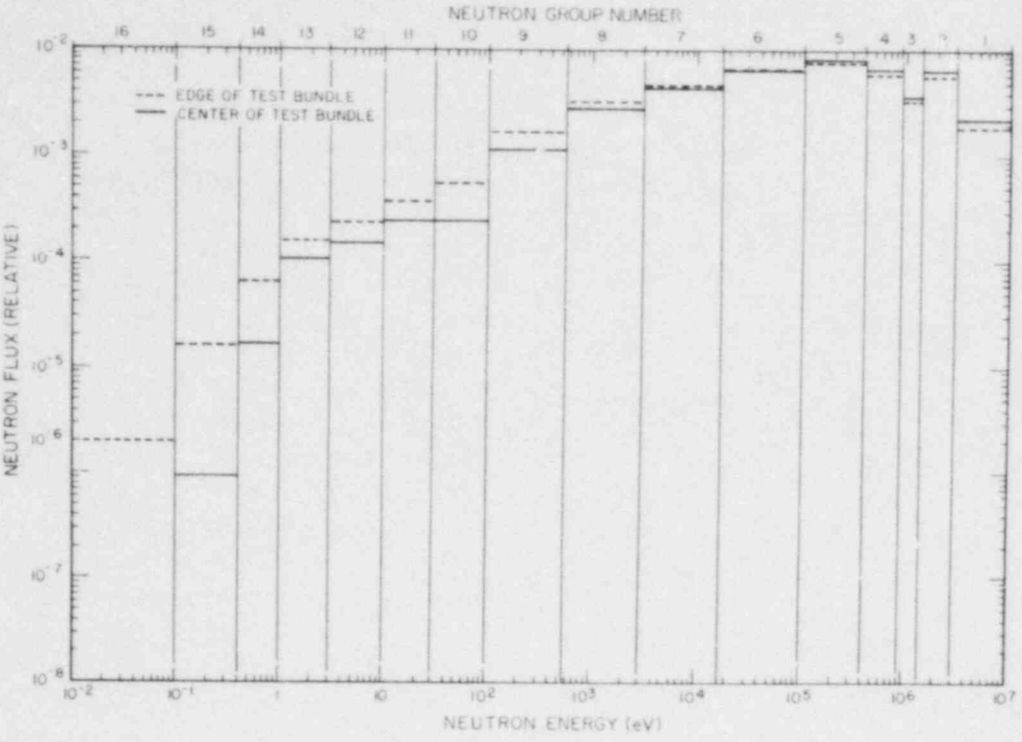

Fig. 2.

Sixteen-group ONETRAN calculation of the neutron spectrum at the center and at the edge of a 37-pin test assembly in PARKA.

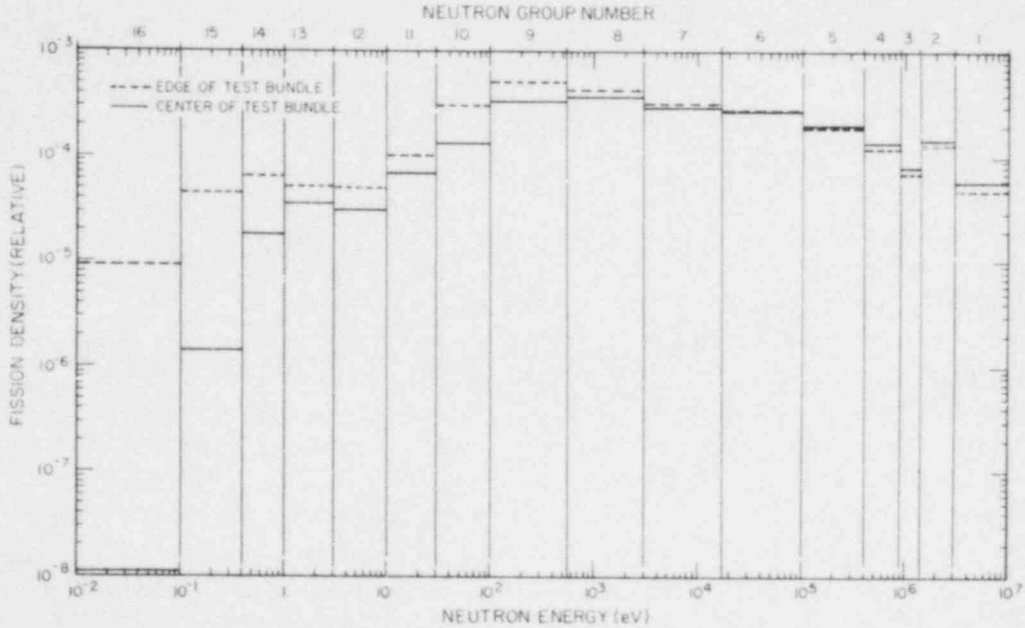

Fig. 3.

Calculated fission density, as a function of the energy of the neutron causing fission, at the center and at the edge of a 37-pin test assembly in PARKA.

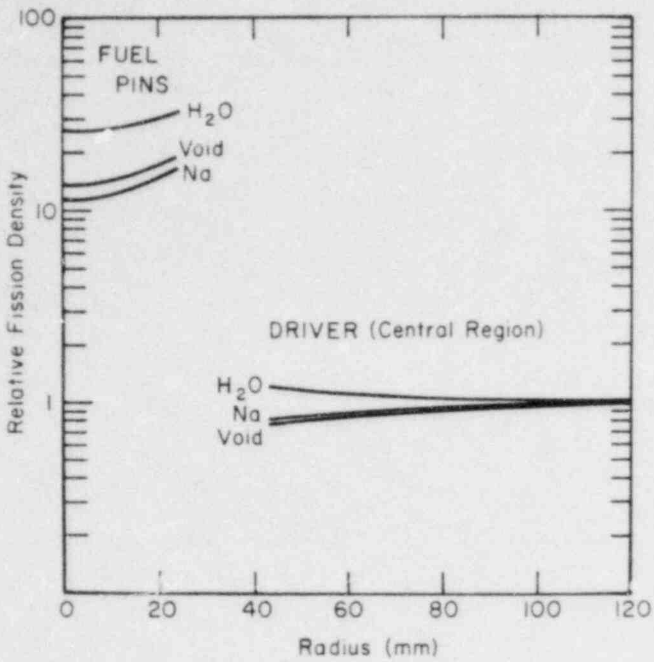

Fig. 4.
Calculated fission density in the test and driver regions for a 37-pin test assembly in PARKA with various fillers.

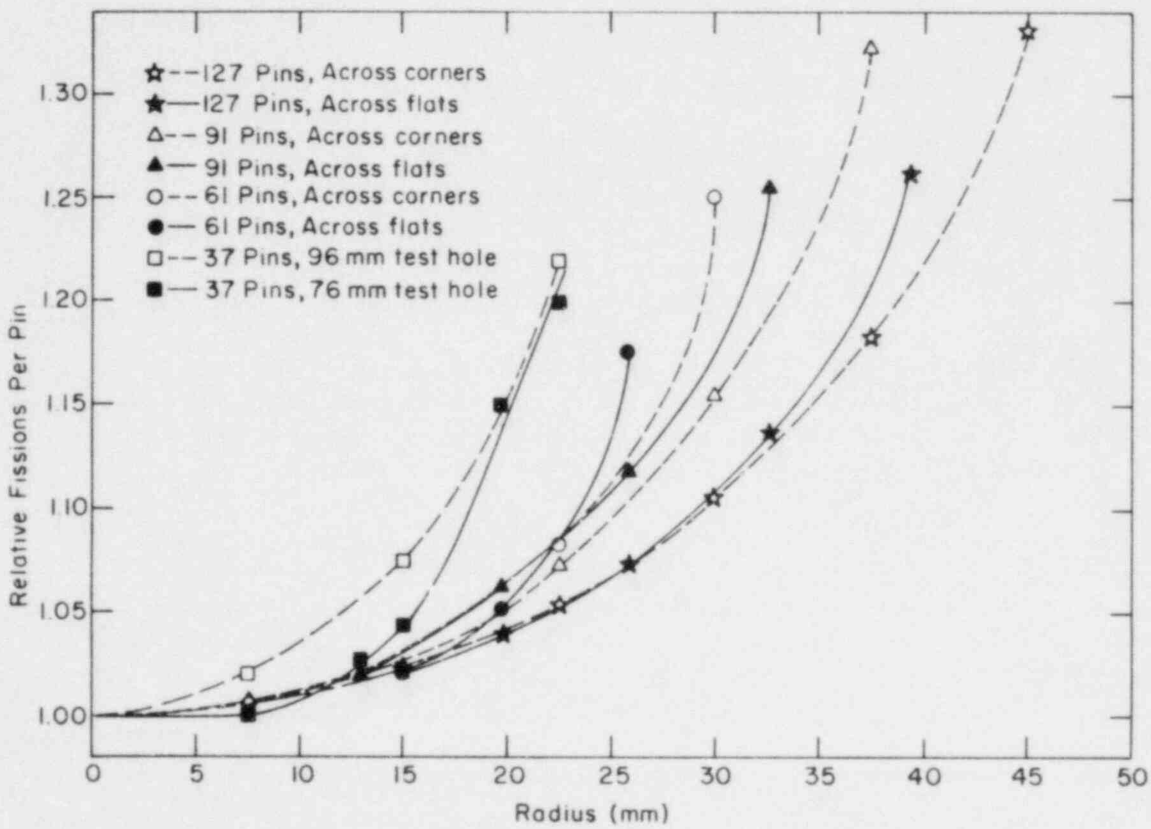

Fig. 5.
Measured fission distributions in various-sized test assemblies in PARKA.

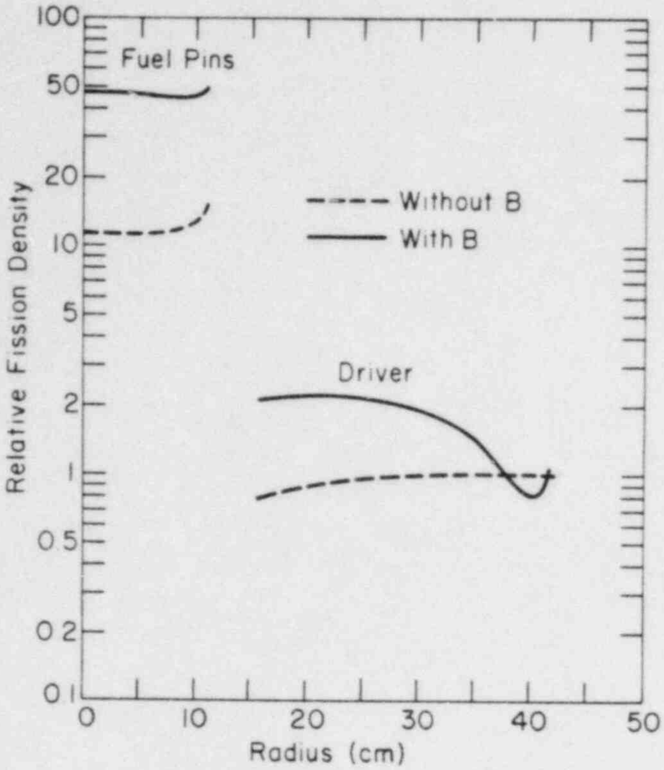

Fig. 6.
Calculated fission density in the test and driver regions for a four-subassembly array in PARKA, without boron and with boron uniformly distributed over the driver region.

This was confirmed by calculations with boron uniformly distributed over the driver portion of the PARKA core. The boron required to reduce the reactivity the required 23 $ is equivalent to 6.3 g per PARKA fuel element. The calculated fission densities with and without boron are shown in Fig. 6. Although the boron poison causes a large perturbation in the driver fission profile, the resulting FOM is approximately 20 and the peak-to-minimum fission ratio in the fuel pins is only 1.10. Maintaining a flat fission-density profile across the driver in PARKA is of no particular concern. It thus appears that PARKA can be adapted to serve as an excellent driver for a four-subassembly array of fuel pins.

Initial measurements on the 37-pin assembly in PARKA show that addition of the UO_2 fuel to the stainless-steel cladding tubes increases reactivity by 1.1 $. The UO_2 length of 0.91 m is centered in the 1.32-m-long PARKA driver fuel. ONETRAN calculations of this geometry predicted a reactivity for the 37 pins of 0.9 $ in a voided test cell and 1.1 $ in a cell filled with sodium.

Reactivity worths of test bundles of various sizes, the PARKA central-region fuel elements, shim rods, and other additions to the reactor that have affected system reactivity are listed in Table I.

Figure 7 shows an overall view of PARKA. It has been necessary to add 12 mm of lead to the sides and 50 mm to the top of the reactor to permit access to the reactor after irradiation.

B. Provisions for Ex-Core Imaging

A 4.4-cm-wide by 10.2-cm-high slot has been cut transversely through the fuel and the beryllium reflector of PARKA to permit viewing the test region with either a hodoscope or a coded-aperture imaging system. Another 4.5-cm-wide by 5-cm-high slot, located in the reflector 30 cm below the primary slot, is available for future experiments.

The reactor is adjacent to an unmortared-concrete-block shielded instrument room. The viewing slot in PARKA is aligned with a stepped hole leading into the shielded area. This hole, 30 cm square at the reactor side and approximately 75 cm square at the inside face of the instrument room, can accommodate a variety of imaging devices. The overall facility layout is shown in Fig. 8. The combination of 75-cm-thick shield-room walls, the 45-cm-thick concrete wall of the critical-assembly bay, and 38 cm of unmortared concrete

TABLE I

REACTIVITY WORTHS OF VARIOUS OBJECTS IN PARKA

Item	Reactivity ($)
Central region PARKA fuel element, 400 kg/m^3 93%-enriched uranium	0.0610
Graphite shim rod, 7-mm diam	0.0060
Empty axial steel shell, 96 mm i.d. by 7.1 mm thick	0.280
Single simulated FFTF fuel pin, 172 g 93%-enriched UO_2 in steel shell	0.0273
Assembly of 37 fuel pins in steel shell	1.300
Assembly of 61 fuel pins in steel shell	2.140
Assembly of 91 fuel pins in steel shell	3.300
Assembly of 127 fuel pins in steel shell	4.980
Lead shield on top of core, 5 cm thick	0.800
Lead shield outside Be reflector, 1.25 cm thick	0.800
91-pin EBR-II assembly, 30 cm long, 5 kg 52%-enriched uranium	0.690
Slot halfway through reflector and core, 102 mm by 44 mm	0.580

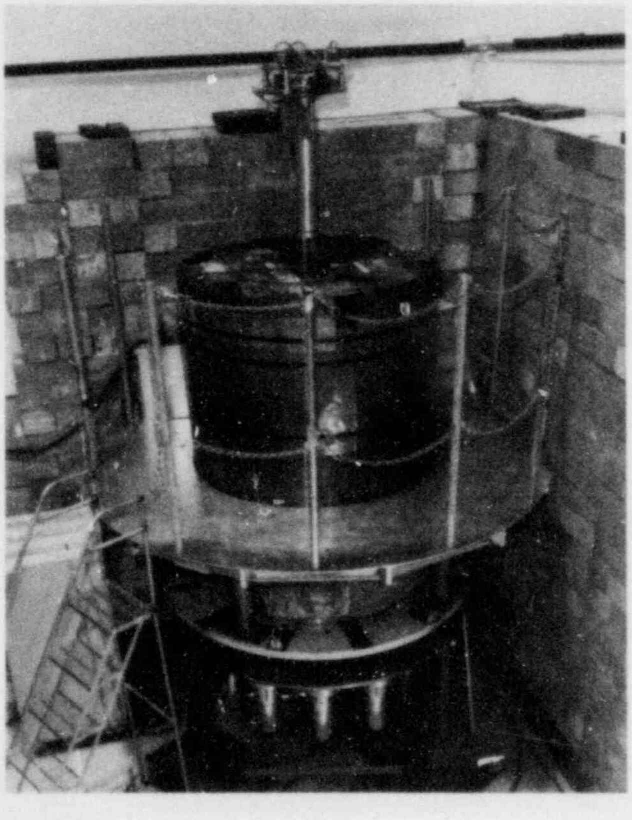

Fig. 7.
View of the PARKA facility set up for evaluation of fuel-motion diagnostics instrumentation. The assembly at the top of the core is an actuator for remote rotation of test assemblies and withdrawal of individual fuel pins. The rotary control-drum actuators can be seen on the underside of the reactor.

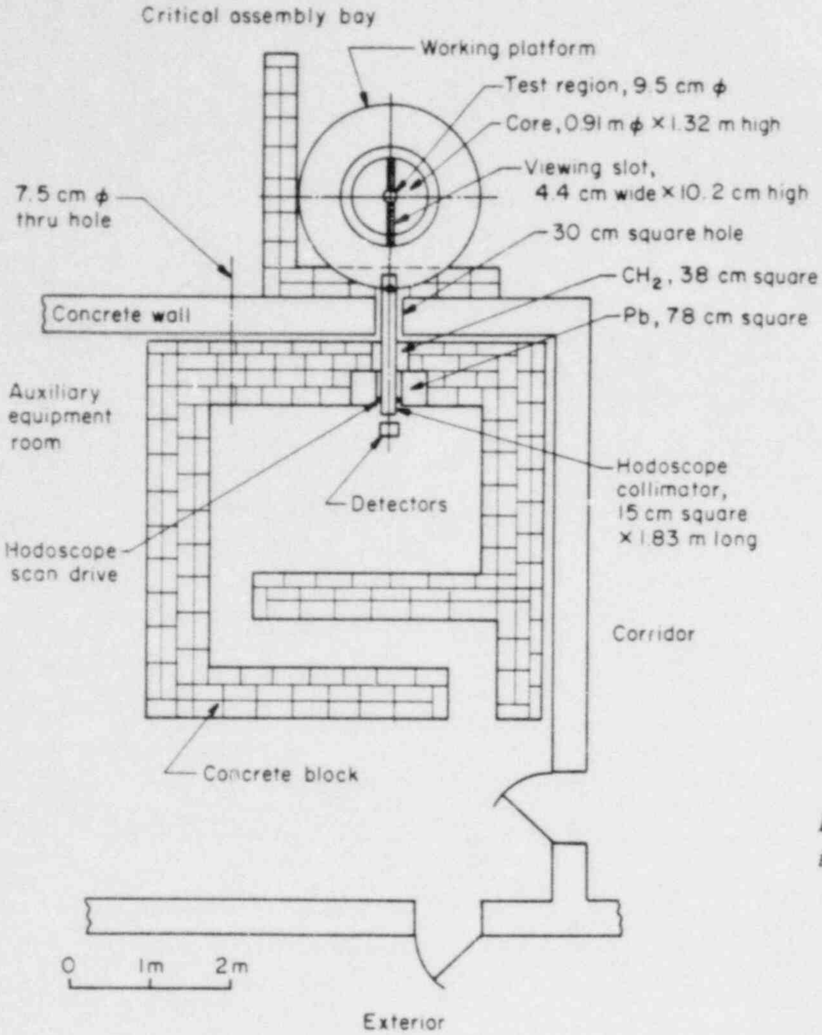

Fig. 8.
Layout of the fuel-motion diagnostics instrumentation evaluation facility.

block stacked between the reactor working platform and the assembly-bay wall provides an attenuation factor in the shield room for PARKA neutrons and gamma rays of approximately 10 000. The shield room has been lined with 25 mm of boron-loaded plaster (Reactor Experiments, Inc. #284) to suppress thermal neutrons.

As shown in Fig. 8, a four-channel steel hodoscope collimator was installed in the large hole in the shield-room wall to view the central portion of the test region in PARKA. This collimator, 15 cm square and 1.83 m long, is a lamination of three 45-mm-thick steel slabs into which the viewing slots have been milled. A photograph of the collimator is shown in Fig. 9.

Details of the collimator and its relationship to the test region are given in Fig. 10. The slots through the collimator are 4.8 mm wide by 12.7 mm high. The front face of the collimator is 0.91 m from the center of the reactor test region.

The field of view of a collimator slot is considered in Fig. 11. If radiation is detected uniformly across the face of a sensor at the collimator exit (a) and if collimation is "perfect," the detector senses radiation uniformly from a field at the object (b) of the same dimensions as the slot, plus a fringing area defined by diagonals across the slot from its entrance (c) to the exit. If θ is the angle between these diagonals and the walls of the slot, d the width of the slot and ℓ its length, we have

$$\tan \theta = d/\ell \quad . \tag{1}$$

If r is the distance of the object plane from the front face of the collimator, then the total width y of the viewing area is given by

$$y = d + 2r \tan \theta = d[1 + (2r/\ell)] \quad . \tag{2}$$

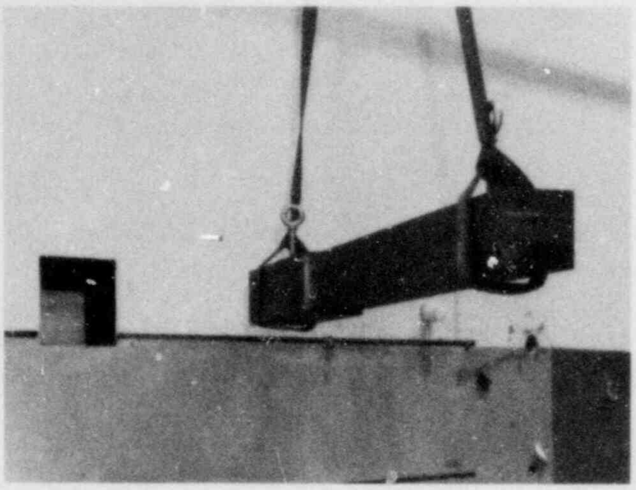

Fig. 9.
Installation of the four-channel hodoscope collimator.

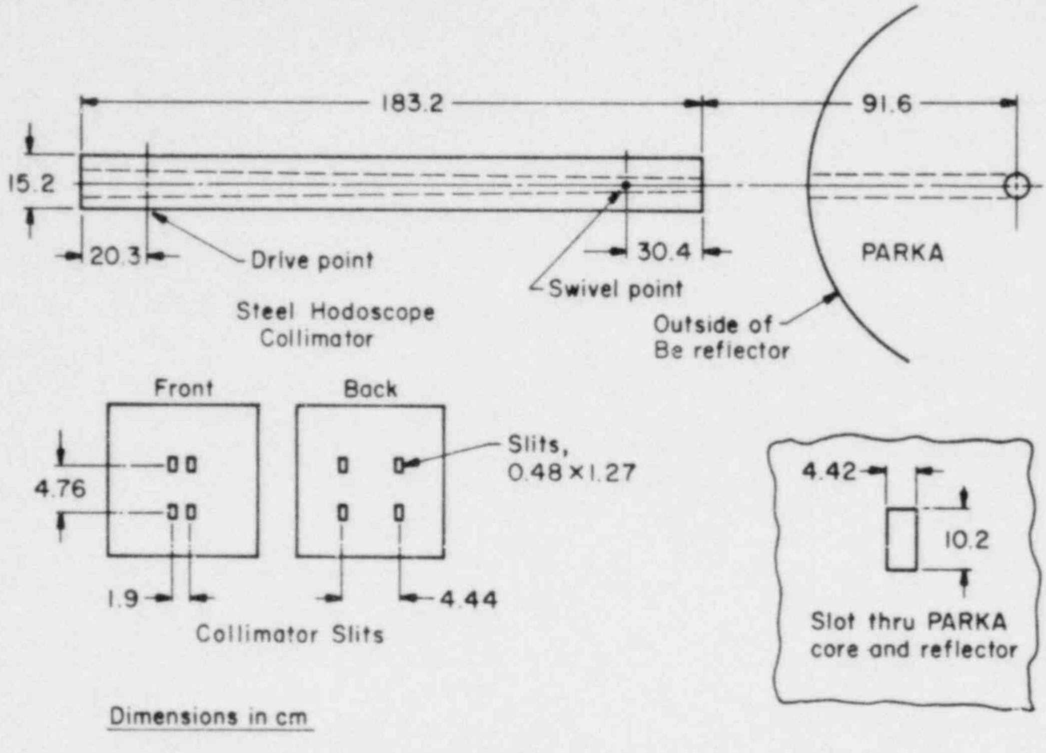

Fig. 10.
Details of the hodoscope collimator and test region geometry.

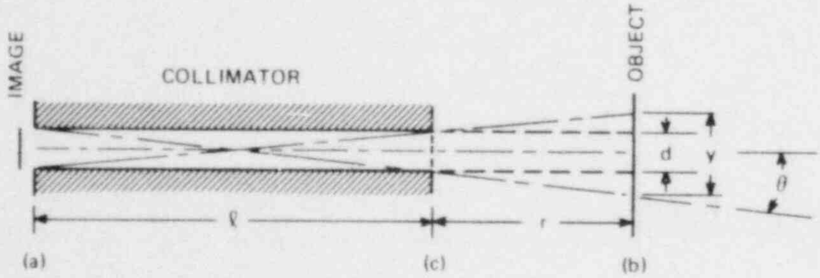

Fig. 11.
Field of view of a collimator slot.

The horizontal resolution y′ of the collimator slot is taken to be the width at which the sensitivity of the detector mounted at (a) falls to half of its maximum. Therefore,

$$y' = d[1 + (r/\ell)] \quad (3)$$

In a similar fashion, one derives an expression for the vertical resolution. From the dimensions given in Fig. 10, a horizontal resolution of 7.2 mm and a vertical resolution of 19.05 mm are determined.

C. Test Assemblies

Simulated fuel pins of Fast-Flux Test Facility (FFTF) dimensions were fabricated by loading 4.8-mm-diam by 50.4-mm-long extruded pellets of 93.09%-enriched UO_2 into stainless steel tubing. The tubing, rejected FFTF fuel-pin casing obtained from Battelle Northwest Laboratories, has an inside diameter of 5.08 mm and a wall thickness of 0.38 mm. Eighteen pellets, each containing 7.83 g of ^{235}U, were loaded into the central 91.4-cm region of the 137-cm-long fuel pins. The ends of the pins were filled with 25-cm-long sections of 4.75-mm-diam drill rod. The bottom ends of the pins are rounded to assure easy insertion into grid plates. A threaded fixture is provided on top to allow attachment to a pin-motion actuator. Details of a test fuel pin are given in Fig. 12.

Fuel pins are assembled into test bundles with aluminum grid plates drilled to locate pins in a hexagonal pattern with 7.26 mm between centers. In the region of the viewing slot, the grid plates are stacked to provide a solid aluminum matrix for the test bundle as a crude nuclear substitute for sodium. Measurements described below showed that the presence of the aluminum did not materially affect fuel-motion monitoring.

A test well was formed on the axis of the PARKA core by removing 37 of the hexagonal fuel elements and inserting a 110.7-mm-o.d. by 103.25-mm-i.d. steel liner. An inner lining 96.5 mm i.d. by 101.6 mm o.d. is mounted to rotate within the outer liner so that the test assembly can be oriented at any angle with respect to the viewing slot. Remote orientation is provided by means of a stepping-motor and rim-gear drive at the upper end. A drawing of a test assembly in the test well is shown in Fig. 13.

To facilitate the handling of test assemblies after irradiation, a shielded cart has been built. This cart provides the lower body of a person working on test assemblies the protection of 50 cm of lead shielding. The cart is shown in use in Fig. 14.

Test assemblies in TREAT and in future safety test facilities must be encapsulated in steel as thick as 45 mm. This much steel is bound to seriously affect the ability to monitor fuel motion in the test assembly. Accordingly, it was necessary to measure the effect of steel on ex-core imaging techniques. For these tests, a 37-pin test assembly was surrounded in the viewing region by a

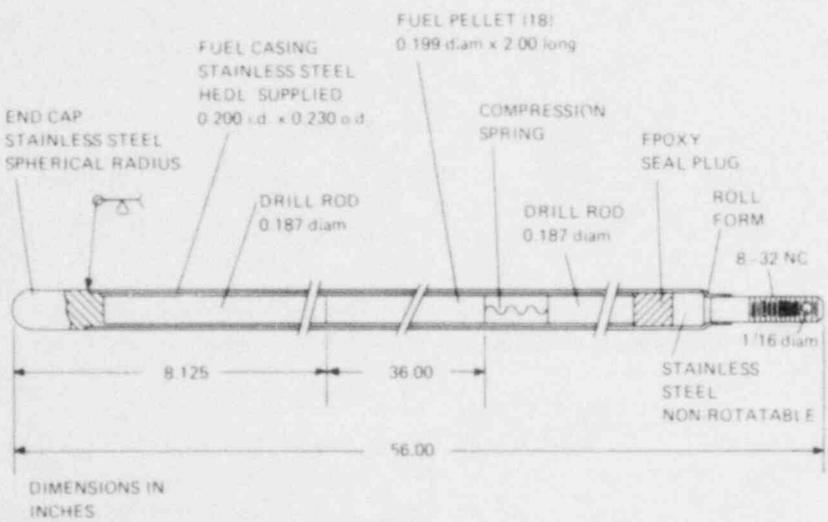

Fig. 12.
Details of a fuel pin.

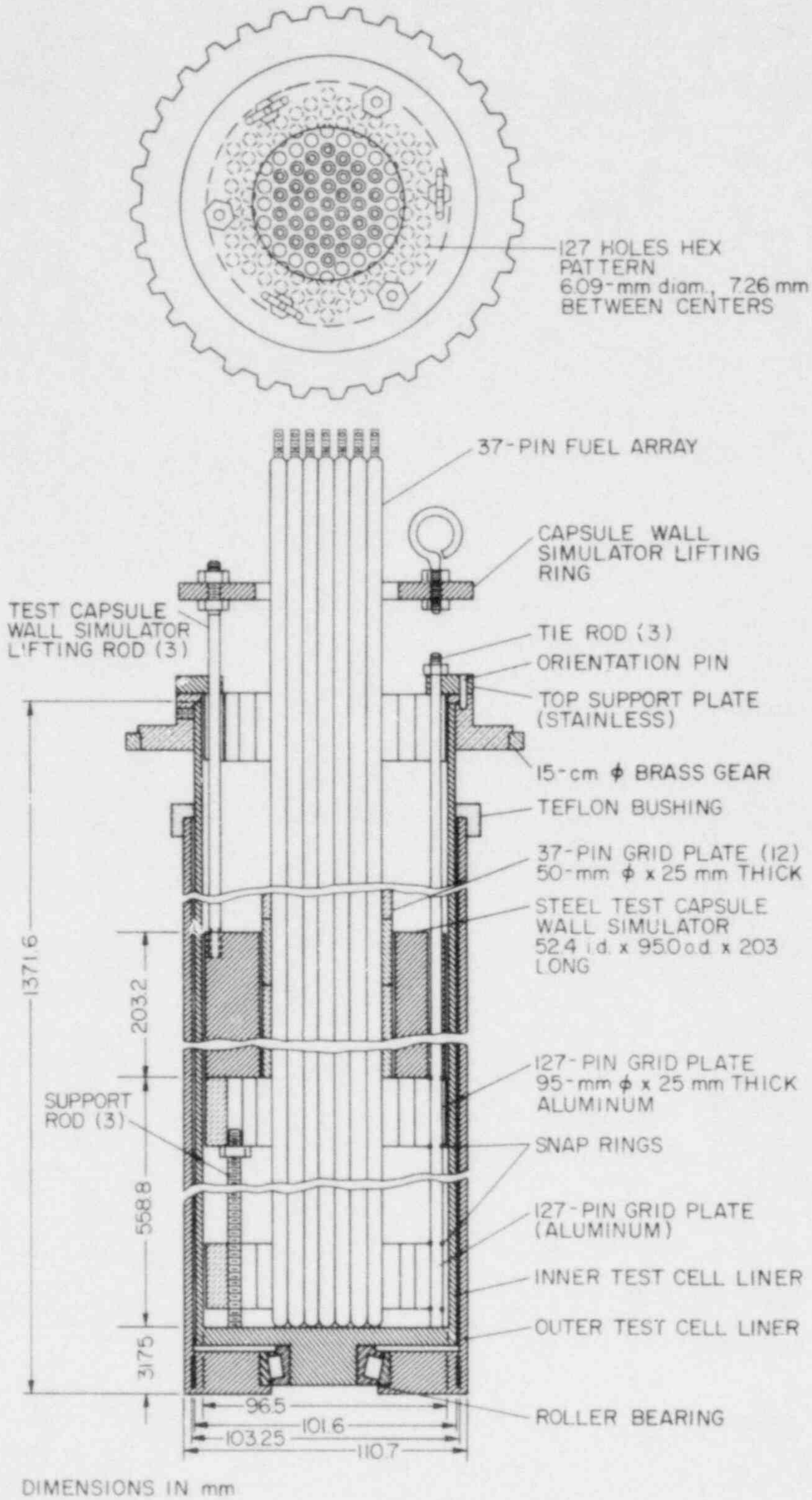

Fig. 13.
Details of a fuel-pin assembly in test well.

Fig. 14.
Shielded test assembly cart.

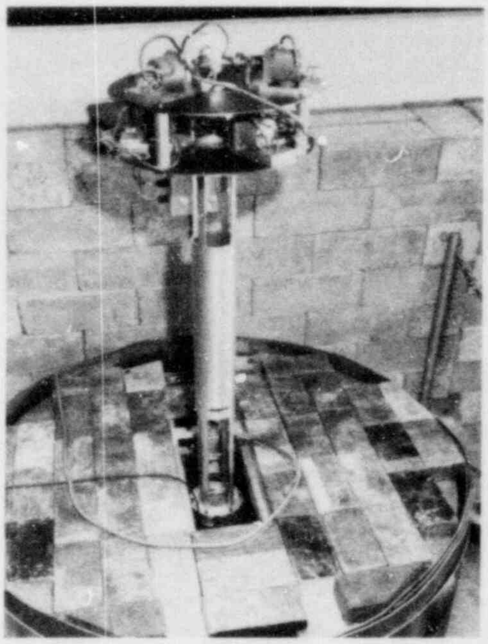

Fig. 15.
Actuator turret for raising and lowering fuel pins and for rotating the test assembly.

cylindrical casing 52.4 mm i.d. by 95 mm o.d. by 203 mm long. This casing was remotely raised from and lowered into the field of view by means of steel cables attached to a stepping-motor-driven drum.

Up to six pins in a test assembly may be raised from or lowered into the field of view by means of nylon strings attached to stepping-motor-driven spools. The lifting assemblies for the fuel pins and the steel test capsule are mounted on a turret that is attached to the inner liner of the test well. This turret is shown in Fig. 15.

Stepping motors controlling motion of the fuel pins and the steel test capsule, rotation of the test well, and panning of the hodoscope scanner are all driven by a common stepping-motor controller through a system of selector switches and relays that permit only one motor to be operated at a time. Reproducibility of settings is obtained by counting pulses delivered to the stepping motors. The controller has provisions for presetting the amount of motion desired. A position readout in the controller is coupled to an automatic data-recording system.

III. INSTRUMENTATION

A. Neutron Detectors

A number of detectors have been used with the collimator to measure the pattern of radiation emitted by the test section. For detection of fast neutrons, Hornyak Buttons[11] similar to those used on the TREAT hodoscope,[8] ^{4}He-recoil proportional counters,[12] and stilbene scintillation detectors have been used. The ideal neutron detector for this purpose is one that is as insensitive as possible to gamma radiation and that can be biased for neutrons with energies of from 1 to 2 MeV. To minimize backgrounds, the detector should have a sensitive area closely matching the slot size. Hornyak Buttons and ^{4}He-recoil detectors have been found to meet the criteria of gamma insensitivity and energy discrimination. However, stilbene detectors are more efficient by a factor of 5 than Hornyak Buttons of the same size and offer the additional advantage of pulse-shape discrimination,[13] by which it is possible to obtain neutron and gamma-ray data simultaneously.

1. Hornyak Buttons. Initial data were taken with Hornyak Buttons that provided a direct comparison with data obtained at TREAT. These detectors are pieces of the standard suspension of zinc sulfide in Lucite (purchased from Nuclear Enterprises, Inc.) cut into rectilinear pieces 12.5 mm square by 6.2 mm thick and mounted edgewise in Lucite light pipes using Nuclear Enterprises, Inc. NE-580 optical cement. Finished assemblies were coated on the sides and one end with titanium oxide reflector paint (Nuclear Enterprises, Inc. NE-560) and coupled to Amperex Electronic Corp. XP1110 19-mm-diam photomultipliers.

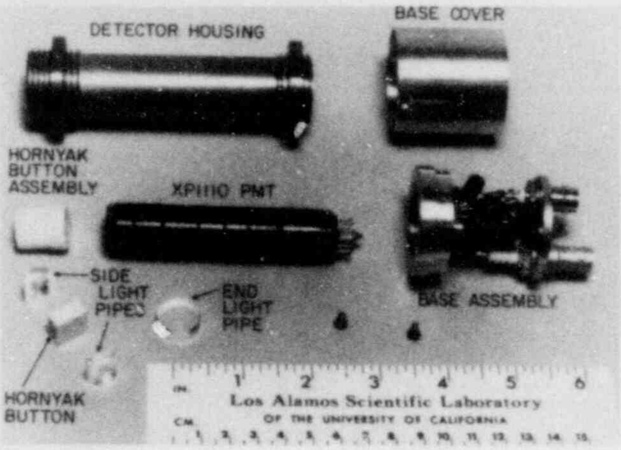

Fig. 16.
Exploded view of a Hornyak-Button detector assembly.

An exploded view of the detector assembly is shown in Fig. 16. The detector end of the brass photomultiplier housing screws into a brass plate attached to the hodoscope collimator. The photomultiplier divider network, shown in Fig. 17 together with the other electronic components used for these detectors, is according to the recommendations of the tube manufacturer except that capacitance values were chosen on the basis of response of the tube with a Nuclear Enterprises, Inc. NE-102 scintillator to x-ray pulses from a 5-MeV linear accelerator. Values chosen minimized saturation and afterpulsing without imposing too long a recovery time on the divider chain after large pulses. It was also felt desirable to hold divider current to less than 1.5 mA, since it was thought that large arrays of detectors might be needed. A negative high-voltage supply was used to reduce noise and to eliminate the need for a coupling capacitor at the anode, which is at ground potential. This in turn required that detector assemblies attached to the photocathode be nonconducting to avoid inducing spurious noise at the photocathode resulting from electrical discharge or static effects in the glass.

Pulse-height distributions for monoenergetic neutrons incident upon the Hornyak-Button detectors are shown in Fig. 18. The detectors were tested at the LASL 3.75-MeV Van de Graaff accelerator using monoenergetic neutrons from the ^{7}Li(p,n)^{7}Be reaction. For these tests, the neutron energy spread was approximately 20 keV. Each curve is normalized to a neutron fluence of 2.2×10^7 neutrons/cm^2, as determined with a ^{3}He long counter[14] that monitored the fast-neutron flux. For use on the hodoscope, amplified signals from the detectors

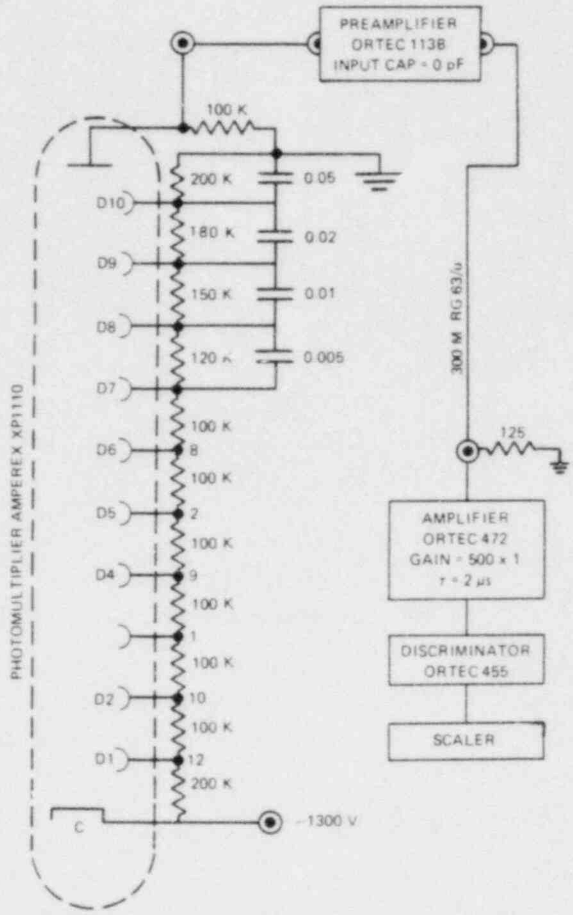

Fig. 17.
Electronics for Hornyak-Button detectors.

were counted using a discriminator setting just higher than that point at which counts were registered from a 5-mCi ^{60}Co source held adjacent to the detector. The counting efficiency of the detectors as a function of energy, derived from the data shown in Fig. 18, is shown in Fig. 19.

2. ^{4}He-Recoil Detectors. Two ^{4}He-recoil proportional counters were evaluated as neutron detectors for the present hodoscope studies at the PARKA facility and for an STF hodoscope system. These detectors are of interest because of their known low sensitivity to thermal neutrons and gamma rays, their relatively high overall efficiency for fast-neutron detection, and their pulse-height distribution, which permits neutron-energy discrimination. The detectors have an active size of 12.7 mm in diameter by 150 mm long. They were operated at 1500 V with an ORTEC Inc. model 109 PC preamplifier and model 472 spectroscopy amplifier with time constants set at 3 μs.

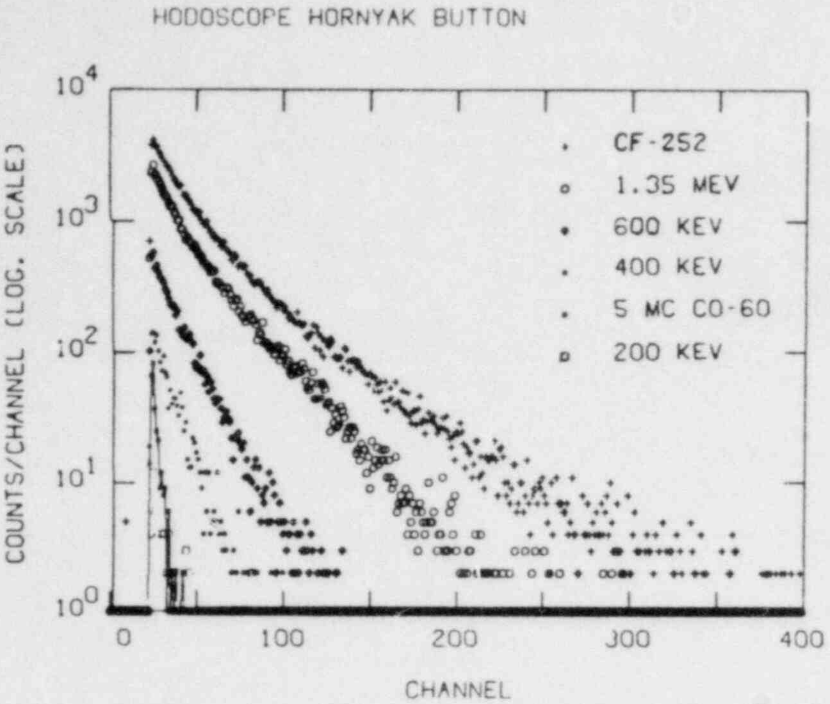

Fig. 18.
Pulse-height distributions of a Hornyak Button for neutrons of various energies and for an intense gamma-ray source.

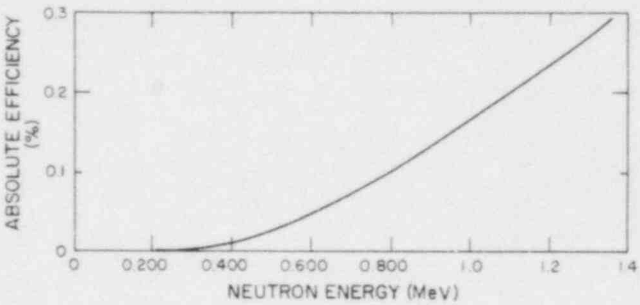

Fig. 19.
Absolute counting efficiency of a Hornyak-Button detector as a function of neutron energy.

These detectors were bombarded axially with monoenergetic neutrons from the $^{7}Li(p,n)^{7}Be$ reaction at the LASL 3.75-MeV Van de Graaff accelerator. Pulse-height distributions for neutrons of various energies are shown in Fig. 20. The asymmetry of the ^{4}He neutron-scattering cross section causes maxima at the low- and high-energy ends of pulse-height distributions for neutrons of energies between 400 and 1200 keV. Figure 21 is a plot of the measured counting efficiency of these detectors as a functions of neutron energy. The solid curve is the ^{4}He total neutron cross section. The fact that detector efficiency falls off with decreasing neutron energy makes it especially easy to bias the output of these detectors against low-energy neutrons.

The measured efficiency for counting 1-MeV neutrons incident along the detector axis was 3.2% for a pulse-height discriminator setting equivalent to 75 keV of energy deposited in the counter. This compares favorably with the efficiency obtainable with the 12.7- by 12.7- by 6.4-mm stilbene detectors discussed below. However, because of the preponderance of low-voltage pulses in the ^{4}He-recoil detectors for neutrons of energies useful for fuel self-imaging, biasing the detector outputs at substantial neutron energies results in very high losses in counting efficiency. For instance, for an energy bias of 1.4 MeV, the counting rate of these detectors mounted on the PARKA hodoscope is about one-twentieth of the rate available from the stilbene detectors with a similar bias. A lower-energy bias results in less differentiation between test-section and driver neutrons.

3. Stilbene Detectors. The use of organic-crystal and plastic scintillators to detect neutrons is discussed in some detail by Swartz and Owen.[15] In these media, fast neutrons produce recoil protons, which in turn give up their energy in ionization tracks in the detector; the

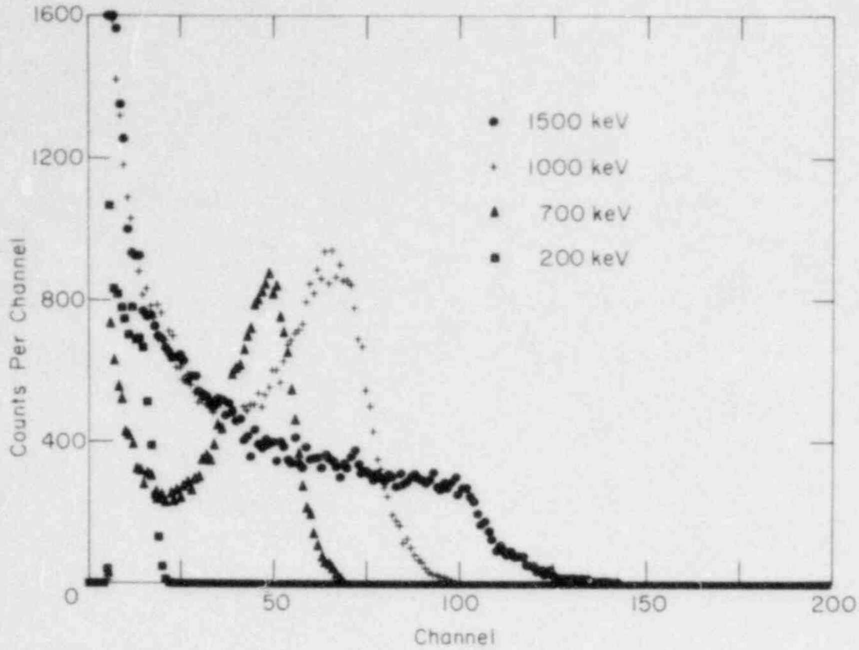

Fig. 20.
Pulse-height distributions of a ^{4}He-recoil proportional counter for neutrons of various energies.

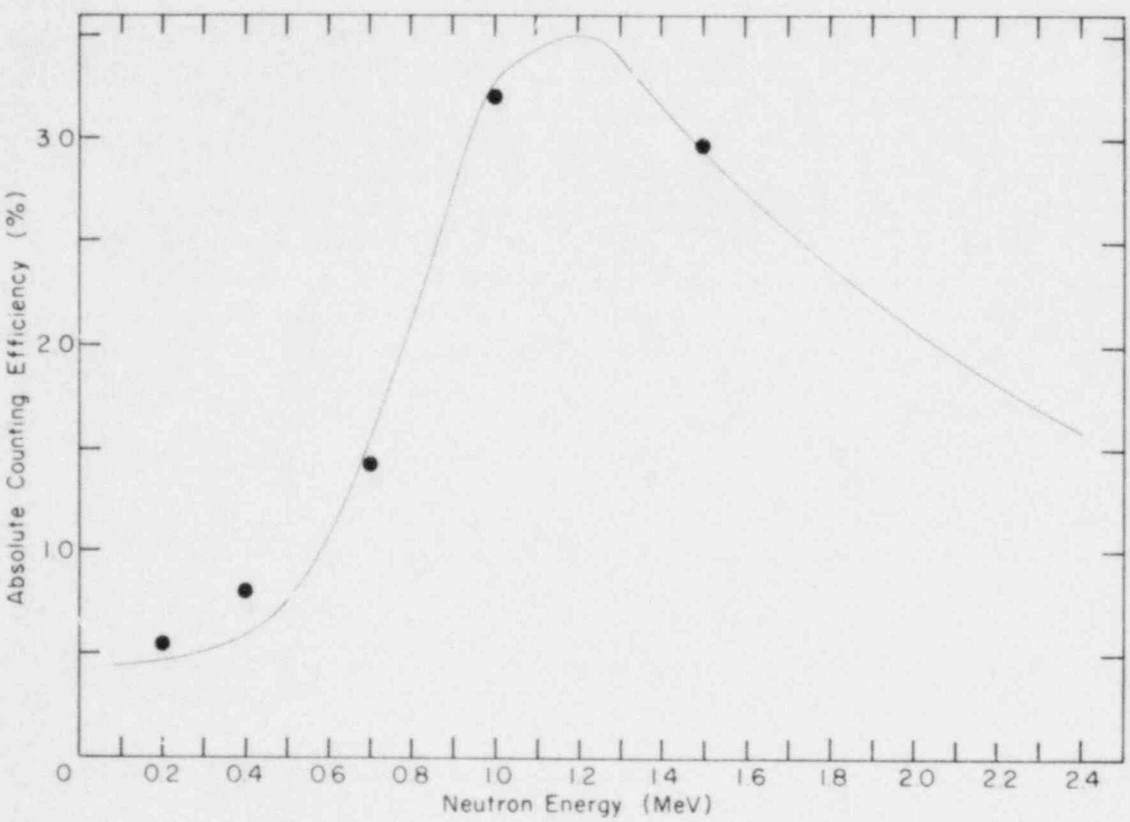

Fig. 21.
Absolute counting efficiency of a ^{4}He-recoil proportional counter as a function of neutron energy. Discriminator threshold was 75 keV.

energy of the ionization tracks are then partially converted into light. If the light output of the detector were linear with the energy of the recoil protons, one would expect monoenergetic neutrons to produce a rectilinear pulse-height distribution corresponding to n-p scattering, which is isotropic in the center-of-mass system. However, the light output is not linear with recoil-proton energy. As a result, pulse-height distributions are distorted, with more pulses at the low-energy end of the scale, and the maximum pulse height is not proportional to the neutron energy.

On the other hand, gamma rays deposit their energy in the detecting medium by Compton scattering of electrons in a process that results in a nearly linear relationship between the energy of the scattered electron and the measured light output. Photons of energy E_0 will produce a continuous distribution of Compton electrons up to an energy E_{max} given by

$$E_0/E_{max} = 1 + (m_0c^2/2E_0) \tag{4}$$

where m_0c^2 is the rest energy of the electron (511 keV). The distribution is peaked at E_{max}.

Figure 22 compares the measured light output (expressed as equivalent electron energy) of a stilbene scintillator as a function of incident neutron and gamma-ray energy. The fact that gamma rays produce on the average a greater number of scintillations in stilbene than do neutrons of the same energy means that, in a mixed gamma-ray-neutron field, the output of the scintillator will be dominated by gamma events unless these are suppressed. Pulses due to gamma rays can be suppressed because the average decay time of pulses generated by recoil protons from neutron interactions is greater than the decay time of pulses generated by Compton electrons.

A block diagram of the electronics used with the stilbene detectors is shown in Fig. 23. The crystals, 12.7-mm square by 6.4-mm-thick, were coupled geometrically with the hodoscope slots by embedding them edgewise in Lucite light pipes. The scintillator assemblies were viewed by Amperex Electronic Corp. XP1110 photomultiplier tubes, the signals from which were passed through ORTEC Inc. model 113 preamplifiers, 300 m of RG63/U cable from the critical-assembly building to the control room, and then through ORTEC Inc. model 460 delay-line-shaping amplifiers. The outputs of the amplifiers were analyzed for risetime distribution using ORTEC Inc. model 458 pulse-shape analyzers.

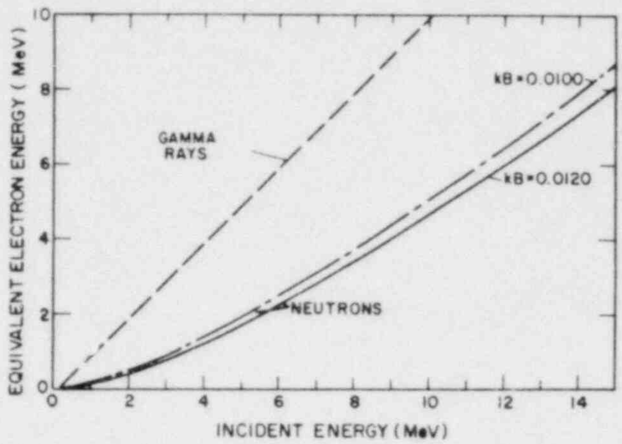

Fig. 22.

Light output (expressed in equivalent electron energy) of a stilbene scintillator as a function of incident neutron or gamma-ray energy for two different crystal parameters.

The pulse-shape analyzer gives an output pulse of amplitude proportional to the 10-90% risetime of the incoming signal. Figure 24 is a comparison of risetime distributions obtained with a ^{238}Pu-Be neutron source and with a ^{60}Co gamma-ray source. For this test, the input discriminator of the pulse-shape analyzer was set to accept pulses with amplitudes greater than one-half the Compton edge from 662-keV ^{137}Cs gamma rays. The equivalent neutron energy threshold is 1.3 MeV. The independence of pulse-risetime distributions on neutron and gamma-ray energies and the resultant stability of the n-γ discrimination point (the minimum between the gamma-ray and neutron distributions) was checked by comparing the response to reactor radiation (as seen through the hodoscope) with the response to ^{238}Pu-Be neutrons.

B. Gamma-Ray Detectors

Not all proposed techniques for STF fuel-motion monitoring have involved fast-neutron imaging. Some of the coded-aperture techniques use gamma radiation as their image-forming medium.[6] Furthermore, it has been proposed that clad motion be monitored by imaging high-energy capture gamma rays from iron.[16] The use of the hodoscope for gamma-ray imaging, particularly for imaging capture gamma rays from iron in the face of an intense but lower-average-energy fission-gamma spectrum, requires optimization of the gamma detector. Ideally, one would like a detector that is small (to

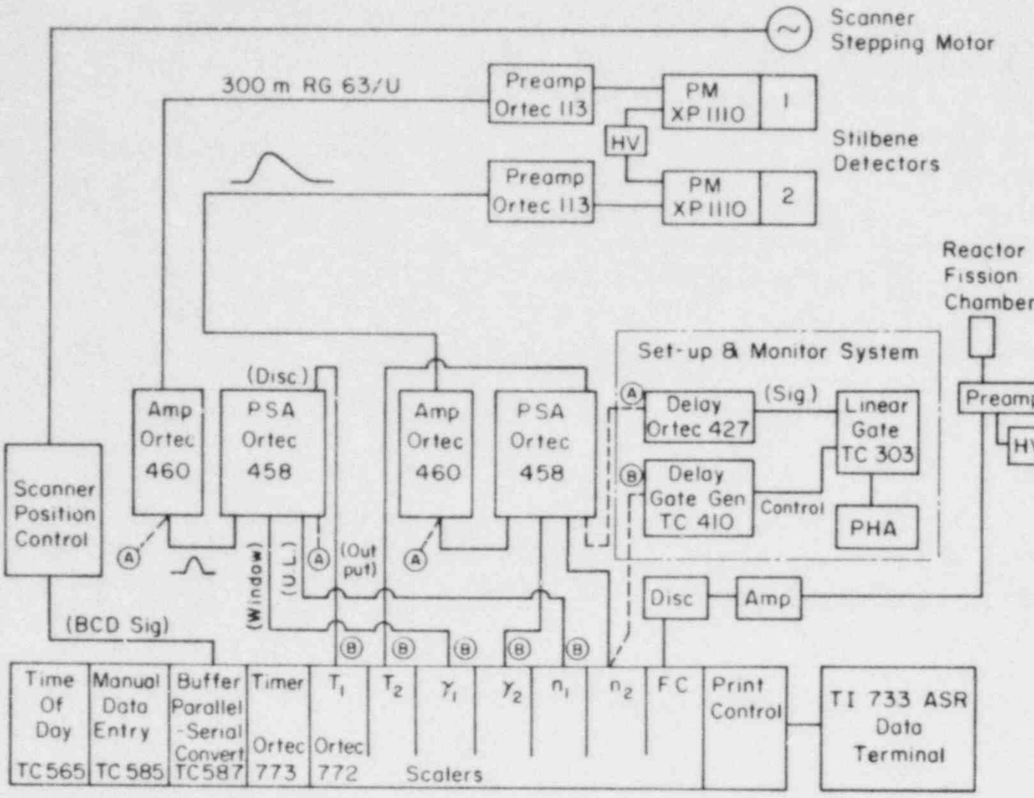

Fig. 23.
Block diagram of electronics for hodoscope scans with stilbene detectors.

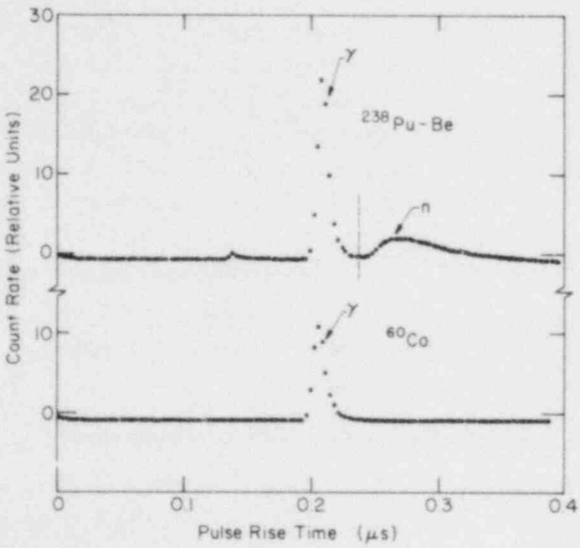

Fig. 24.
Pulse-risetime distributions from stilbene detector for a ^{238}Pu-Be neutron source and for a ^{60}Co gamma-ray source.

minimize sensitivity to ambient backgrounds and to make arrays of large numbers of detectors practical), has a high overall detection efficiency for high-energy radiation, and has a response peaked at full-energy absorption to assure good energy discrimination.

1. NaI(Tl) and NE-102. Hodoscope gamma-ray imaging of LMFBR fuel test assemblies has been studied using stilbene, Nuclear Enterprises, Inc. NE-102 plastic, and NaI(Tl) scintillators. The plastic and NaI(Tl) scintillators, cylinders 12.5 mm in diameter by 12.5 mm long, were mounted on Amperex Electronic Corp. XP1110 photomultipliers. Signals were processed with the same tube bases, preamplifiers, and amplifiers that were used for the Hornyak Buttons. It was found that the small NaI(Tl) detectors have a rather low peak-to-Compton ratio for gamma rays at energies greater than 1 MeV. Moreover, activation of iodine, with resultant buildup and decay of the 25-min ^{128}I activity, has been a deterrent to their use. Plastic and stilbene detectors have even less optimum pulse-height responses for the range of gamma-ray energies involved.

2. Bismuth Germanate. Newly introduced scintillation-grade bismuth germanate (Bi_4GeO_{12}) crystals have the desired detector characteristics.[17] This material, twice as dense as NaI, has an efficiency for gamma absorption such that pulse-height distributions from a bismuth germanate (BGO) crystal are equivalent to those from a NaI(Tl) crystal with linear dimensions three times larger. Thus a $600, 38-mm BGO detector is nearly equivalent to a 125-mm NaI(Tl) detector worth $2000.

Three BGO crystals, a 38-mm-diam by 38-mm-high cylinder, a 12.5-mm-diam by 12.5-mm-high cylinder, and a rectangular piece 12.5-mm square by 6.2-mm-thick, have been purchased from the Harshaw Chemical Co. for evaluation. The latter two crystals were used with the PARKA hodoscope. Since the light output of BGO is only 8% of that of NaI(Tl) for incident photons of a given energy, a low-noise photomultiplier is needed to obtain optimum pulse-height resolution. We found that an Amperex Electronics Corp. XP2000 51-mm-diam tube gave satisfactory results. Amperex XP1110 19-mm-diam photomultipliers, which have been used for the Hornyak Buttons and stilbene scintillators in the hodoscope measurements, were found to be quite satisfactory for use with the smaller BGO detectors. The BGO crystals were coated on the cylindrical surface and one end with titanium dioxide reflector paint. The rectangular crystal was mounted edgewise on the 19-mm photomultiplier. Electronic equipment used for testing included an ORTEC Inc. model 266 photomultiplier base, model 113 preamplifier, and model 472 spectroscopy amplifier. The amplifier shaping time constant was 3 μs. The photomultipliers were operated at 1300 V.

In Fig. 25, the pulse-height response of the 38-mm BGO crystal for ^{137}Cs gamma rays is compared to that of a 38-mm NaI(Tl) detector. A 1-μCi source was counted for 200 s on contact with the face of each detector. The full width at half-maximum (FWHM) from the full-energy peak of the BGO response is nearly twice that of the NaI(Tl) distribution. However, the peak-to-Compton ratio of the BGO detector is considerably larger and its backscatter peak is somewhat smaller. These characteristics should simplify the unfolding of continuous spectra. The full-energy-peak efficiency of BGO is 3.3 times that of NaI(Tl) for these detectors.

The pulse-height response for ^{60}Co gamma rays is shown in Fig. 26. The resolution of the 38-mm BGO detector is not quite sufficient to resolve the 1.17- and 1.33-MeV photopeaks. However, the Compton peak in the 38-mm NaI(Tl) detector is now prominent enough to interfere with the detection of small amounts of lower energy gamma rays and makes spectrum unfolding difficult. At 1.33 MeV, the full-energy-peak efficiency of the BGO detector is 4.5 times that of the NaI(Tl) detector.

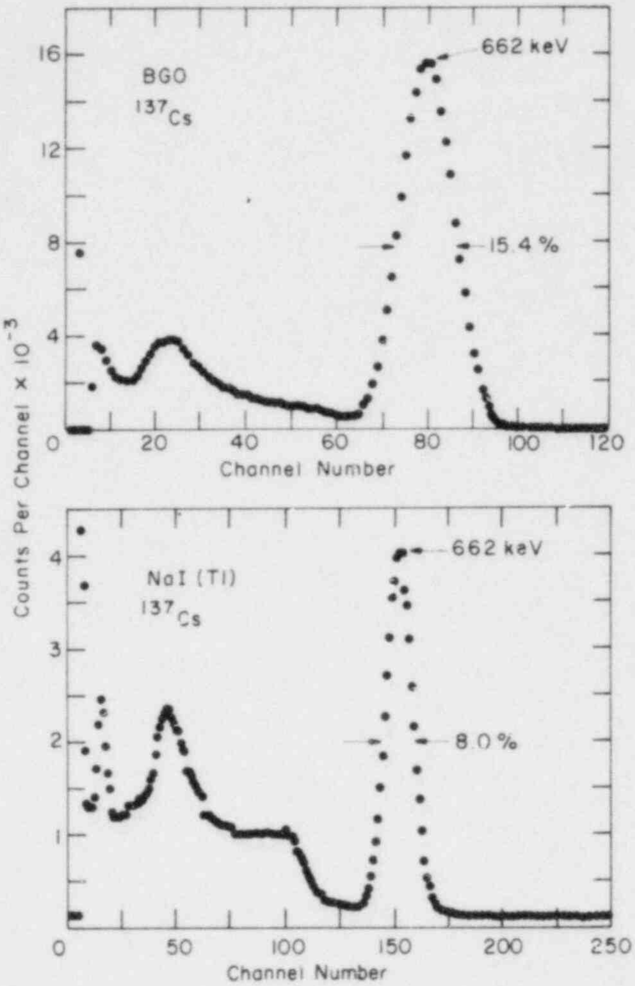

Fig. 25.
Pulse-height responses of 38-mm by 38-mm BGO and NaI(Tl) scintillators to ^{137}Cs gamma rays. A 1-μCi source was counted for 200 s on contact with the face of each detector.

As photon energy increases, BGO becomes the clear choice over NaI(Tl). We illustrate this in Fig. 27, which shows the responses of the two 38-mm detectors to 1.37- and 2.75-MeV gamma rays from the decay of ^{24}Na. At 2.75 MeV, the BGO detector shows a predominance of the full-energy peak over the annihilation-escape peaks and the Compton shoulders. For the NaI(Tl) detector, the full-energy and escape peaks of the 2.75-MeV line are approximately equal and the Compton peaks of both lines are quite evident. The efficiency of the BGO

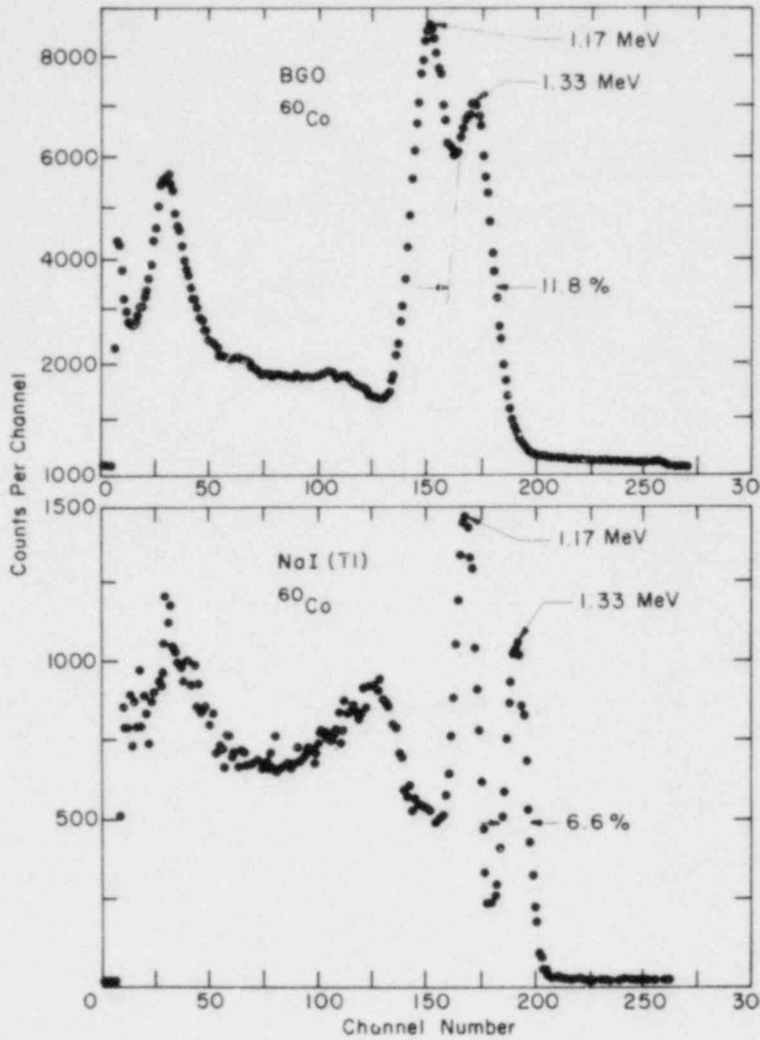

Fig. 26.
Pulse-height responses of 38-mm by 38-mm BGO and NaI(Tl) scintillators to ^{60}Co gamma rays.

detector for the 2.75-MeV full-energy peak is 5.6 times that of the NaI(Tl) detector.

Figure 28 shows the response of the 12.5-mm BGO cylinder to ^{24}Na radiation. In terms of peak-to-total ratio and total counts per photon incident upon the crystal, this detector is roughly equivalent to the 38-mm NaI(Tl) detector.

The response of the 38-mm BGO detector to 4.43-MeV radiation is plotted in Fig. 29. This radiation, from the decay of the first excited state of ^{12}C, was derived from the ^{9}Be(α,n)^{12}C* reaction in a ^{238}Pu-Be neutron source.

The response of the 38-mm BGO detector to higher energy radiation was measured by observing gamma rays from the decay of the 8.28-MeV excited level of ^{15}O. To produce this radiation, a thin film of tantalum nitride on a platinum backing was bombarded by 1.06-MeV protons at the LASL 3.75-MeV accelerator. The observed gamma rays result from a 5-keV-wide resonance in the ^{14}N(p,γ)^{15}0 reaction. With the detector 2 cm from the target, we obtained the pulse-height distribution shown in Fig. 30 in 84 min with a 2-μA proton beam. The 8.28-, 5.24- and 3.04-MeV lines are from the decay of the 8.28-MeV level of ^{15}O to the ground state. The 4.43-MeV radiation, from the ^{15}N(p,$\alpha\gamma$)^{12}C reaction, is due to the use of normal isotopic-content nitrogen as a target.

In Fig. 31, the full-energy-peak efficiency of the 38-mm BGO crystal for 0.1- to 8.28-MeV gamma rays is compared with that of a 38-mm NaI(Tl) crystal. For energies less than 2.6 MeV, absolute efficiencies were obtained by placing calibrated radioisotope sources 10 cm from the front face of the detector. Relative efficiencies from 3.04 to 8.28 MeV were obtained from the known branching ratios[18] of the decay of the 8.28-MeV level of ^{15}O and were normalized to the radioisotope data by matching the slopes of the two parts of the curve.

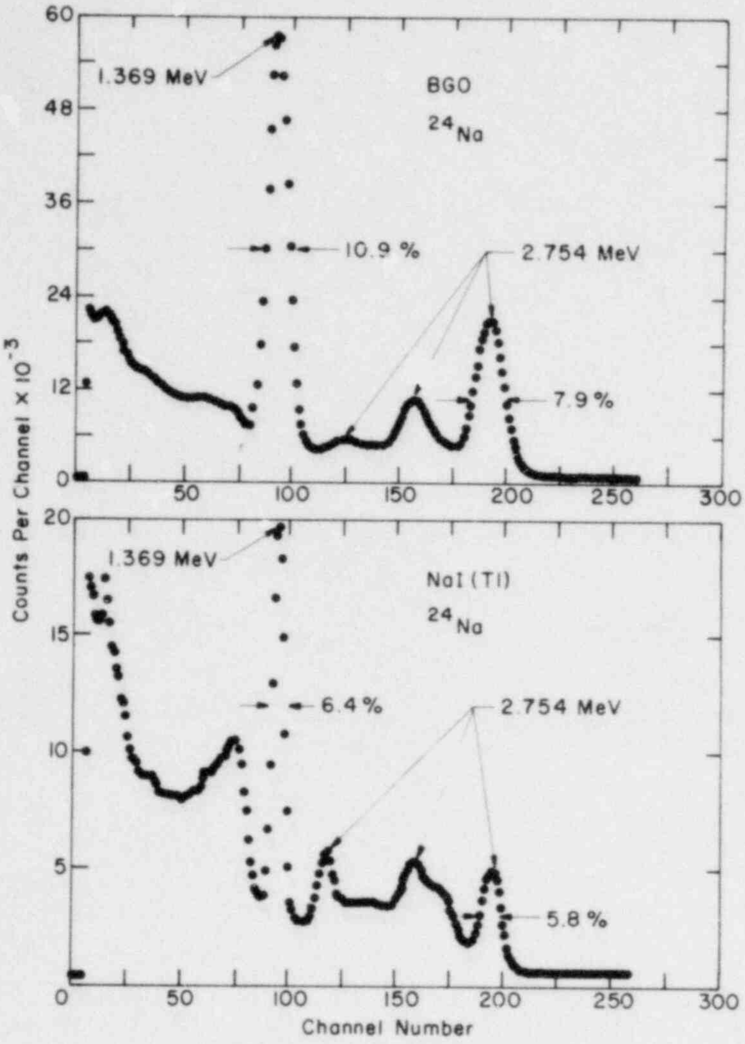

Fig. 27.
Pulse-height responses of 38-mm by 38-mm BGO and NaI(Tl) scintillators to ^{24}Na gamma rays.

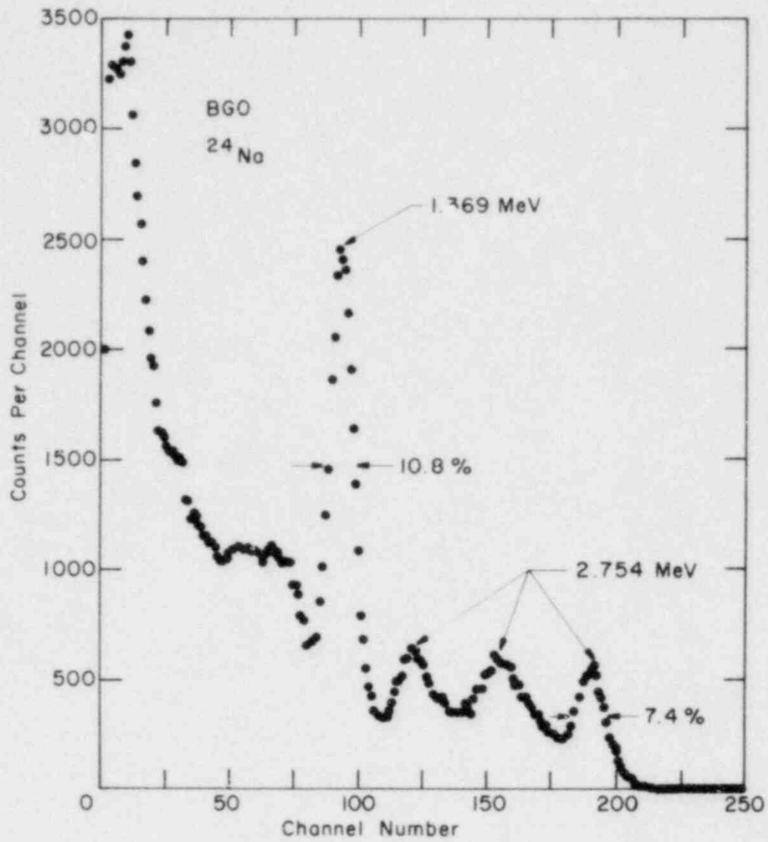

Fig. 28.
Pulse-height response of a 12.5-mm by 12.5-mm BGO scintillator to ^{24}Na gamma rays.

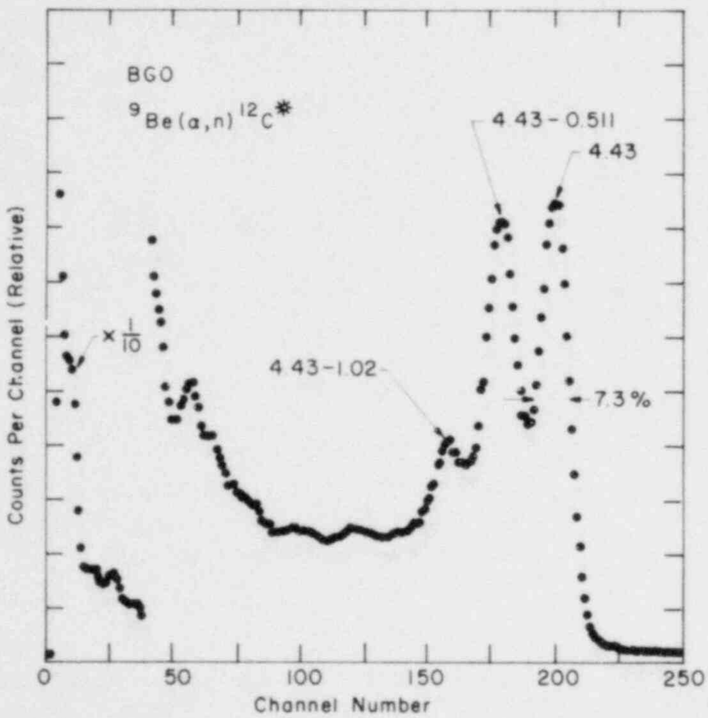

Fig. 29.
Pulse-height response of a 38-mm by 38-mm BGO scintillator to 4.43-MeV gamma rays.

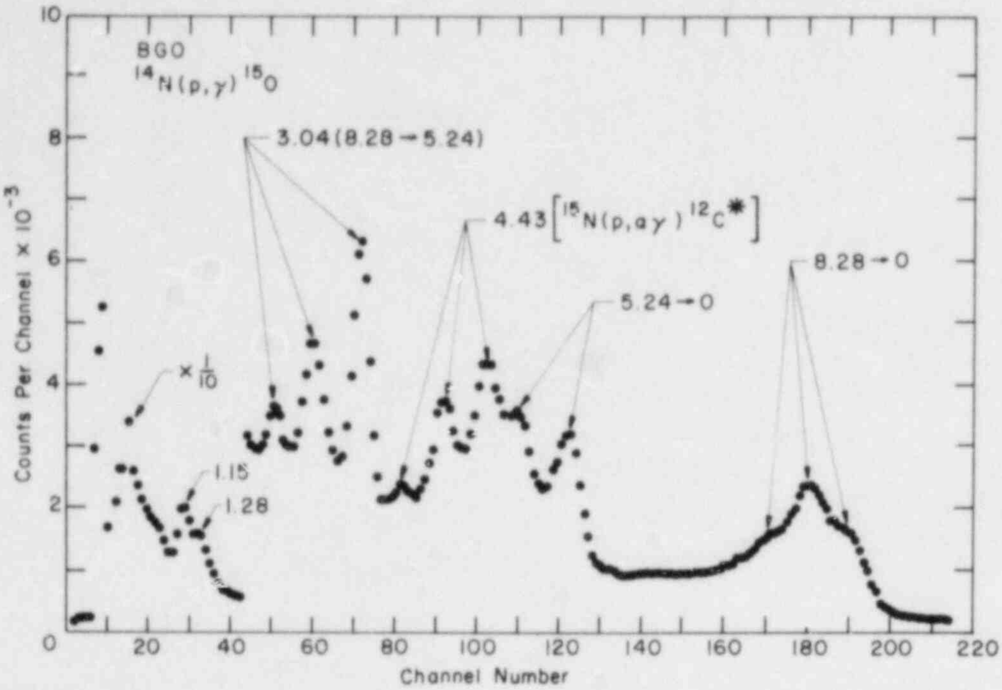

Fig. 30.
Pulse-height response of a 38-mm by 38-mm BGO scintillator to gamma rays from the 1.058-MeV resonance of the $^{14}N(p,\gamma)^{15}O$ reaction.

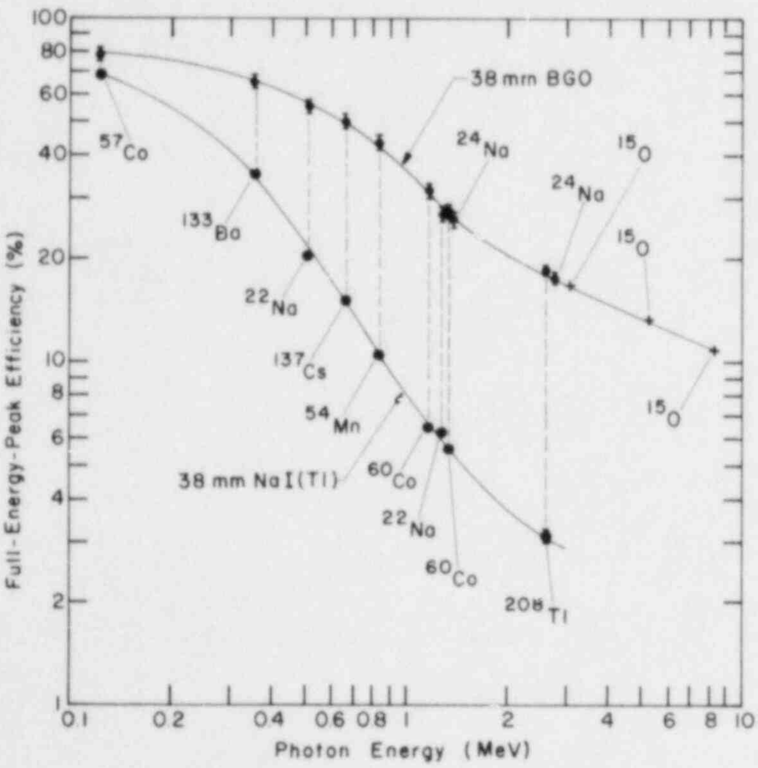

Fig. 31.
Full energy-peak efficiencies of 38-mm by 38-mm BGO and NaI(Tl) scintillators as functions of gamma-ray energy.

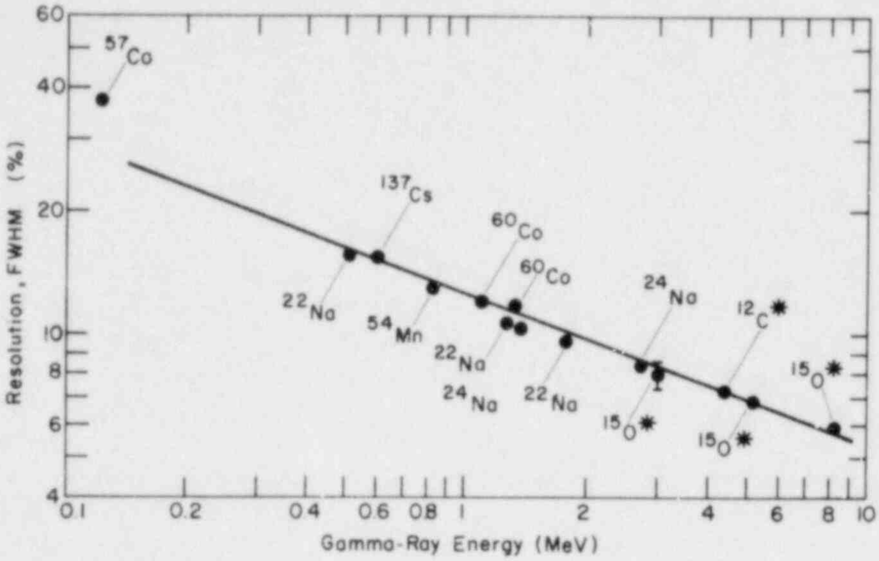

Fig. 32.
Resolution of the 38-mm by 38-mm BGO scintillator as a function of gamma-ray energy.

The resolution of the 38-mm BGO detector is shown in Fig. 32. Although this resolution is only about half that of equivalent NaI(Tl) crystals, the higher efficiency and the near absence of Compton continua make BGO the detector of choice for high-energy measurements when high resolution is not needed. Its ruggedness, comparable to Pyrex, and its nonhygroscopicity make it an ideal candidate for field applications such an environmental and health monitoring, nuclear safeguards assays, and uranium exploration. It would be an ideal detector for downhole assay by capture gamma-ray measurements.

It was necessary to determine whether BGO detectors would show effects of activation or radiation damage in the environment in which the PARKA hodoscope detectors operate. Accordingly, the 12.5-mm by 12.5-mm detector was mounted in front of one of the collimator slots while PARKA was operated at 5 mW/g ^{235}U for 4 h with a 37-pin test assembly in the test well. The collimator slot was held fixed on the center of the test assembly and the count rate from the detector, biased at 1 MeV, was taken every 5 min, starting at the time the reactor reached full operating power. The resulting data are shown in Fig. 33, together with those obtained simultaneously from a stilbene detector and the results of a previous run using a NaI(Tl) detector. The ratio of the

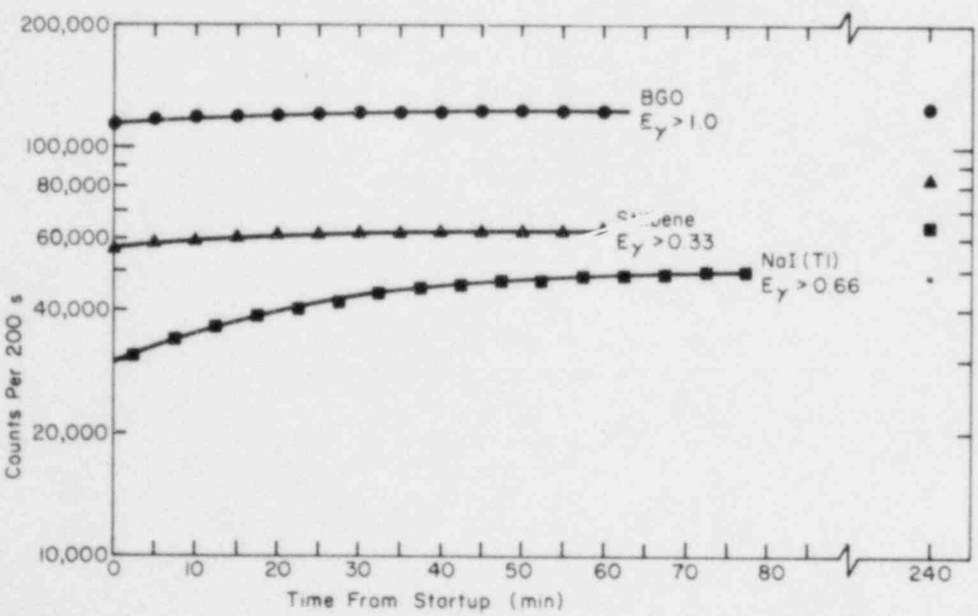

Fig. 33.
Count-rate buildup in BGO, stilbene, and NaI(Tl) detectors used with the PARKA hodoscope.

BGO and stilbene count rates remained constant over the entire 4-h run, suggesting that the 13% increase in count rate for both detectors was related to the radiation environment and is probably associated with fission-product buildup in the test section. The departure of the NaI(Tl) data from this behavior is obvious.

A pulse-height distribution from the 38-mm BGO detector mounted in front of one of the collimator slots is shown in Fig. 34. For this measurement, the collimator was pointed at the edge of the test assembly with the 21-mm-thick steel test capsule in place. In this position, the detector was "seeing" a total thickness of 154 mm of steel. We identified the observed high-energy radiation as capture gamma rays from iron. The indicated peak energies correspond to available data.[19] The 7.64-MeV peak is due to decay of ^{57}Fe to the ground state after thermal-neutron capture by ^{56}Fe. Higher energy peaks, at 9.30 and 10.16 MeV from neutron capture by ^{54}Fe and ^{57}Fe, were too weak to be useful for these studies. The spectrum displayed was accumulated in 3000 s with PARKA again operating at a power level of 5 mW/g ^{235}U.

IV. HODOSCOPE SCANS

A. Single-Pin Scans

Figure 35 shows the results of a hodoscope scan across a single fuel pin with two Hornyak-Button detectors in the same horizontal plane. The reactor was operated at 550 W (4.6 mW/g ^{235}U). The count time for each point was 500 s. The S/B ratio is low, only 0.2 compared to a typical S/B ratio of 3 for the TREAT hodoscope.[8] The low S/B ratio of our hodoscope is due to the epithermal neutron spectrum of PARKA. The driver neutrons of the TREAT reactor, a thermal reactor, are on the average easier to separate from the fast neutrons emitted by the test region. The harder driver spectrum will be needed, however, to produce uniform excitation across large fuel-pin arrays; the capability of the hodoscope technique must therefore be verified before incorporating it into the design of STFs for large-bundle tests.

The scan shown in Fig. 35 was made with the viewing slot extending only halfway through PARKA. The

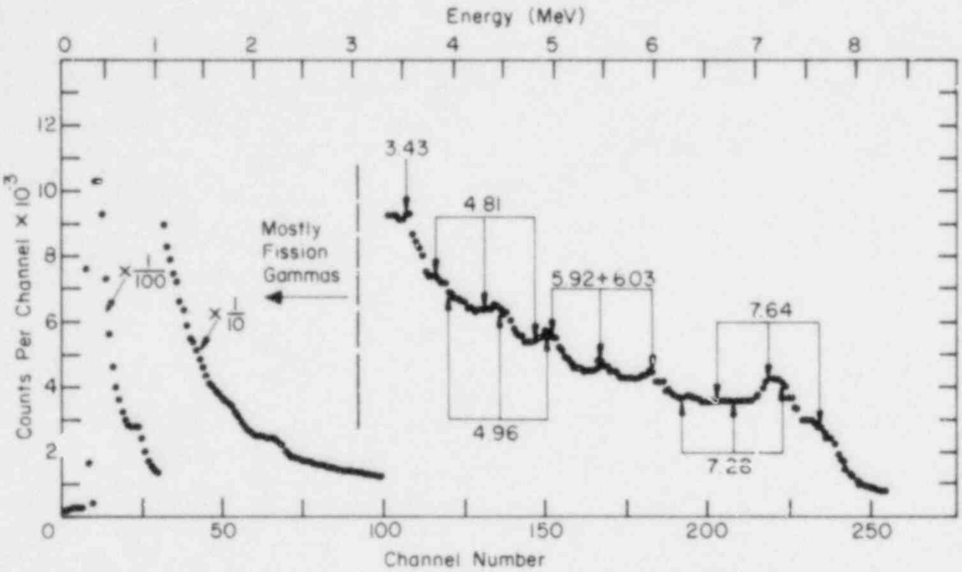

Fig. 34.

Gamma-ray pulse-height distribution from the PARKA hodoscope using a 38-mm by 38-mm BGO scintillator. Identified transitions from thermal-neutron capture in iron are from Ref. 19.

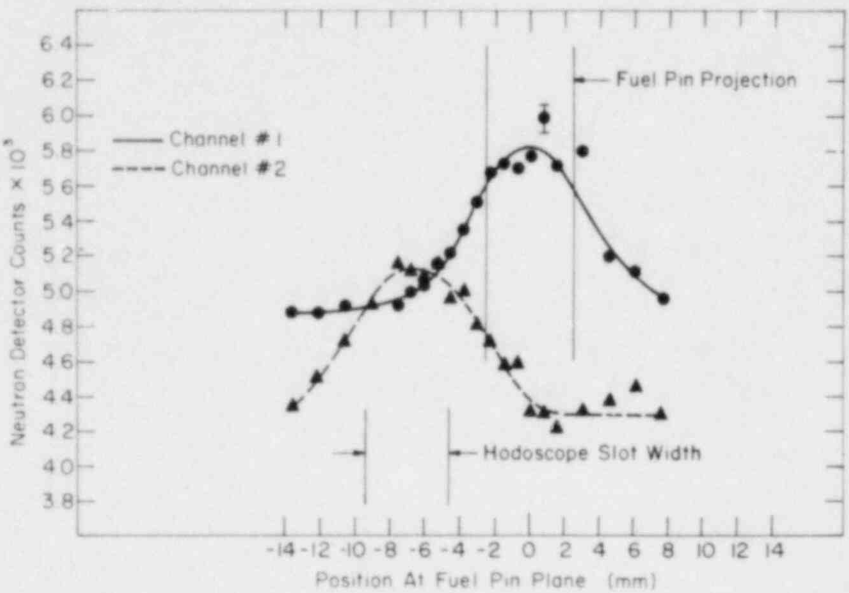

Fig. 35.
Two-channel scan with Hornyak Buttons of a single fuel pin in PARKA, with the viewing slot extending only to the center of the core.

single-pin S/B ratio has since been improved by extending the slot through the reactor so that the collimator slots do not "see" any PARKA fuel. As shown in Fig. 36, the slot extension has improved the S/B ratio by a factor of 3. This indicates the possible need for through slots for either hodoscope or coded-aperture imaging in safety test facilities. However, the half slot may be adequate for full-subassembly or larger tests, where the signal from the test bundle its may dominate the driver background.

The high counts on the right side of the through-slot scan shown in Fig. 36 are due to scattering from a piece of aluminum channel placed in the extended PARKA slot to support the fuel elements above the slot. This channel has since been replaced with a lighter, symmetrical support.

To study factors affecting the S/B ratio of the test-fuel image, single-pin neutron and gamma-ray scans were made using stilbene, NE-102, and NaI(Tl) scintillators and ^{4}He-recoil proportional counters. Simultaneous neutron and gamma-ray data were obtained from each of two stilbene detectors. The output of one of these detectors was biased with a discriminator setting corresponding to gamma-ray events with $E_\gamma > 0.33$ MeV and neutron events with $E_n > 1.3$ MeV. The other stilbene detector was biased for $E_\gamma > 0.66$ MeV and $E_n > 2.2$ MeV.

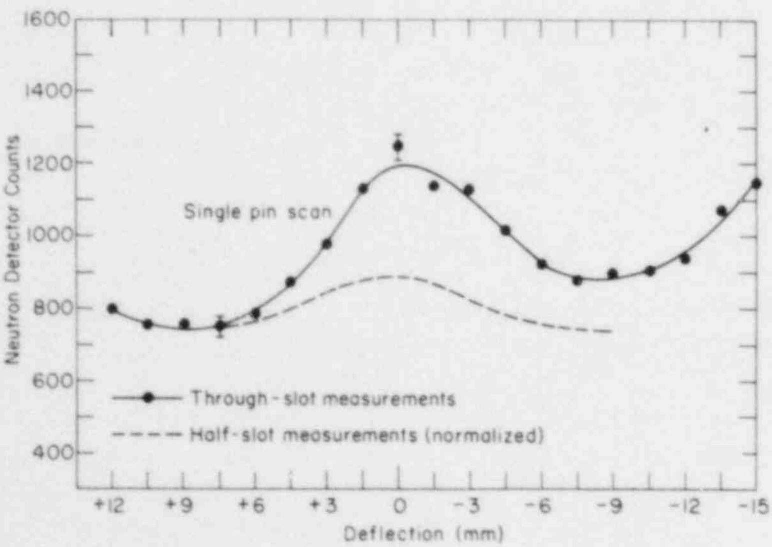

Fig. 36.
Comparison of single-pin scans with Hornyak Buttons before and after extending the viewing slot through the PARKA core.

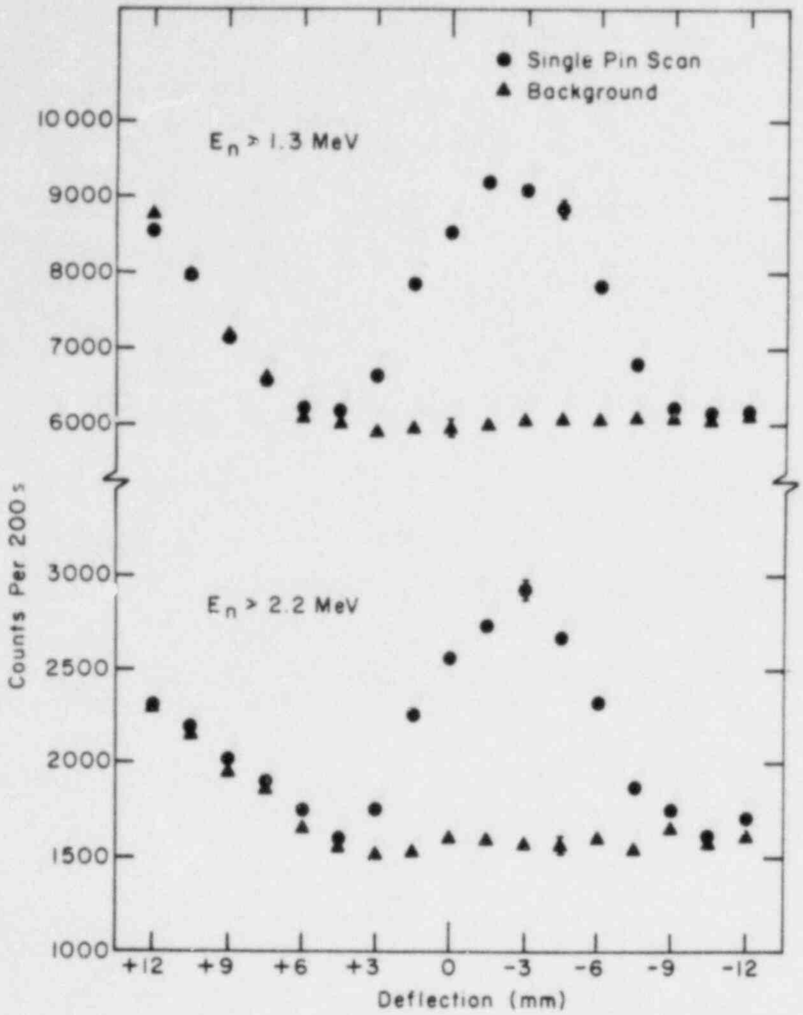

Fig. 37.
Neutron scan with stilbene of a single fuel pin.

Results of the stilbene neutron scanning of a single pin in PARKA are shown in Fig. 37, together with background scans of the empty PARKA test section. The asymmetry in the background radiation is probably caused by scattering from temporary shielding between the hodoscope and the reactor. As would be expected, the higher discriminator setting resulted in a better S/B ratio: 0.75 for $E_n > 2.2$ MeV compared with about 0.5 for $E_n > 1.3$ MeV. The S/B ratio for the lower discrimnator setting is only slightly better than that obtained with Hornyak Buttons biased for $E_n > 1$ MeV. However, the stilbene detectors are five times more efficient than the Hornyak Buttons, so that statistically better data could be taken with lower critical-assembly power and less operating time.

The corresponding single-pin gamma scans shown in Fig. 38 exhibited S/B ratios of ~1, somewhat better than that obtained for neutrons. This is contrary to our experience with larger test bundles.

The behavior of the single-pin neutron image was studied as a function of threshold energy using a ^{4}He-recoil detector with energy biases of 0.35, 0.7 and 1.4 MeV. The results are shown in Fig. 39. Because of the lower energy biases used for the ^{4}He-recoil detectors, the S/B ratios for a single pin are poorer than those obtained with stilbene detectors and Hornyak Buttons. In Fig. 40, the ratio of the single-pin count rate to the driver-neutron count rate is plotted as a function of discriminator setting (neutron energy bias) for ^{4}He-recoil and stilbene detectors. Higher energy biasing than that shown in Fig. 40 for the ^{4}He-recoil detectors was not feasible, because of the resulting low count rates.

Plots of single-pin scans taken with 12.5-mm-diam by 12.5-mm long NaI(Tl) and NE-102 scintillators are shown in Figs. 41 and 42. These results are similar to the gamma scans with stilbene detectors. The figures are superpositions of unretouched computer printouts from a program written to correct for buildup of fission- and

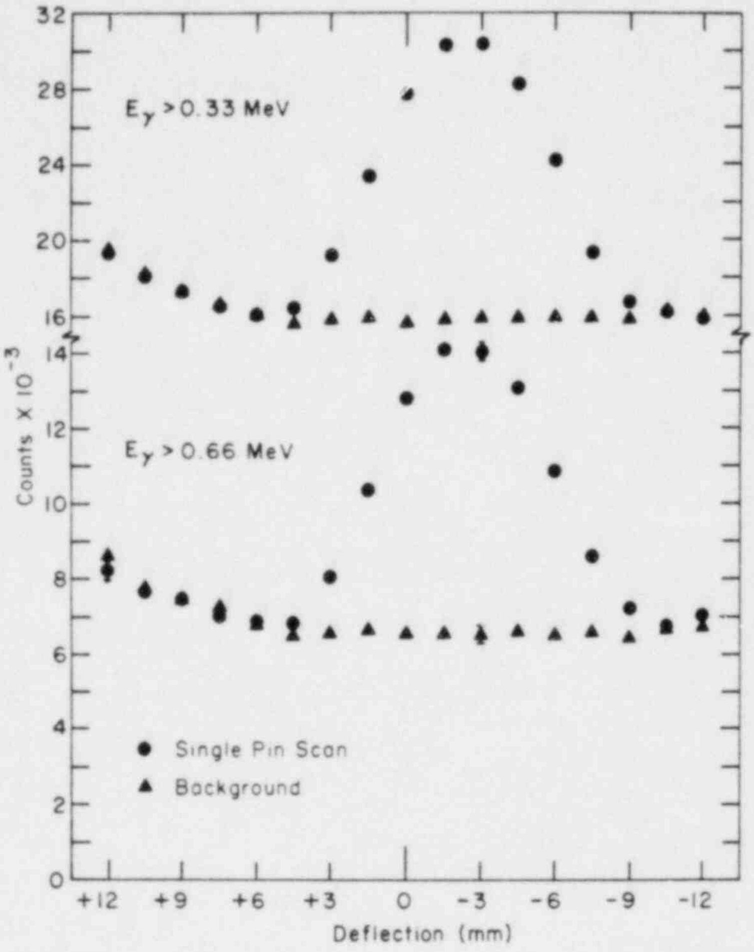

Fig. 38.
Gamma-ray scan with stilbene of a single fuel pin.

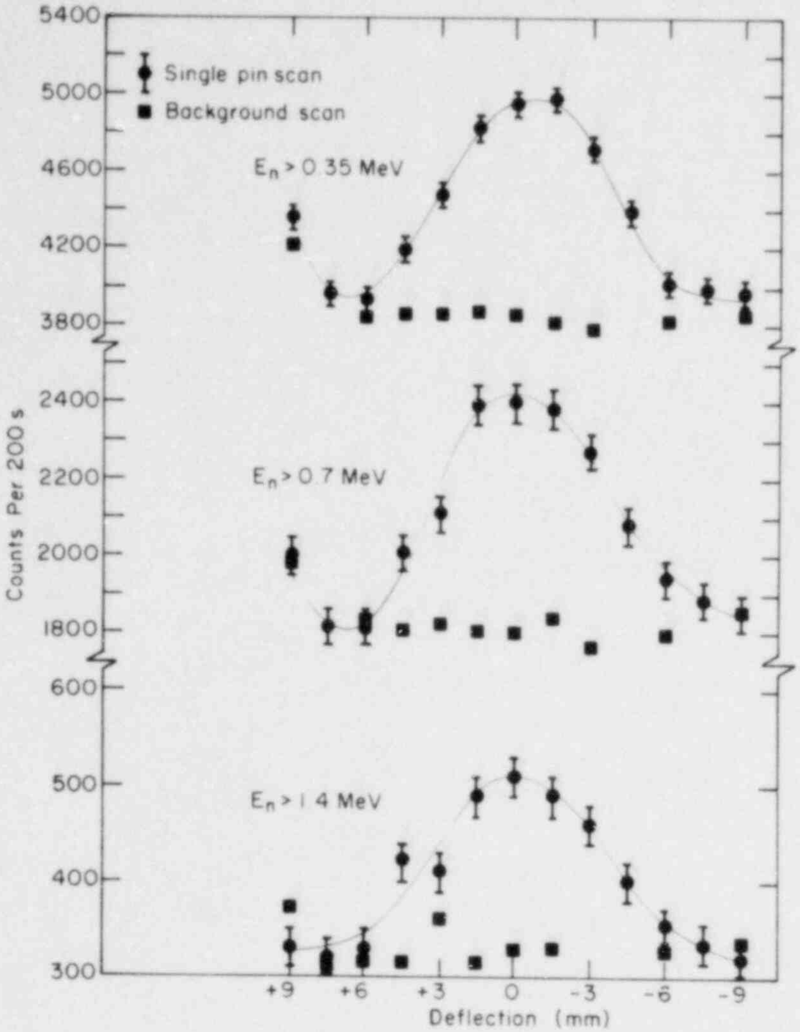

Fig. 39.
Neutron scan of a single pin with a ^{4}He-recoil proportional counter at various threshold energies.

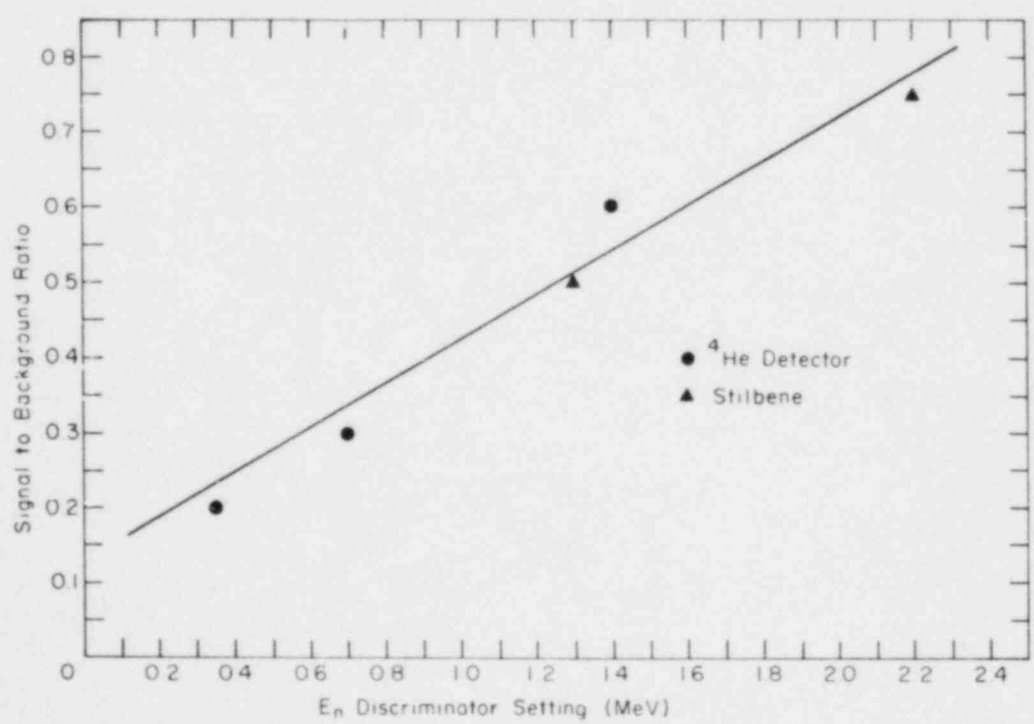

Fig. 40.
Effect of neutron energy bias on the S/B ratio of hodoscope scans of a single fuel pin.

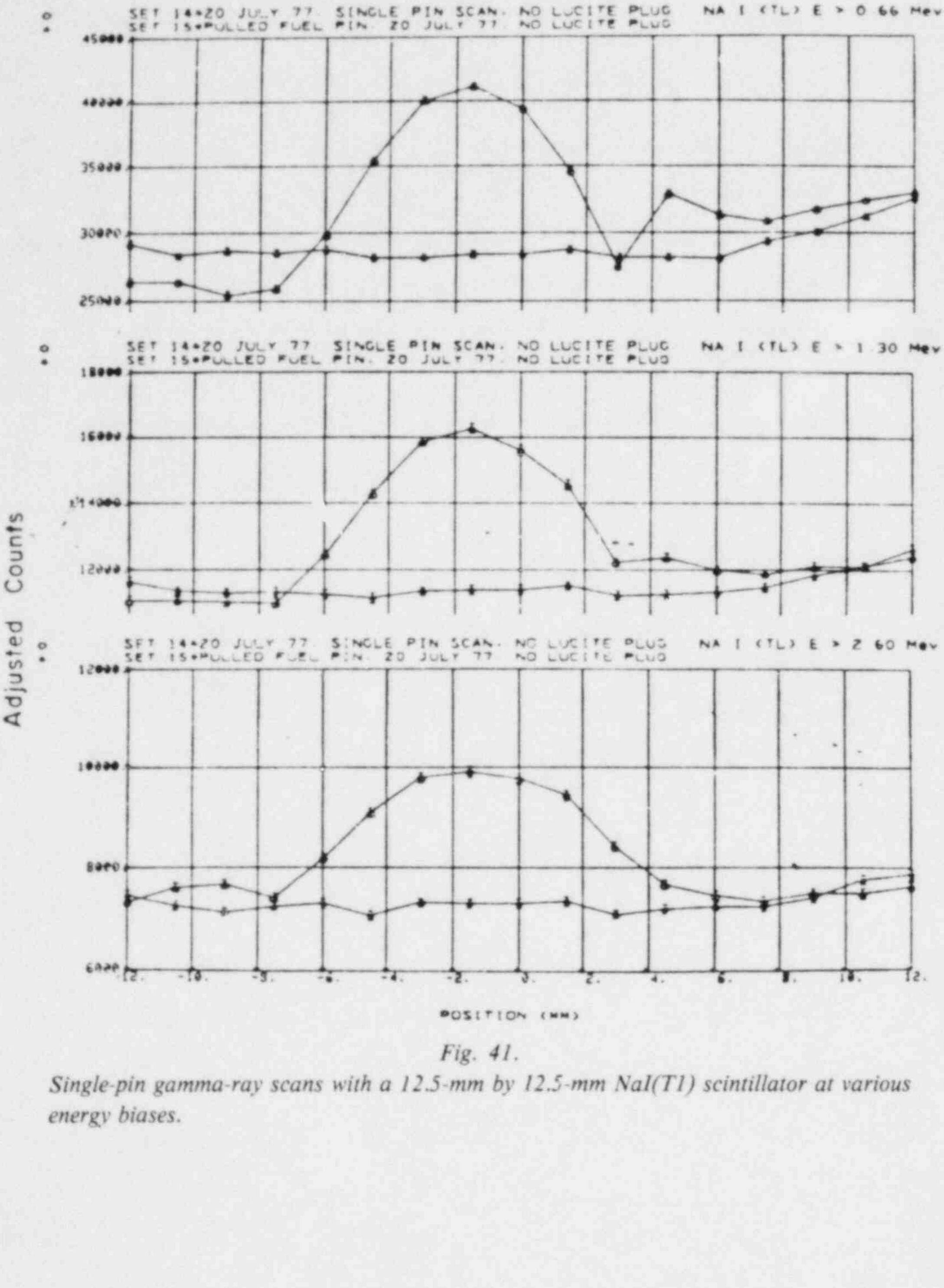

Fig. 41.
Single-pin gamma-ray scans with a 12.5-mm by 12.5-mm NaI(T1) scintillator at various energy biases.

POOR ORIGINAL

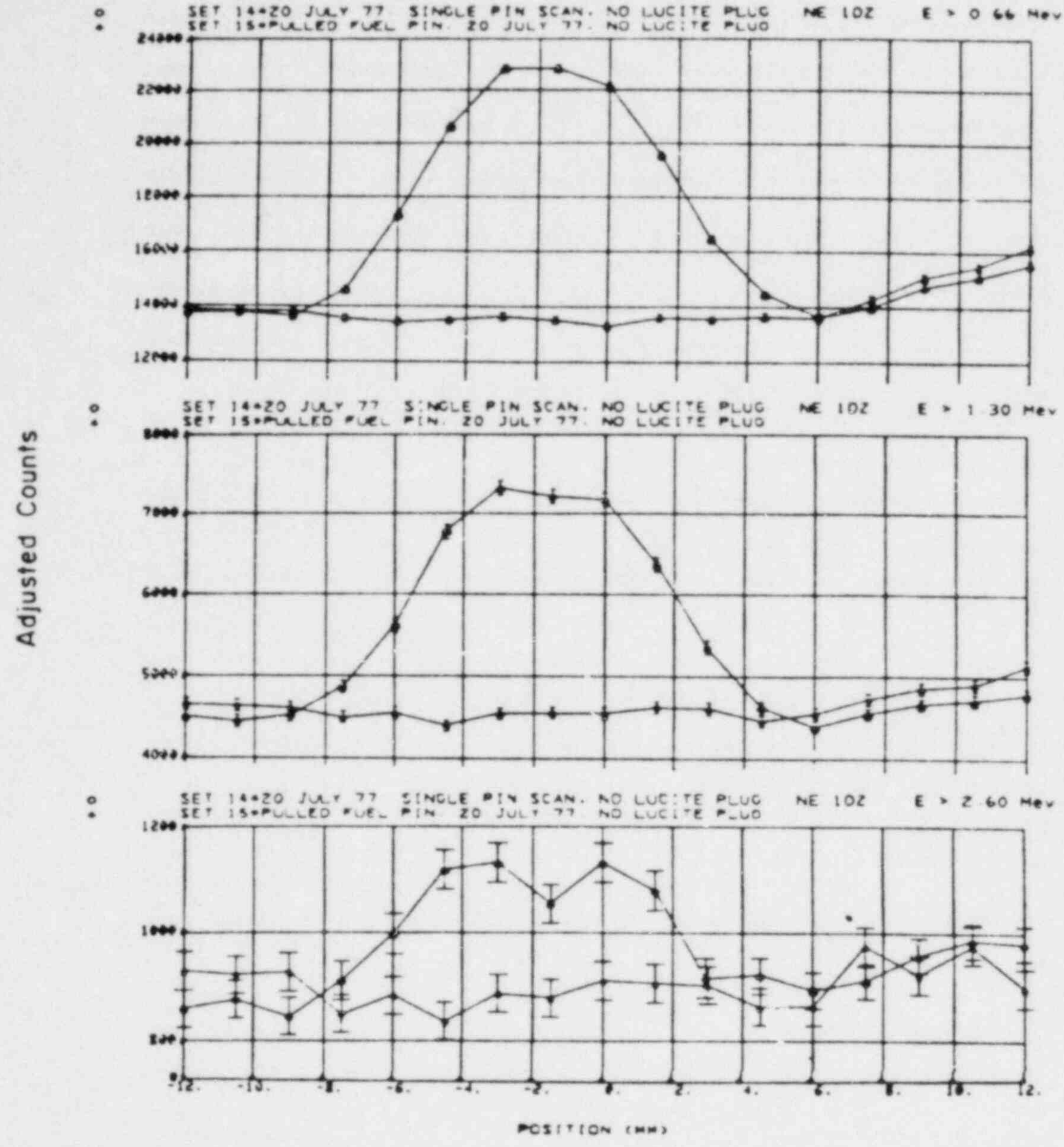

Fig. 42.
Single-pin gamma-ray scans with an NE-102 plastic scintillator at various energy biases.

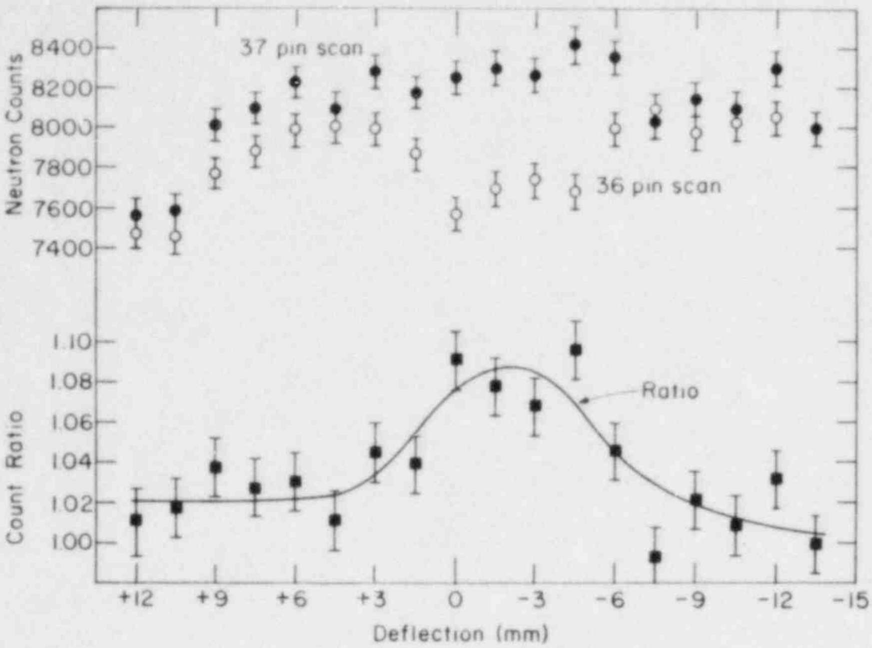

Fig. 43.
Across-flats scans with Hornyak Buttons of a 37-pin assembly, intact and with the center fuel pin withdrawn.

activation-product activity during the scans, normalize for integrated reactor power, calculate statistical errors, and plot the results as a function of scanner position.

B. 37-Pin Assembly Scans

The scanning hodoscope was used with Hornyak Buttons to determine whether one missing pin in a 37-pin assembly could be detected. The results of this test are shown in Fig. 43. The count time for each data point was 200 s. The missing pin produces a 6% decrease in count rate over a distance consistent with the pin diameter and the collimator resolution. It should be noted that the absolute count-rate difference between the 37-pin scan and the 36-pin scan at the center of the missing pin is about 40% of the net count rate from a single pin (Fig. 36). PARKA power levels were identical for the single-pin and 37-pin scans. This indicates the degree to which neutron scattering and absorption may be expected to influence imaging results.

The 37-pin scan was repeated after increasing the thickness of steel around the test assembly to 12.7 mm and filling the space between the fuel pins with drilled aluminum discs. The aluminum is a reasonable neutronic substitute for sodium. The result (Fig. 44) was little different from that obtained previously. There was a drop of ~10% in total count rate, but no apparent loss in resolution.

Stilbene detectors biased for 0.33- and 0.66-MeV gamma rays (1.3- and 2.2-MeV neutrons), were used for across-flats scans of a 37-pin assembly, intact and with the center pin missing. The neutron and gamma-ray count data (Fig. 45) were taken during a 3-h run starting immediately after reaching operating power. The count-rate increase with time for the gamma-ray and lower-energy neutron scans is caused by buildup of fission and activation products. It should be noted that both scans were taken from left to right and that the 36-pin scan followed the 37-pin scan. We subsequently found that most of this problem may be eliminated by running PARKA at the experimental power level for 1 h before starting to take data. One may, if desired, also measure this time-dependent buildup and correct for it. This effect is, of course, less important to the performance of multichannel hodoscopes, with which all data are taken simultaneously.

The time-related buildup for the scan with $E_n > 1.3$ MeV is probably due to incomplete separation of neutron and gamma-ray counts caused by slight overlap of

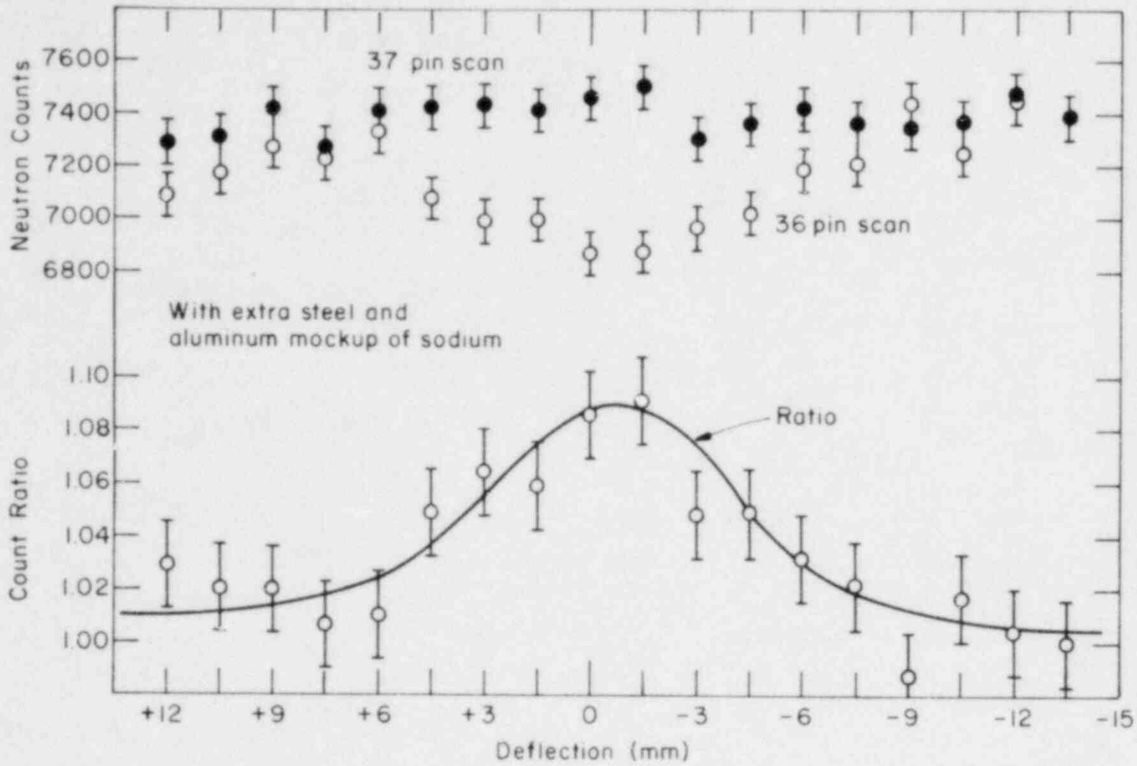

Fig. 44.

Across-flats scans with Hornyak Buttons of a 37-pin assembly, intact and with the center pin withdrawn, with aluminum mockup of sodium and 12.7 mm-thick steel casing.

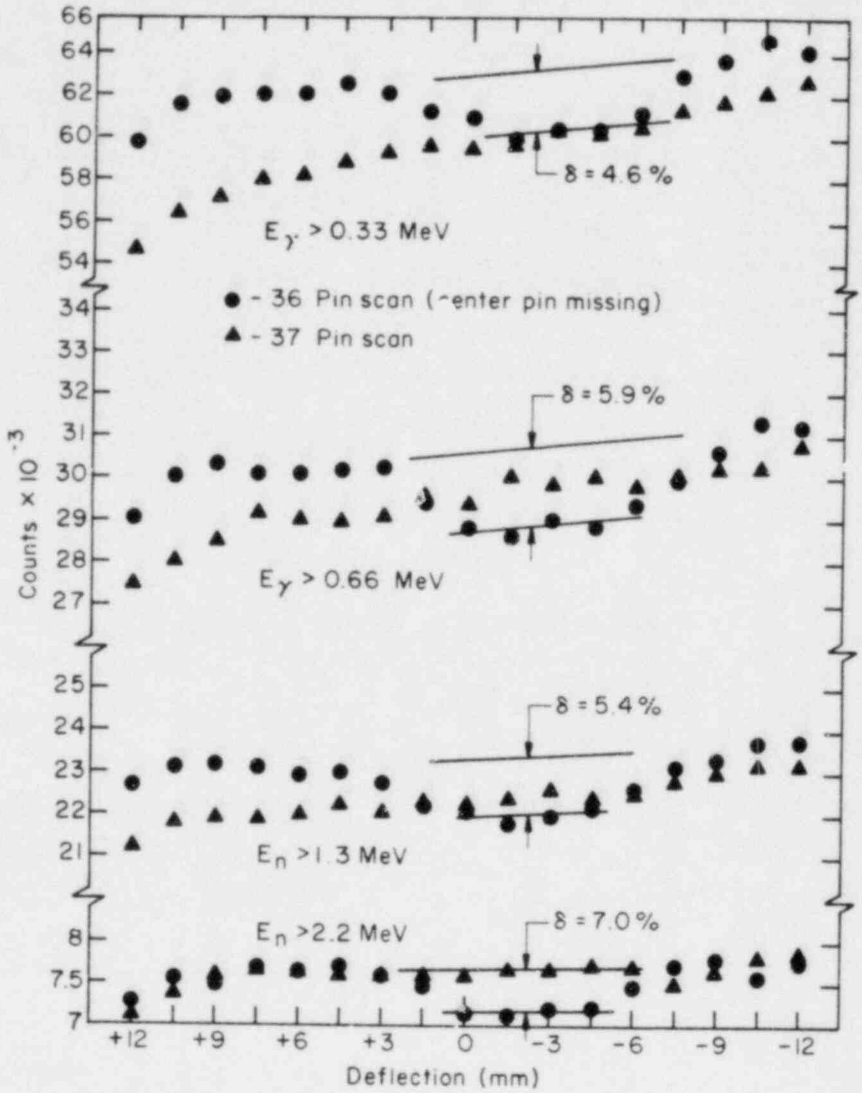

Fig. 45.
Across-flats scans with stilbene detectors of a 37-pin assembly, intact and with the center pin withdrawn.

pulse-risetime distributions as measured by the pulse-shape analyzer. One might also expect contamination of the gamma-ray scan data by neutrons that are captured or inelastically scattered in the vicinity of the detectors and are then indirectly "seen" as gamma-ray events. To test for intermixing of gamma- and neutron-induced counts in the detectors, 37-, 36-, 1-, and 0-pin scans were repeated with 20-cm-long Lucite plugs inserted into the reactor end of the hodoscope collimator holes. The effect of the Lucite plugs on gamma-ray and neutron counting rates is listed in Table II. Crude estimates would indicate that the attenuation should be ~3 for reactor gamma rays and 2 to 3 orders of magnitude for fast neutrons. We also note that most of the neutron counts for the 0-pin, Lucite-plugged case are due to room background rather than to neutrons coming down the collimator, which explains the apparent lower attenuation of these neutrons by the Lucite plugs.

The data of Table II show that the absolute neutron count loss caused by withdrawing one pin from the 37-pin assembly is less than one-half of the net count (with background subtracted) from a single pin in the test section. For gamma radiation, the situation is much worse: the count loss due to withdrawal of one pin from 37-pin bundle is less than one-fourth of the net count from a single pin in the test section. This raises questions concerning the hodoscope's response linearity and its sentitivity to the position of a perturbation in fuel density within the test bundle.

We investigated the position sensitivity by scanning a 37-pin bundle with a pin withdrawn from the center, the front (nearest the collimator), and the back. The results (Fig. 46) show a general reduction in sensitivity from front to back of 20-30% for fast-neutron scans and 35-50% for gamma scans. The center (20-mm) points have been corrected for a known 15% power distribution depression in the center of the test bundle. The indicated errors are from counting statistics only.

TABLE II

RESULTS OF TEST FOR INTERMIXING OF DETECTOR COUNTS INDUCED BY GAMMA RAYS AND NEUTRONS

Scan	Counts per 200 s at 5 mW/g ^{235}U — Collimator Open	Counts per 200 s at 5 mW/g ^{235}U — Collimator Plugged with Lucite	Attenuation
37-pin, $E_n > 2.2$ MeV	7 720	450	17.0
37-pin, $E_n > 1.3$ MeV	23 400	1 300	18.0
37-pin, $E_\gamma > 0.66$ MeV	30 700	10 600	2.9
37-pin, $E_\gamma > 0.33$ MeV	63 400	19 300	3.3
36-pin, $E_n > 2.2$ MeV	7 180	400	18.0
36-pin, $E_n > 1.3$ MeV	22 050	1 250	18.0
36-pin, $E_\gamma > 0.66$ MeV	28 900	10 000	2.9
36-pin, $E_\gamma > 0.33$ MeV	60 400	18 200	3.3
1-pin, $E_n > 2.2$ MeV	2 800	175	16.0
1-pin, $E_n > 1.3$ MeV	9 100	600	15.0
1-pin, $E_\gamma > 0.66$ MeV	14 000	5 400	2.6
1-pin, $E_\gamma > 0.33$ MeV	30 400	10 000	3.0
0-pin, $E_n > 2.2$ MeV	1 600	110	14.5
0-pin, $E_n > 1.3$ MeV	6 000	450	13.3
0-pin, $E_\gamma > 0.66$ MeV	6 500	3 200	2.0
0-pin, $E_\gamma > 0.33$ MeV	16 000	6 200	2.6

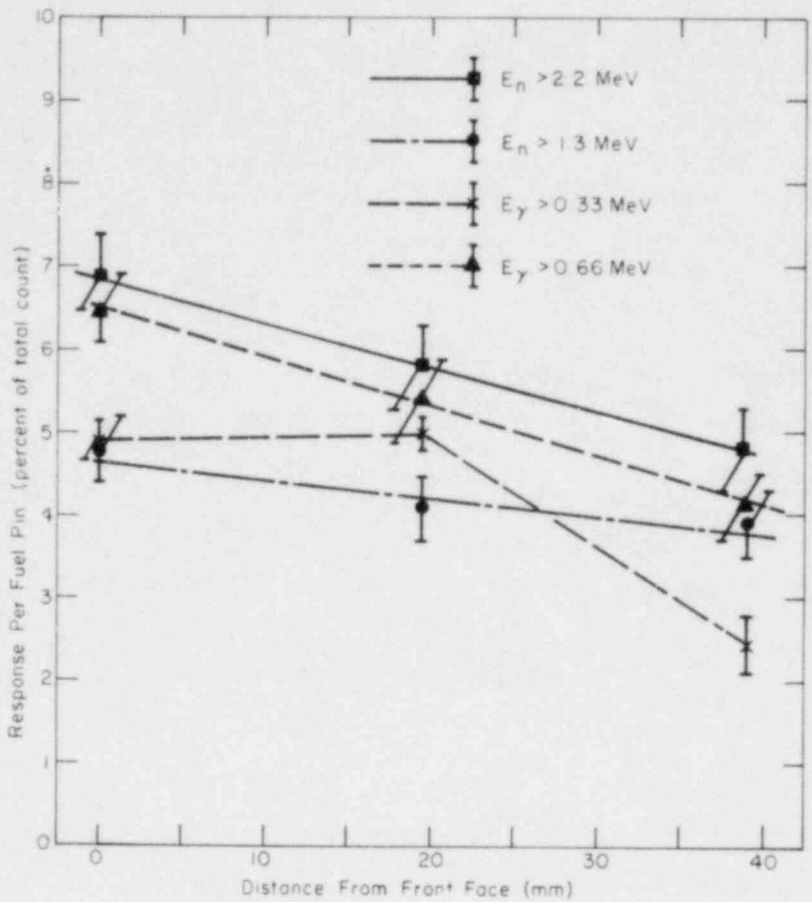

Fig. 46.
Sensitivity of hodoscope response with stilbene detectors to fuel-pin removal from a 37-pin assembly as a function of the position of the void in the assembly.

Response linearity was tested by scanning with one to four pins withdrawn in line from the assembly. The results are shown in Fig. 47 for neutrons and in Fig. 48 for gamma rays. The neutron scans (Fig. 47) exhibit linear response within the indicated statistics but the gamma scans (Fig. 48) show a slight (5-10%) increase in response over linearity.

The 37-pin assembly with zero to four pins withdrawn was scanned across flats with ^{4}He-recoil detectors at an energy threshold of 0.35 MeV (Fig. 49). The response linearity with these detectors at various energy thresholds is shown in Fig. 50. The ^{4}He recoil detectors are far less sensitive to background gamma rays and thermal neutrons than either the stilbene detectors or the Hornyak Buttons. With 20-cm-long Lucite plugs blocking the hodoscope channels, we found the ^{4}He-recoil detector count rates attenuated by factors of from 40 to 64, compared to 15 and 18 for stilbene detectors. Doubling the length of the Lucite plug showed that only 1 or 2% of the counts from the ^{4}He-recoil detectors were due to room background.

The ^{4}He-recoil detectors have too low a counting efficiency for fission-spectrum neutrons to be of regular use in PARKA hodoscope experiments, but their insensitivity to gamma rays and thermal neutrons may make them candidates for use at STF power levels. They do, however, have a longer pulse risetime (1-2μs) than do plastic scintillators, which may cause nonlinearity at high count rates. Furthermore, ^{4}He-recoil detectors seem to have less long-term stability than do stilbene and Hornyak-Button scintillators.

Figures 51 and 52 show computer-generated plots of across-flats scans with NaI(Tl) and NE-102 scintillators of the 37-pin assembly, intact and with the center pin withdrawn. These data have been corrected for time-dependent buildup of fission-product background and activation of the NaI(Tl) detector. Results are little different from those obtained with the stilbene detectors.

POOR ORIGINAL

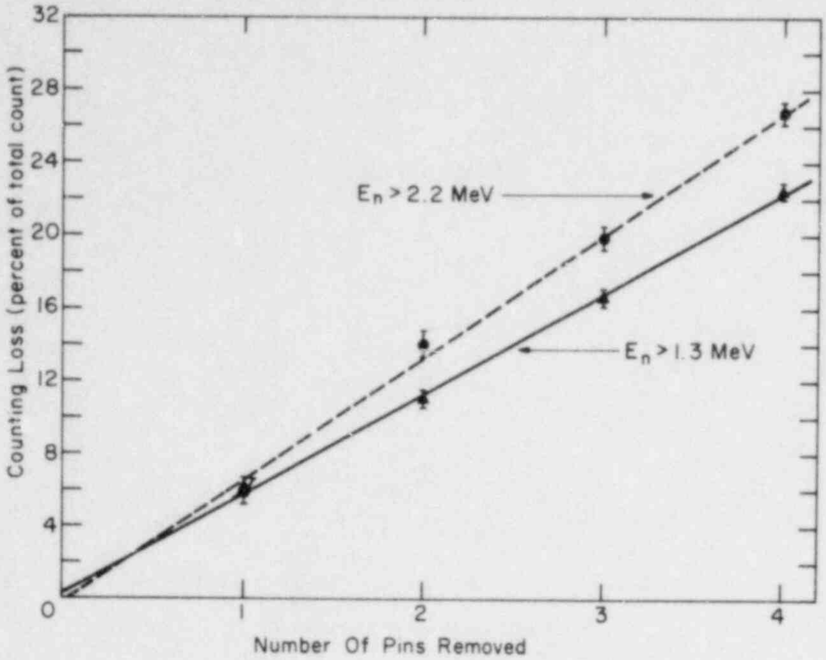

Fig. 47.
Linearity of hodoscope neutron response with stilbene detectors to fuel-pin removal from a 37-pin assembly.

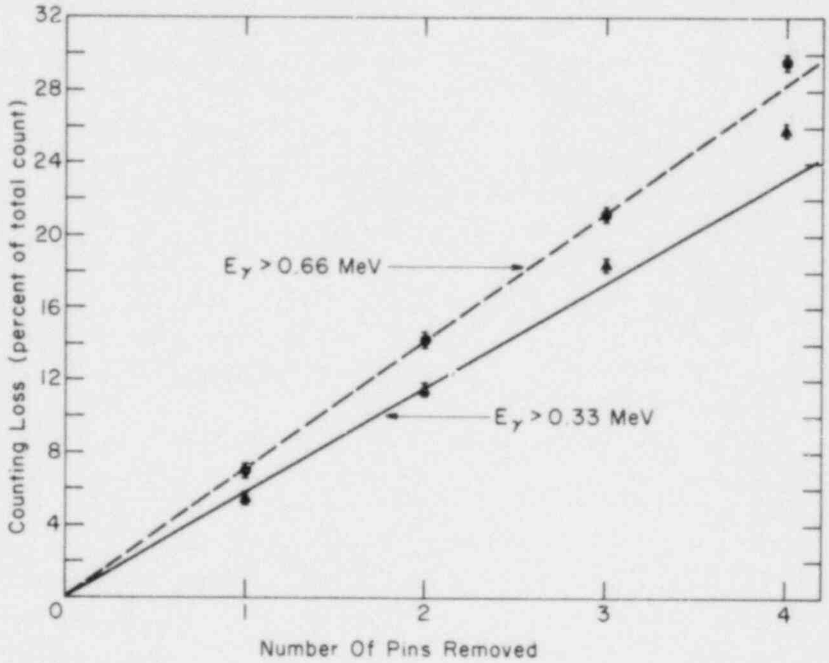

Fig. 48.
Linearity of hodoscope gamma-ray response with stilbene detectors to fuel-pin removal from a 37-pin assembly.

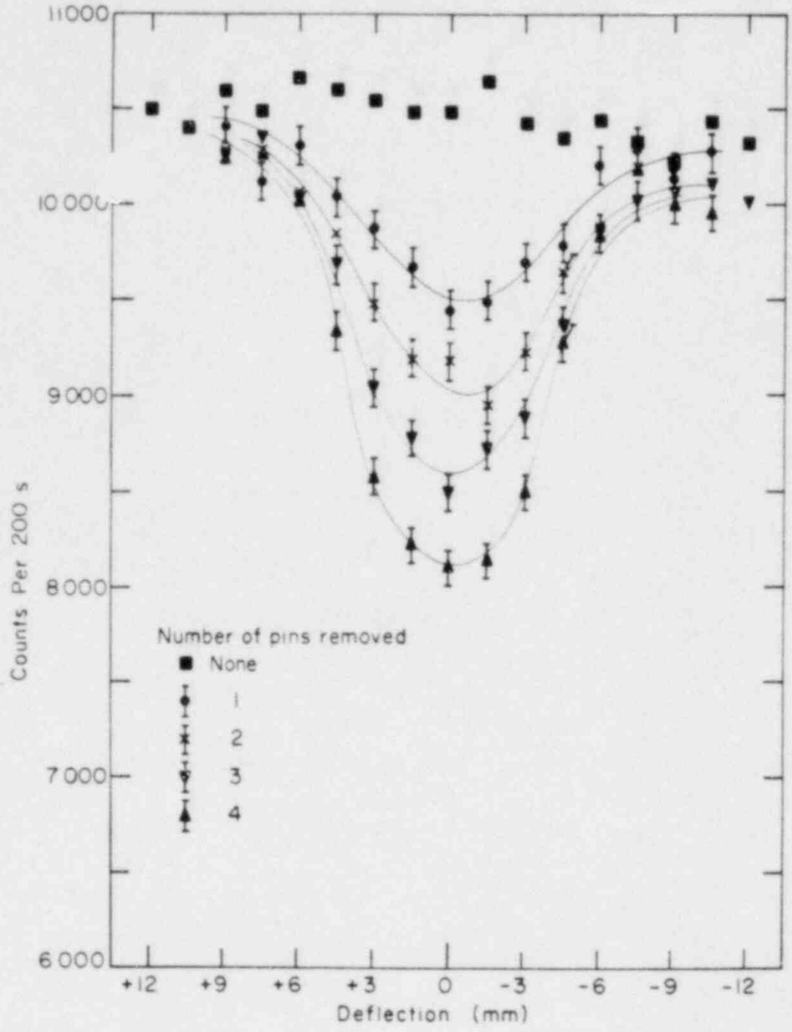

Fig. 49.
Neutron scans with ^{4}He-recoil detectors at an energy threshold of 0.35 MeV of a 37-pin assembly with up to four pins removed in line.

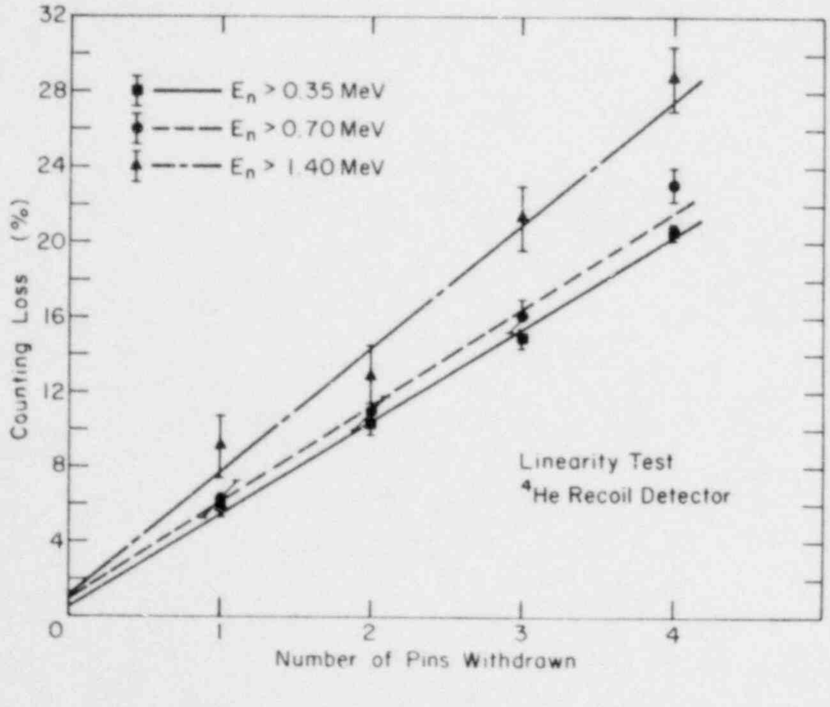

Fig. 50.
Linearity of hodoscope neutron response with ^{4}He-recoil detectors at various energy thresholds to fuel-pin removal from a 37-pin assembly.

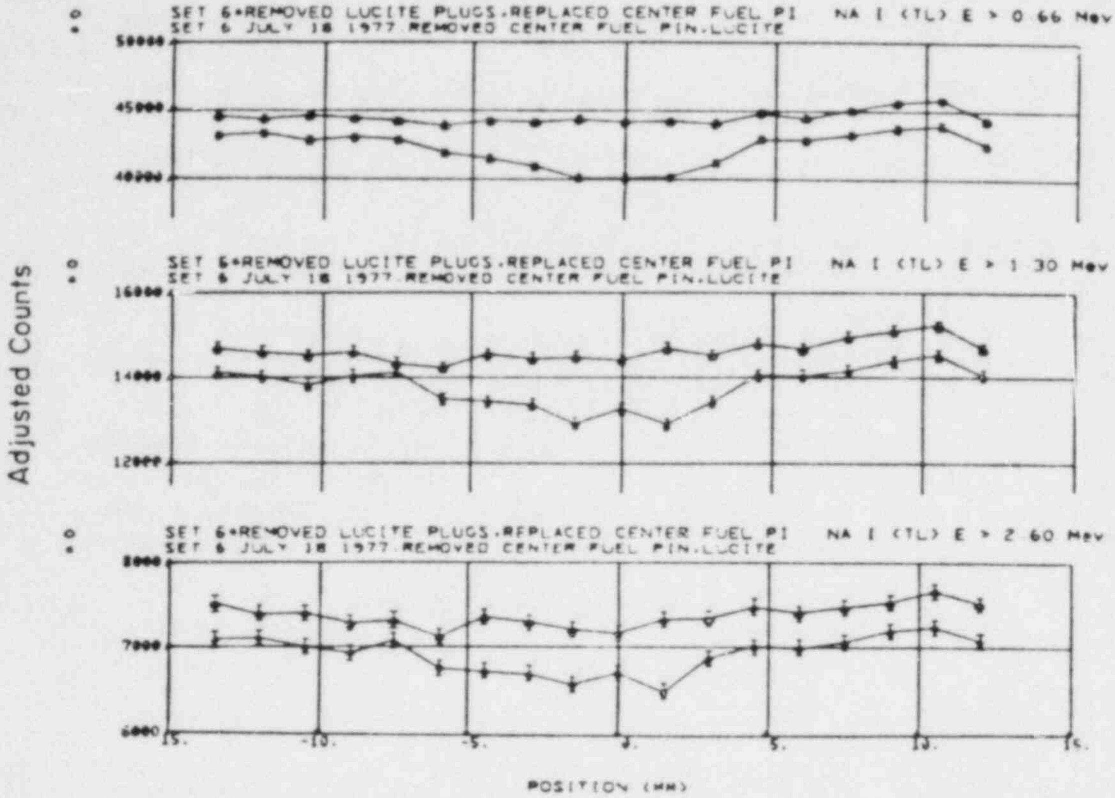

Fig. 51.
Across-flats scans with NaI(Tl) of a 37-pin assembly, intact with the center pin removed.

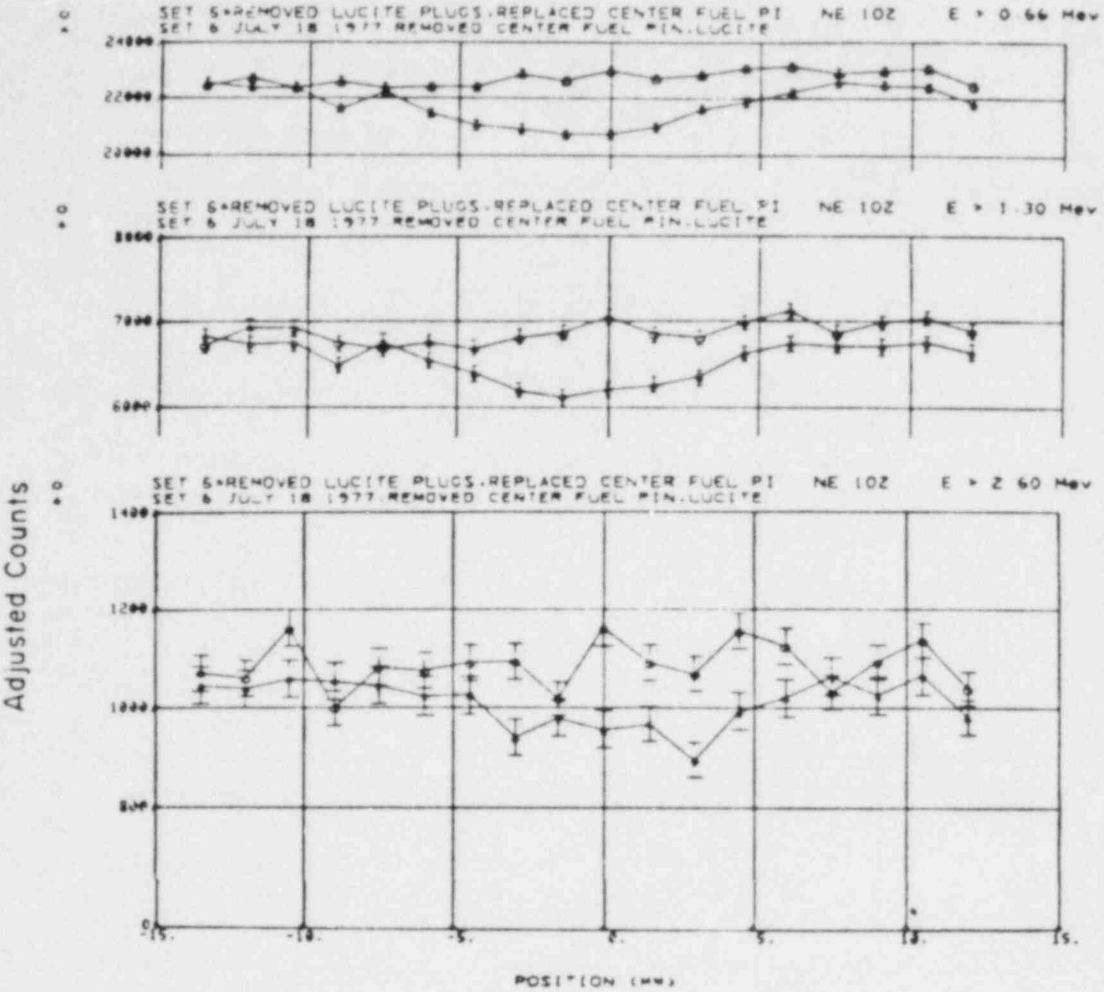

Fig. 52.
Across-flats scans with NE-102 of a 37-pin assembly, intact and with the center pin removed.

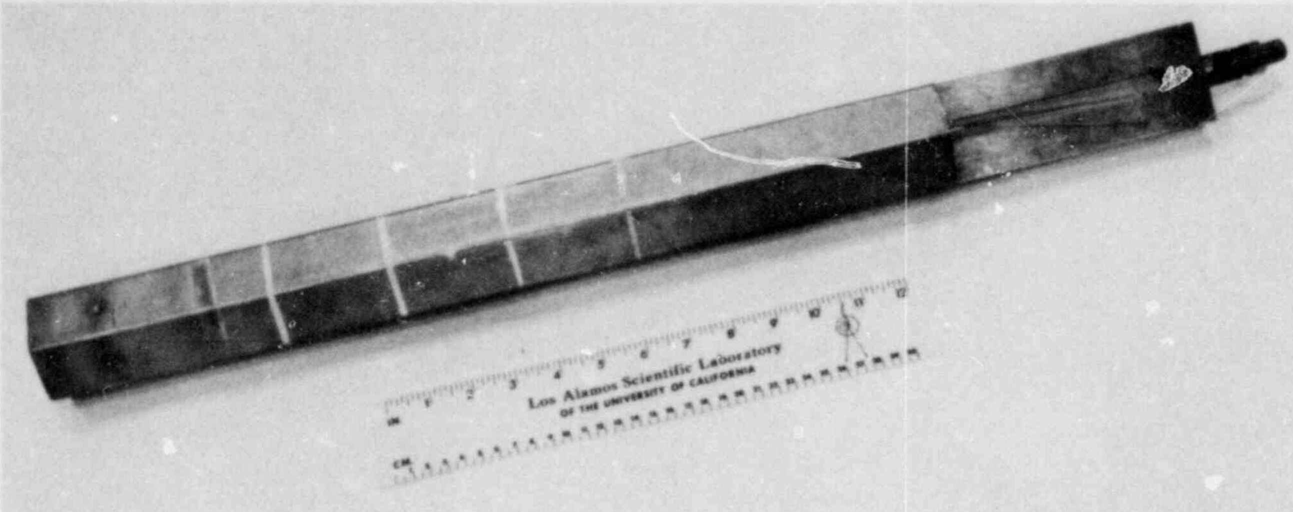

Fig. 53.
Mockup of the 91-pin EBR-II fuel assembly.

C. 91-Pin Assembly Scans

In a joint experiment[20] with Argonne National Laboratory, a 91-pin EBR-II fuel assembly was scanned. This assembly (Fig. 53) consisted of an array of wire-wrapped fuel pins in a hexagonal stainless-steel can with an outside dimension of 5.82 cm across flats. The fuel pins, each consisting of 3.56-mm-diam by 69-mm-long pellets of 52%-enriched UO_2 fuel loaded into 0.38-mm-thick cladding, were assembled into a hexagonal bundle with a spacing of 5.6 mm between centers. A void and a steel dummy replaced two pellets in each of three "flawed" pins. Figure 54 shows the positions of the flawed fuel pins in the bundle and the layout of the void and steel dummy in a flawed fuel pin. The flaws could be aligned with the field of view of the hodoscope. The assembly was mounted on remotely operated precision rotation and vertical positioners. By rotating the bundle, scans could be made through the three flawed pins aligned on a major diameter of the hexagon or through only the center defect either across flats or across corners. By using two vertical channels of the hodoscope, scans could be made simultaneously through a perfect and a faulted section of the assembly. Stilbene detectors and Hornyak buttons were both used.

Twenty-one scans of the EBR-II fuel assembly were made at various neutron and gamma-ray thresholds, looking through one or three flawed pins from various angles. One across-flats scan with stilbene detectors is shown in Fig. 55. The data points are the ratios of the output of one detector scanning across a perfect section to the output of the other detector scanning across a section flawed in the center with a void. The three curves are the neutron, the gamma-ray, and the "total" ($n + \gamma$) scans for $E_\gamma > 0.3$ MeV. The neutron scan shows a clear 3.5% difference in ratios over the diameter of the missing pellet (detector sensitivities were not normalized, so the base-line ratio is not unity). It is also clear that the gamma-ray scan does not reveal the missing pellet. As should be expected, summing the gamma-ray and neutron data serves only to dilute the neutron data, therby degrading the sensitivity of the hodoscope.

Other results of these experiments have been reported in detail elsewhere.[20-22] The tests showed that it is possible to detect a pellet-sized void in an assembly of this size by means of a fast-neutron hodoscope, that hodoscope image resolution improves with increasing neutron energy (from 1 to 3 MeV), and that gamma-ray self-imaging of an assembly of this size and complexity is inferior to neutron self-imaging.

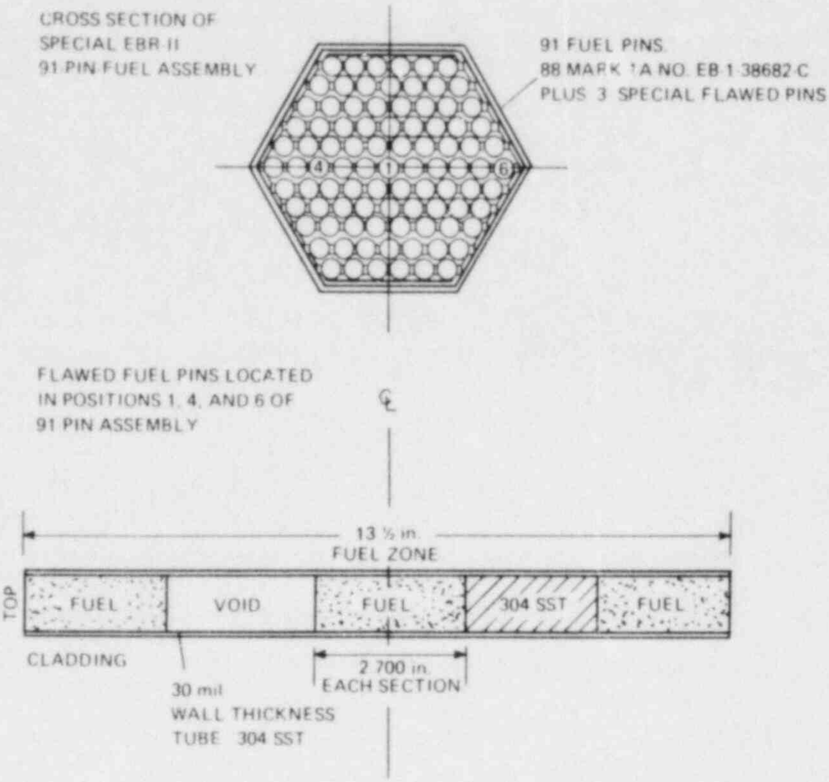

Fig. 54.
Locations and details of flawed pins in the 91-pin EBR-II test assembly.

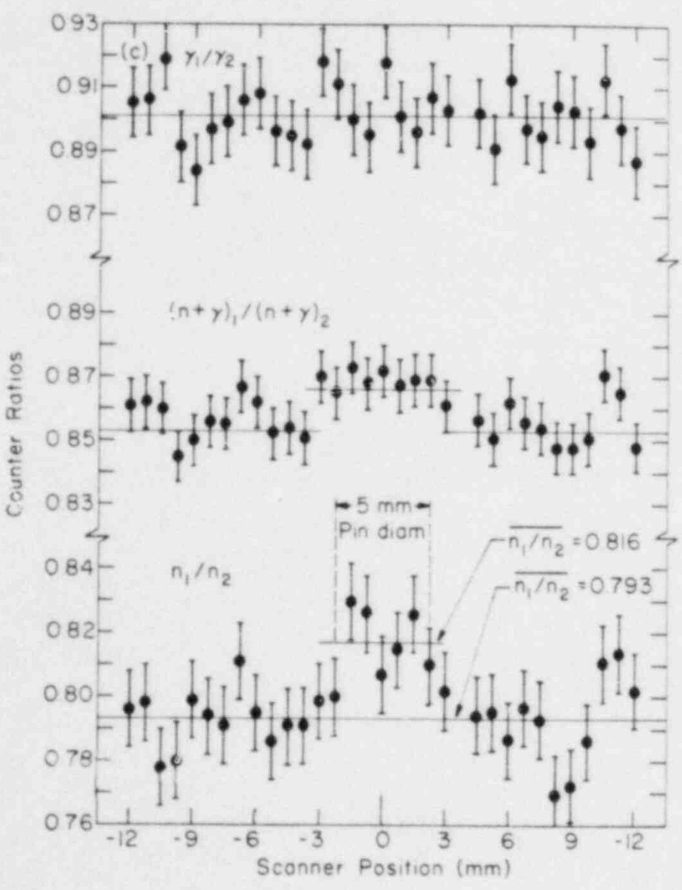

Fig. 55.
Across-flats neutron, gamma, and total scans with stilbene detectors of a flawed 91-pin EBR-II assembly. Data points are the ratios of the output of one detector scanning across a perfect section to the output of the other detector scanning across a section flawed in the center with a void.

D. 127-Pin Assembly Scans

With stilbene detectors biased as in the 37-pin assembly scans, a 127-pin assembly with FFTF-sized pin dimensions and spacing has been scanned across flats and across corners of the hexagon, intact and with pins removed at various depths in the assembly. Shown in Fig. 56 are across-flats scans of the assembly intact and with the center pin withdrawn. The count time was 200 s for each data point at 5 mW/g ^{235}U operating power. (Note that counts/200 s at 5 mW/g ^{235}U is equivalent to counts/(J/g ^{235}U))—a fortuitous choice!) To better show the effect of withdrawing the pin, the ratios of pin-out to pin-in counting rates are plotted in Fig. 57. The fast-neutron signal from the fuel in the center pin, averaged over the diameter of the pin, is approximately 2% of the total count rate. Using the known vertical resolution (to half-maximum intensity) of the hodoscope slot (19.05 mm) and the known ^{235}U content of the fuel pin, we calculate that the observed count reduction was caused by the removal of 2.94 g of ^{235}U from the hodoscope field of view, which is comparable to the established requirements for mass resolution for single-subassembly tests.[3]

Figure 58 shows a scan across a corner of the assembly. Such a scan exhibits definite maxima and minima because the scan direction is perpendicular to the fuel-pin rows. Since the distance between fuel rows (6.29 mm) is less than the horizontal resolution (to half-maximum intensity) of the hodoscope slot (7.14 mm), the hodoscope slot actually "sees" more fuel when the slot is centered between two rows than when the slot is centered on a row. As result, a count minimum occurs when the hodoscope slot is pointed directly at a row of pins.

Figure 58 also shows the effects of withdrawing the central pin or the corner pin nearest the hodoscope. As discussed above, some of the difference in response

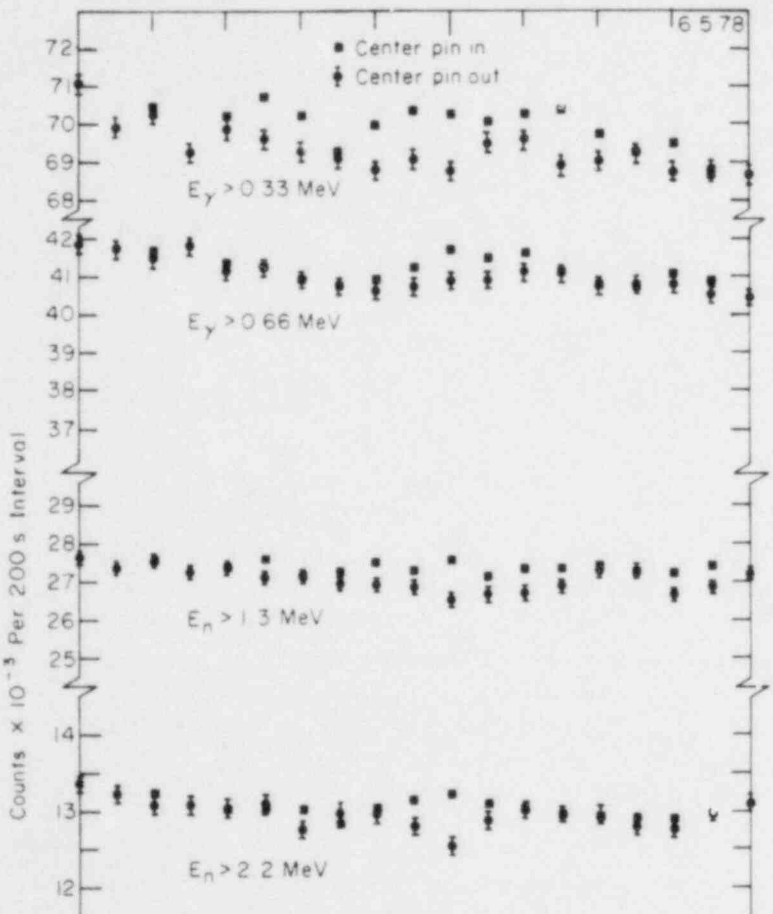

Fig. 56. Across-flats scans with stilbene detectors of a 127-pin assembly, intact and with the center pin withdrawn.

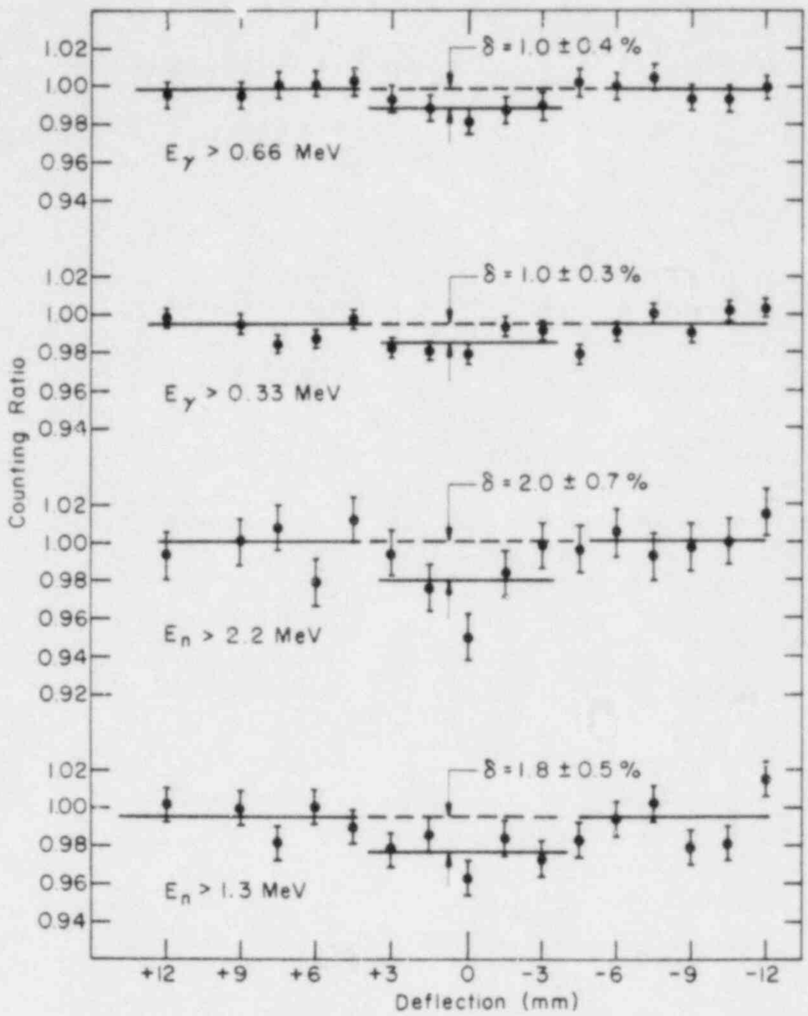

Fig. 57.
Data of Fig. 56, expressed as ratios of pin-out to pin-in count rates.

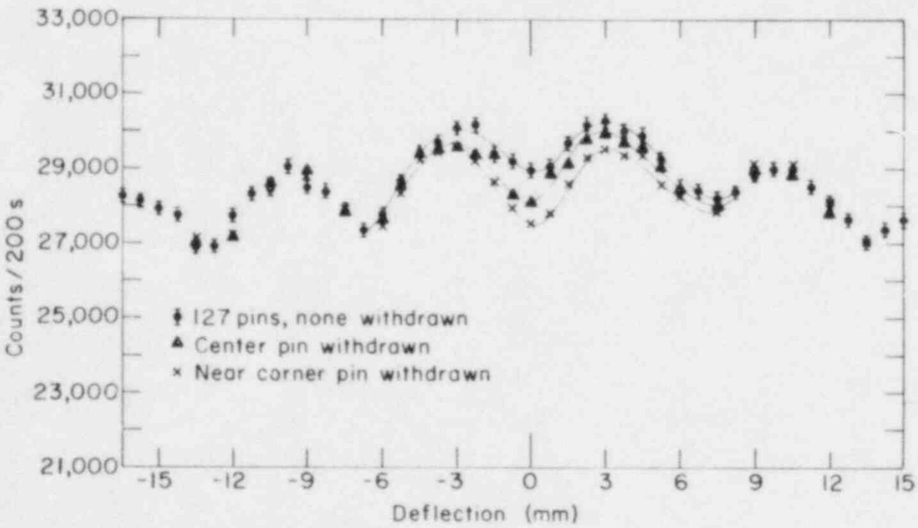

Fig. 58
Across-corners scans with stilbene detectors biased at E_n > 1.3 MeV of a 127-pin assembly, intact and with the center or near-corner pin withdrawn.

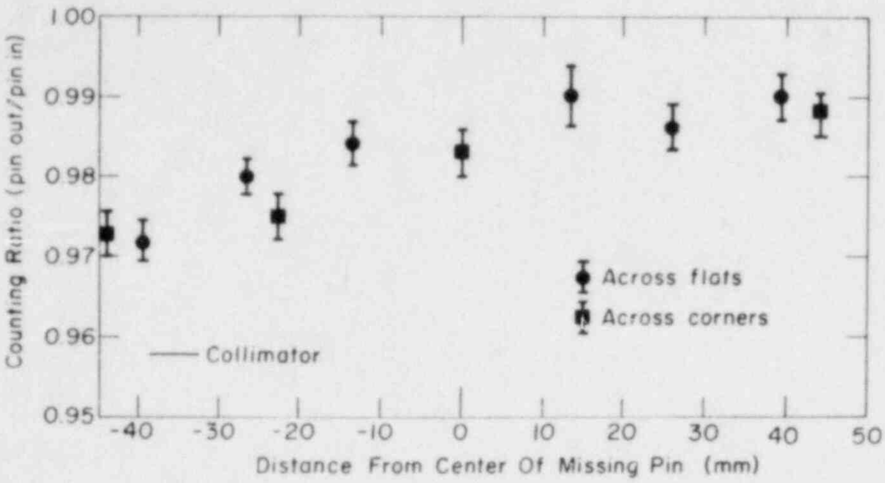

Fig. 59.

Ratio of pin-out to pin-in count rates of a stilbene detectors biased at $E_n >$ 1.3 MeV as a function of void position in a 127-pin assembly.

between the two pin locations is due to the power distribution within the assembly. It is evident, however, that the response of the hodoscope to a void is not independent of the position of the void within the test assembly. Figure 59 shows pin-out to pin-in count-rate ratios for across-flats and across-corners scans of the assembly with a single missing pin at various depths within the bundle. The data, taken with a stilbene detector biased for $E_n > 1.3$ MeV, show that the total count-rate reduction for a single-pin void in a 127-pin assembly varies from 3% for a void at the near edge of the assembly to 1% at the far edge. These data, which have been corrected for the measured power distribution within the assembly, show the need for a detailed static hodoscope study of every large test assembly before the destructive experiment is run. The need for three-dimensional data, as from crossed hodoscopes, is also evident.

E. Effect of Test-Capsule Wall Thickness

Of considerable importance to experiment planning is the effect on the fuel image of the wall thickness of the capsule used to enclose the test assembly. A tradeoff may be necessary between safety of the experiment and amount of image degradation that can be tolerated within experimental objectives. To study this problem, the 127-pin assembly was replaced with a 37-pin assembly surrounded by a 21-mm-thick steel casing. The steel occupies the space between the 37-pin grid and the inside wall of the 127-pin test chamber. This 20-cm-long casing can be remotely raised from and lowered into the field of view of the hodoscope.

Table III lists the results of across-flats scans with stilbene detectors of the 37-pin assembly, with and without the casing and with and without a center void. The steel casing causes a loss in total signal and background of about 30% for fast neutrons and nearly 50% for gamma rays. More important is the fact that the casing decreases the mass resolution by ~33% for fast neutrons and by ~48% for gamma rays. Also listed in Table III are the mass-resolution decreases for 25- and 50-mm-thick steel capsules calculated by assuming that the effect varies exponentially with wall thickness.

Figure 60 displays across-corners fast-neutron scans of the 37-pin assembly, with and without the casing and with and without voids at the center and far corner. As discussed above, a count-rate minimum occurs for this orientation when the collimator is pointed directly at a row of fuel. The degree to which the details of the scan are degraded by the casing is obvious. Similar gamma-ray scans with energy thresholds of 0.33 and 0.66 MeV are shown in Figs 61 and 62. As expected, the degrading effect of the steel on these gamma-ray images, particularly for the lower-energy threshold, is more pronounced than for the neutron images.

Because the effective thickness of intervening steel is greater for scans away from the center line of the cylindrical casing, it was felt desirable to repeat the above experiment with pins removed from the side of the assembly, rather than from the center. The neutron and

TABLE III

EFFECT OF A 21-mm-THICK STEEL CASING ON HODOSCOPE IMAGES OF A 37-PIN ASSEMBLY

	$E_\gamma > 0.66$ MeV	$E_\gamma > 0.33$ MeV	$E_n > 2.2$ MeV	$E_n > 1.3$ MeV
Count rate[a] of intact assembly, without casing	38 150	63 200	9 500	19 000
Count rate[a] of assembly with center void and without casing	35 800	59 600	8 900	17 900
Fractional count-rate decrease caused by center void without casing	0.061 ± 0.003	0.056 ± 0.002	0.065 ± 0.006	0.058 ± 0.005
Count rate[a] of intact assembly with 21-mm-thick casing	20 250	34 400	6 300	13 900
Count rate[a] of assembly with center void and with 21-mm-thick casing	19 600	33 400	6 070	13 300
Fractional count-rate decrease caused by center void with 21-mm-thick casing	0.032 ± 0.005	0.029 ± 0.003	0.037 ± 0.007	0.042 ± 0.005
Mass-resolution decrease caused by 21-mm-thick casing	48 ± 8%	48 ± 5%	38 ± 8%	28 ± 4%
Calculated mass-resolution decrease caused by 25-mm-thick casing	54%	54%	43%	32%
Calculated mass-resolution decrease caused by 50-mm-thick casing	78%	78%	68%	54%

[a]Count rate is in units of counts per 200 s at 5 mW/g ^{235}U.

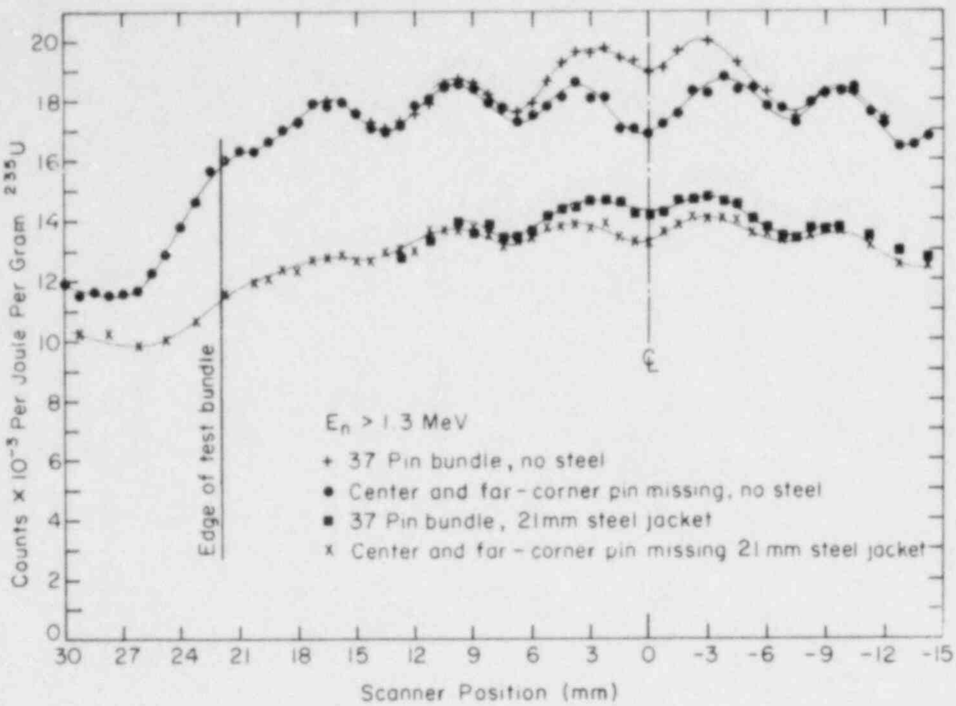

Fig. 60.
Across-corners neutron scans with stilbene detectors (E_n > 1.3 MeV) of a 37-pin assembly, with and without steel casing and with and without voids at the center and at the far corner.

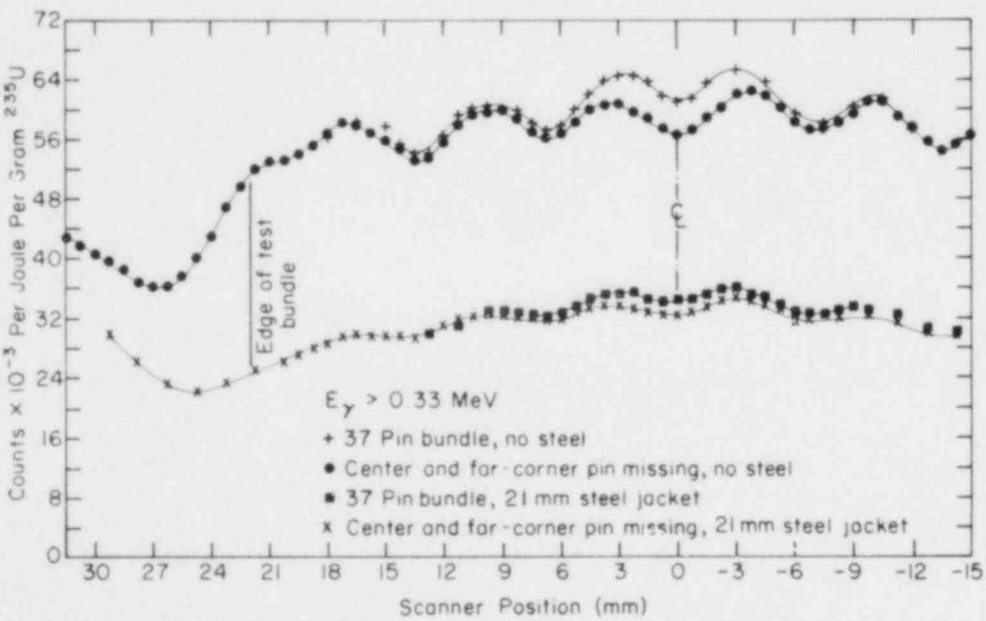

Fig. 61.
Across-corners gamma-ray scans with stilbene detectors (E_γ > 0.33 MeV) of a 37-pin assembly, with and without steel casing and with and without voids at the center and at the far corner.

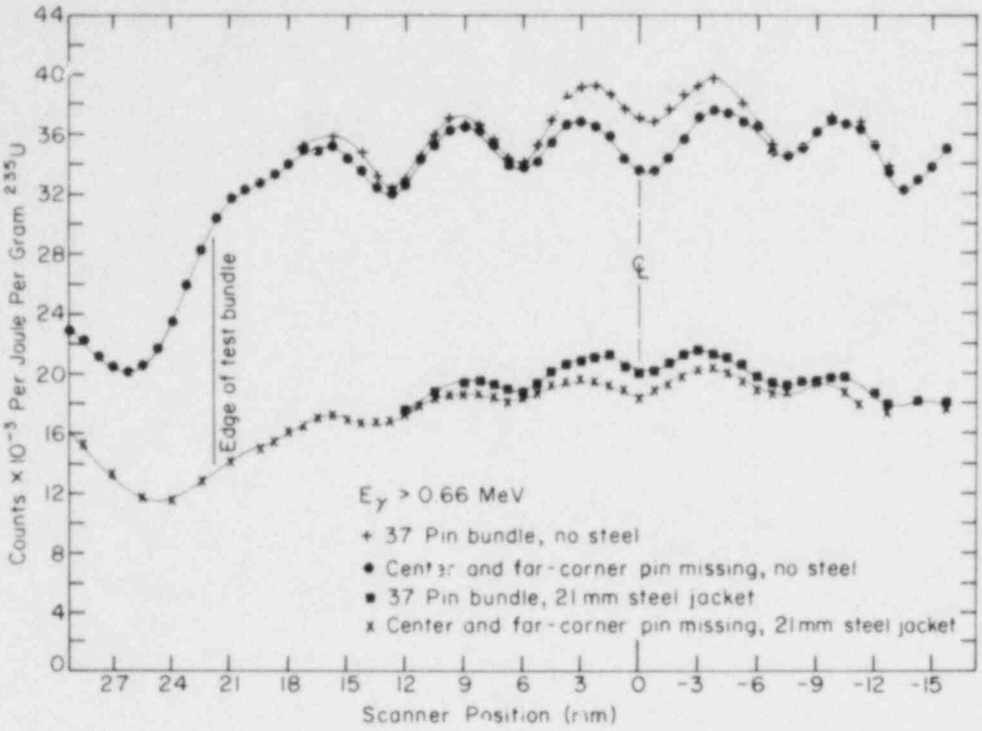

Fig. 62.

Across-corners gamma-ray scans with stilbene detectors (E_γ > 0.66 MeV) of a 37-pin assembly, with and without steel casing and with and without voids at the center and at the far corner.

gamma-ray backgrounds, as sensed by the scanning hodoscope when there is no fuel in the test region, are not uniform across the entire field of view. At the edges, background levels are nearly equal to signal levels from the center of the 37-pin assembly. For this reason and because the major diameter of the 37-pin assembly is greater than the field of view of the hodoscope, it was necessary to displace the test section 19 mm to one side of the axis of the through-slot in PARKA. This was accomplished by removing the test section and its liner from the reactor core, shifting seven PARKA fuel rods, and replacing the test section at its new position.

Figures 63 and 64 show across-corners neutron and gamma-ray scans with stilbene detectors of the off-center 37-pin assembly with and without the steel casing and with and without voids.

The neutron scans of the empty test region show that the casing does not appreciably affect the fast-neutron background in the center of the test region, although it does somewhat flatten the background across the region. At the side edge of the assembly, the steel reduces the neutron signal from the fuel by 40% and thereby reduces the S/B ratio and the mass resolution. The effect is more pronounced for gamma rays. We find the net gamma-ray count rate from the fuel is reduced by more than 50% while the background is undiminished. These effects, for both neutron and gamma-ray imaging, are not appreciably different from those for scans of the assembly center.

Figure 63 also shows that the test assembly causes a 10-15% increase in the neutron background from the test region. This is attributed to a power-distribution shift relative to the flux at the ion chamber being used as a power monitor and controller. The monitoring chamber is external to the reactor core.

F. Studies of Clad-Motion Detection

As discussed in Sec. III.B.2, we had identified the high-energy radiation in the gamma-ray spectrum obtained with a BGO detector as capture gamma rays from iron. This spectrum (Fig. 34) was obtained with the 38-mm BGO detector mounted in front of a collimator slot pointed at the edge of the 37-pin assembly and with the simulated test capsule in place. The use of these capture gamma rays to detect clad motion is hindered by the presence in the experimental setup of various steel

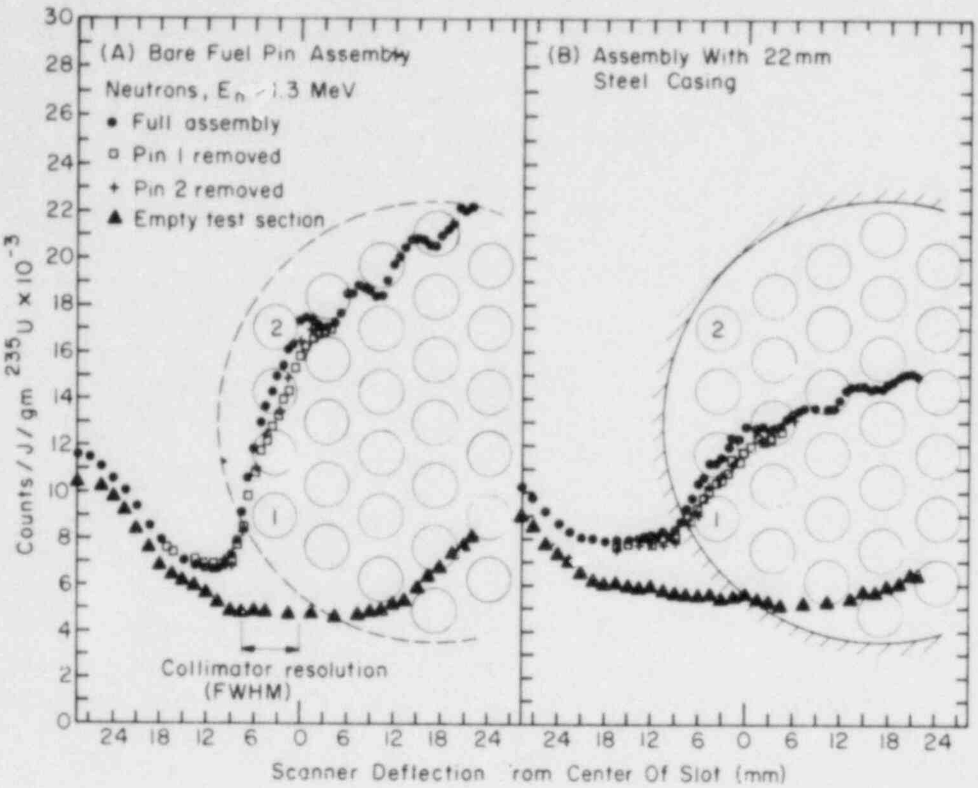

Fig. 63.
Across-corners neutron scans with stilbene detectors of the off-center 37-pin assembly.

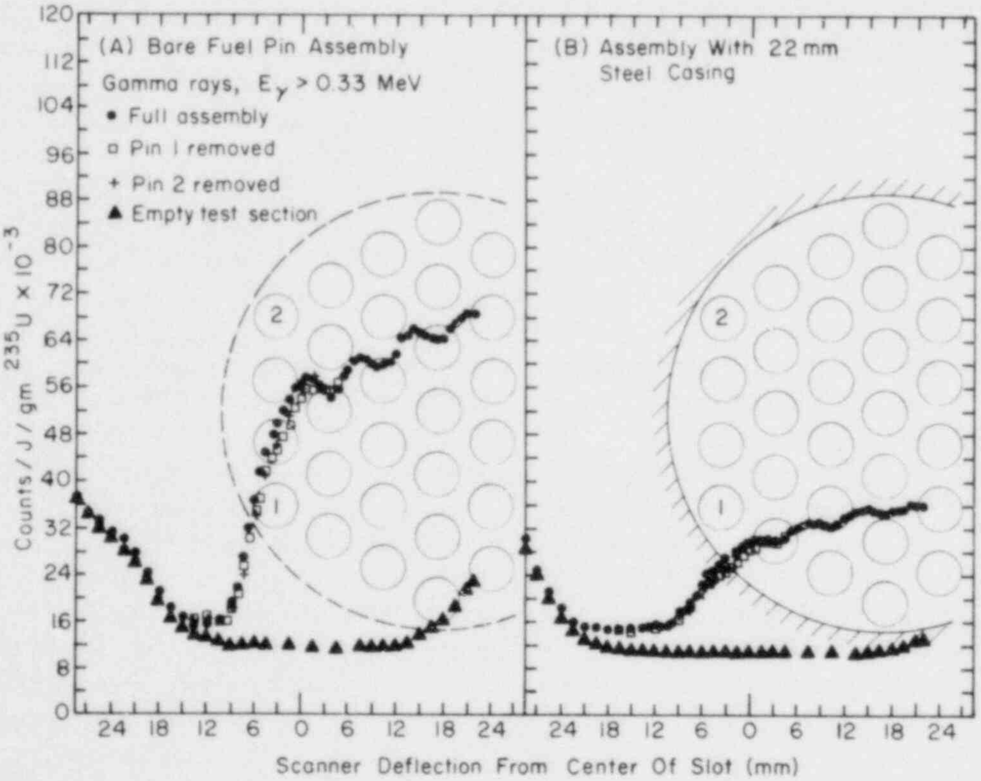

Fig. 64.
Across-corners gamma-ray scans with stilbene detectors of the off-center 37-pin assembly.

objects (other than the cladding itself). These objects include the collimator and the test capsule.

By moving the detector to one side of the collimator slot, it was determined that ~75% of the observed iron capture gamma rays originated in steel near the detector, that is, from capture of thermal neutrons in the steel of the collimator near the detector end. By using the 12.5-mm BGO detector, this high-energy background was reduced to about 23% of the total signal. It is apparent that, if one is to use a hodoscope collimator to obtain high-energy gamma-ray self-images, either the entire collimator should be shielded from thermal neutrons to reduce the production of iron capture gamma rays in the collimator, or the 20 cm or so of collimator closest to the detectors should be made of a high-density material with a low neutron-capture cross section, such as bismuth.

Test capsules for use in the upgraded TREAT reactor are expected to have steel walls with thicknesses of up to 45 mm. Thus, a collimator slot viewing a test assembly enclosed in such a capsule will also be viewing radiation from at least 90 mm of steel. The mass-removal coefficient for 7.6-MeV gamma rays in steel[23] is 0.030 cm^2/g, which is equivalent to a linear cross section of 0.236 cm^{-1}. The signal from steel in the test region will be attenuated by passage through the capsule to $\exp(-0.236 \times 4.5)$ or 35% of its original strength.

The steel capsule, however, not only attenuates the 7.6-MeV gamma-ray count rate from steel in the test region, but also contributes to the total 7.6-MeV count rate. If the steel capsule is regarded as a uniformly radiating source of 7.6-MeV gamma rays (and if absorption in the test assembly is ignored), the count rate R at the detector from gamma rays originating in the capsule is

$$R = \int_0^T s(x)\, e^{-\Sigma x}\, dx \quad , \tag{5}$$

where T is the length of the path through the steel jacket, s(x) is the 7.6-MeV gamma-ray source strength at position x, and Σ is the linear removal cross section for the gamma rays. The source strength term s(x) is of the form

$$s(x) = \rho(x) \int_0^\infty \phi(x,E)\, \sigma_c(E)\, dE \quad , \tag{6}$$

where $\phi(x,E)$ is the neutron flux of energy E at position x, $\sigma_c(E)$ is the radiative capture cross section of iron for neutrons of energy E, and $\rho(x)$ is the density of iron at position x. If one makes the simplifying assumptions that s(x) is constant and equal to S throughout the steel and that no other material is contributing to removal of the capture gamma rays, one may integrate Eq. 5 to obtain

$$R = (S/\Sigma)(1 - e^{-\Sigma T}) \quad , \tag{7}$$

which approaches a saturation value $R_0 = S/\Sigma$ for an infinite slab. Furthermore, the signal ΔR from a small additional thickness ΔT of steel in line with the collimator, as for instance in the test region, is $\Sigma R_0 \Delta T \exp(-\Sigma T)$. For a capsule with 4.5-cm-thick walls (total steel thickness of 9.0 cm), $R = 0.88\ R_0$ and $\Delta R/\Delta T = 0.028\ R_0\ cm^{-1}$. A 1-cm-thick clad blockage in the test assembly would therefore increase the number of 7.6-MeV gamma rays reaching the detector by only ~3%. Neutron flux depression through the test-section and capsule walls would be expected to reduce R_0 and hence the differential sensitivity even further.

To investigate the effect of neutron spectral shifts and flux depression within the test section, hodoscope iron capture gamma-ray intensities were calculated from 16-group ONETRAN calculations of the 37-pin assembly and steel capsule in PARKA. The calculated intensities are compared in Table IV with measurements of high-energy gamma rays from the test region with the collimator viewing various thicknesses of steel. The collimator viewed the center and the edge of the test assembly, first with only the test-section walls in place (total steel thicknesses of 11.2 and 12.7 mm) and then with the 21-mm-thick capsule in place (total steel thicknesses of 54 and 98 mm). Pulses from the 12.5-mm BGO detector corresponding to a gamma-ray energy interval of 6.2-8.1 MeV (with noncollimated background subtracted) were counted for 1000 s at a power level of 5 mW/g ^{235}U. The variation with steel thickness of the ratio of measured counts to the ONETRAN prediction shows that the nonlinearity of detected capture gamma rays is even greater than predicted by Eq. 5 with s(x) derived from the ONETRAN calculations. With the test assembly enclosed in a 45-mm-thick steel capsule, 1-cm-thick clad blockage would cause an increase in count rate of capture gamma rays of the order of only 1%.

TABLE IV

OBSERVED AND CALCULATED
7.6-MeV GAMMA RAYS FROM A 37-PIN ASSEMBLY
AND STEEL JACKET IN PARKA

Steel Thickness (mm)	Observed Net Counts in 1000 s	Calculated Relative Net Counts	Ratio of Observed to Net Counts
11.2	2507	446	5.62
12.7	2817	665	4.24
54	3443	897	3.84
98	4162	1267	3.28

G. Effect of Energy Selection on Gamma-Ray Imaging of Fuel

We have shown that self-images of fissioning fuel may be obtained with gamma-ray detectors. We have also found that the S/B ratio of such gamma-ray images can be enhanced by appropriate selection of the gamma-ray energy interval used to form the image. This is indicated in Fig. 65, which is derived from pulse-height distributions from across-flats scans with the 12.5-mm BGO detector of a 37-pin test assembly and of the empty test region, both with and without the 21-mm steel capsule. Photons with energies >3 MeV produce images with poorer S/B ratios than those with energies of 1-3 MeV. It is therefore desirable to use an upper-level, as well as a threshold, discriminator for imaging fuel motion with gamma-ray detectors. We also conclude that non-energy-dispersive detectors, such as gamma-sensitive fluors used for direct imaging of self-radiation from a test assembly, should, if possible, have an energy-dependent response tailored to maximum sensitivity in this energy range.

H. Summary

Table V is a summary of results obtained from hodoscope scans of various-sized test assemblies with a missing pin. The ability to detect one missing pin in a 127-pin assembly is established, but appears questionable for larger assemblies. It should be emphasized, moreover, that this static test of hodoscope resolution by no means establishes the feasibility of detecting the loss of this quantity of material from a test assembly under dynamic conditions, but rather establishes an upper performance limit for self-radiation-imaging systems.

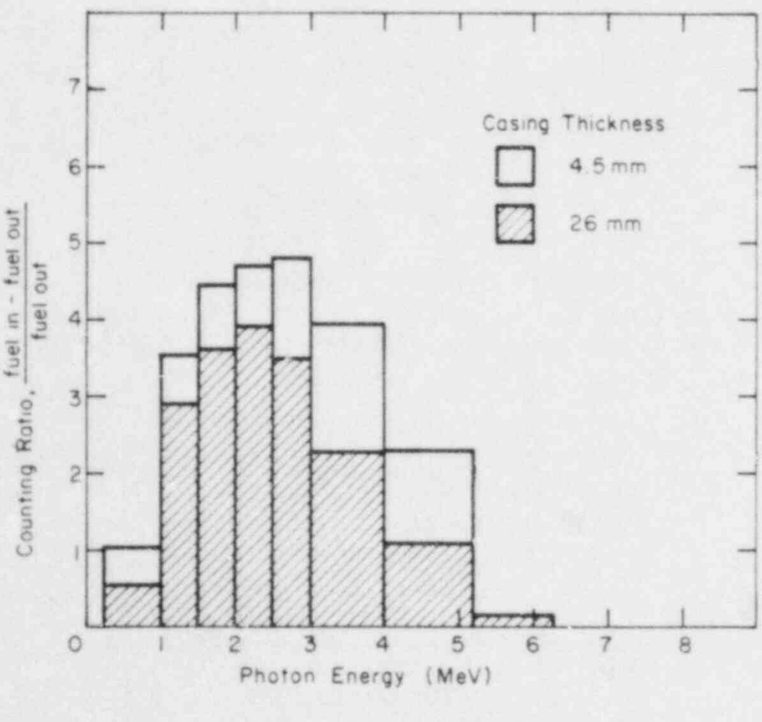

Fig. 65.
Gamma-ray S/B ratio for a 37-pin assembly as a function of detected energy.

TABLE V

FRACTIONAL DECREASE IN HODOSCOPE IMAGE INTENSITY
CAUSED BY CENTER VOID IN VARIOUS-SIZED TEST ASSEMBLIES

Number of Pins in Assembly	Fractional Decrease Caused by Center Void			
	$E_n > 1.3$ MeV	$E_n > 2.2$ MeV	$E_\gamma > 0.33$ MeV	$E_\gamma > 0.66$ MeV
1	0.33	0.43	0.45	0.54
37	0.054	0.070	0.046	0.059
91[a]	0.032	---	0.00	0.00
127	0.018	0.020	0.010	0.010

[a]91-pin EBR-II assembly.

V. CODED-APERTURE IMAGING STUDIES

Coded-aperture gamma-ray imaging of LMFBR fuel assemblies under test is being developed by SLA in conjunction with experiments to be performed at the ACRR. In support of this program, a coded-aperture imaging system designed and fabricated by SLA was installed in the PARKA shielded instrument-room wall in place of the hodoscope collimator. Top and side views of the installation are shown in Figs. 66 and 67. Images of a test assembly in PARKA are projected through the viewing slot and coded aperture onto x-ray film at the back of the aperture shield assembly.

Exposures of the 37-pin assembly were made using Eastman Kodak Co. type AA and XR-5 and E.I. DuPont De Nemours & Co. Cronex-2DC x-ray film with tantalum sheet and type TI-2 organic intensifiers. Films were machine-developed in the LASL Group M-1 x-ray laboratory.

The best quality photographs of Fresnel zone-plate images were obtained by exposing type AA film with type TI-2 screens for 10 000 s with the reactor operating at a power level of 1500 W. Inferior images, useful for setup purposes, could be obtained by exposing the Cronex-2DC film for 10-20 min with type TI-2 screens.

Lack of funding has caused suspension of the experiments, but the following conclusions were reached.

- PARKA can be used effectively as a driver reactor for static coded-aperture imaging experiments.
- A gamma-ray pinhole clearly images a 37-pin assembly in the presence of reactor background.
- Clear images of a 37-pin assembly have been reconstructed from shadowgrams made with an off-axis Fresnel zone-plate coded aperture.
- An exposure with a sheet of NE-102 plastic scintillator and Eastman Kodak Co. Tri-X film produced no image; this indicates that the bulk of radiation forming the coded-aperture images is gamma radiation, rather than neutrons.

Examples of pinhole images, Fresnel zone-plate shadowgrams, and reconstructed images of the 37-pin test assembly were exhibited at the 1979 American Nuclear Society-European Nuclear Society Meeting on Fast Reactor Safety Technology in Seattle, Washington.[24]

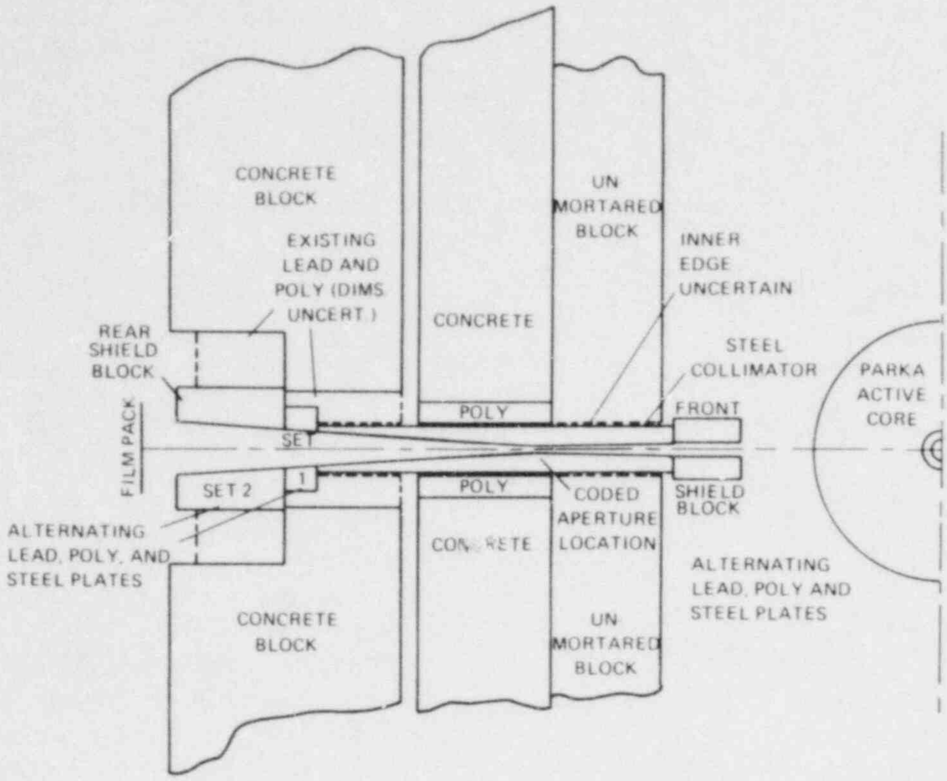

Fig. 66.
Top view of the SLA coded-aperture imaging system.

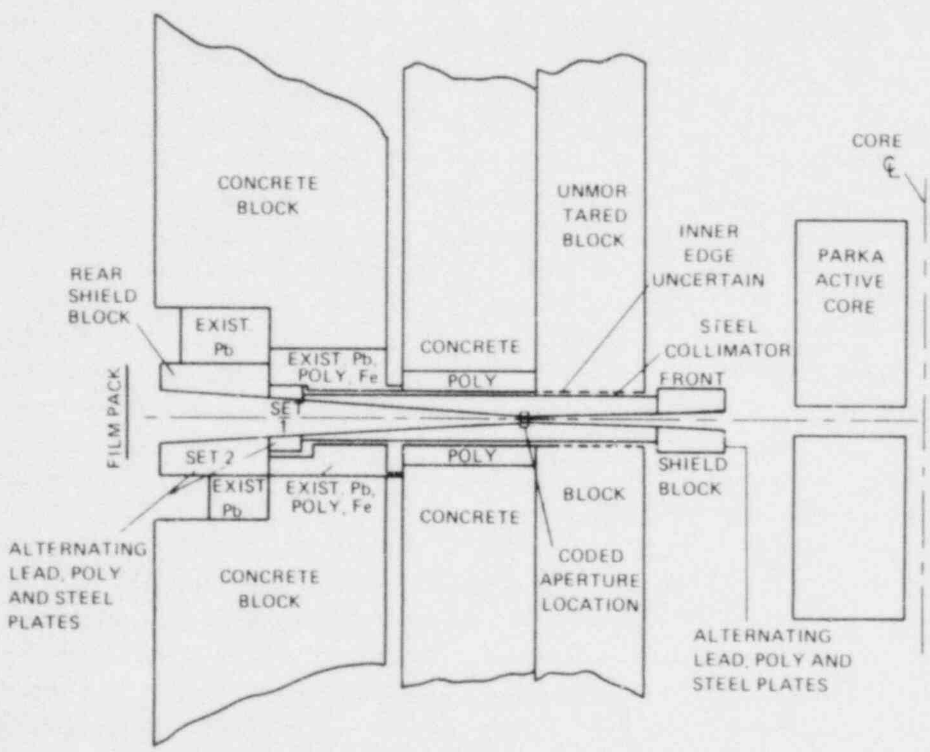

Fig. 67.
Side view of the SLA coded-aperture imaging system.

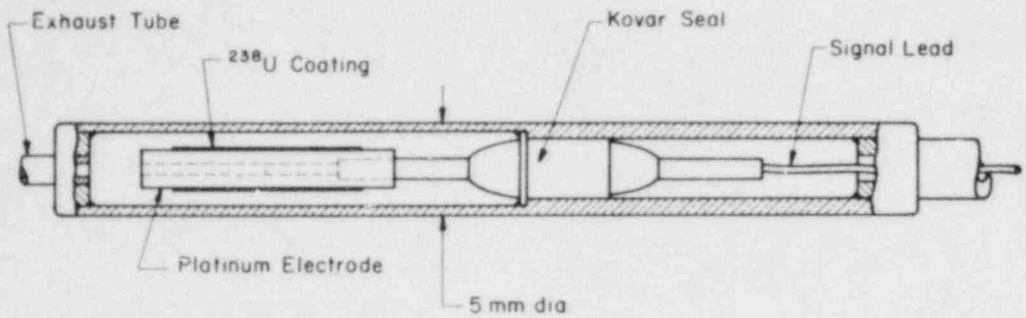

Fig. 68.
Cross-sectional view of a ^{238}U fission chamber used as an in-core detector. A detector of this type has also been used as an auxiliary power-level monitor for all hodoscope tests.

VI. IN-CORE DETECTOR STUDIES

PARKA has been used for studies of in-core detectors, in particular ^{235}U and ^{238}U fission chambers. These chambers, ~5 mm in diameter, were fit into the stainless-steel fuel-pin cladding. Figure 68 is a cross-sectional view of one of these detectors. The ^{238}U detector is sensitive to neutrons with energies above 1 MeV and thus responds primarily to neutrons from the test assembly. In contrast, the ^{235}U detector weights the lower-energy neutrons and is therefore more sensitive to neutrons leaking into the test assembly from the driver. As a result, removal of a fuel pin adjacent to a ^{238}U and a ^{235}U fission chamber produces an ~2% decrease in the count rate of the ^{238}U fission chamber and an increase of similar size in the count rate of the ^{235}U fission chamber.

The chambers, which were fabricated at LASL, were found to be extremely reliable, stable, and easy to make. Uranium-metal coatings of ~1 mg were evaporated onto the platinum anodes.* Most of the joints were soft-soldered, after the interior of the chamber was cleaned with abrasive and solvents. After assembly, the chambers were pumped out through a liquid-nitrogen trap to forepressure only, backfilled to 100 psig with a 90% argon-10% methane mixture, and sealed off. One chamber was prepared with an anode bearing ^{252}Cf to facilitate testing the characteristics of the fission chambers and associated electronics.

The chambers are operated at 200 V. Signals are fed at the reactor to a preamplifier of LASL design (model 224 QN) and then to a Radiation Instrument Development Laboratories (RIDL) model 27001 amplifier. The output of the amplifier is fed through 300 m of RG63/U cable to a RIDL model 27501 discriminator in the control room.

A pulse-height distribution from one of the ^{238}U fission chambers is shown in Fig. 69. The two-humped fission-fragment portion of the distribution provides a convenient check on the performance of the detector and associated electronics. For counting, the discriminator was set at the minimum between the fission distribution and the low-energy alpha and noise pulses, at the point indicated by the cursor. This particular chamber has been used for three years as a monitor of reactor power without noticeable deterioration in performance.

Measurements on a 37-pin assembly were made with the fission chambers located in an empty fuel-pin casing that replaced the center fuel pin. Detector response was determined as fuel pins were removed from each of the three hexagonal rings of pins surrounding the detectors. The results summarized in Table VI show that counts from the ^{238}U detector decrease as the fuel pins are removed, whereas counts from the ^{235}U detector increase. The ^{235}U/^{238}U count-rate ratio is a more sensitive measure of fuel loss than is the count rate of either detector separately. For these experiments, entire fuel pins were removed; it is expected, however, that similar results would be obtained if short lengths were removed in the vicinity of the 10-mm-active-length fission detectors.

Figure 70 shows the response of fission chambers located at the center of the 37-pin assembly as fuel pins are removed progressively from the inside toward the outside. As pins are removed, both detector responses change by almost a factor of 2. For a true fast driver, however, it should be noted that the diagnostic capability of in-core fission detectors would be limited because there would be little change in the neutron spectrum, and

*We are grateful to John Povelites of LASL Group CNC-11 for preparation of these films.

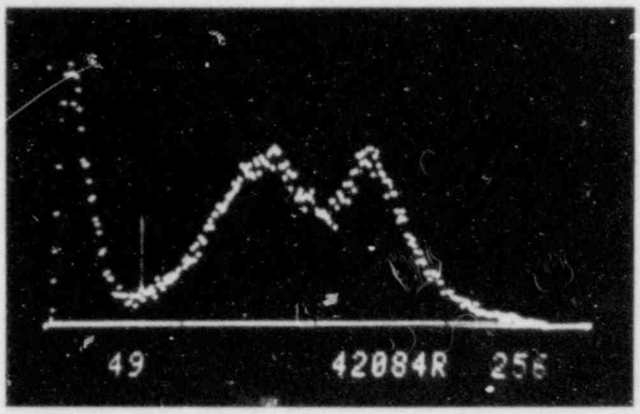

Fig. 69.
Pulse-height distribution from the ^{238}U fission chamber.

TABLE VI

IN-CORE DETECTOR RESPONSE TO FUEL-PIN REMOVAL

Pins Removed	Relative Response		
	^{235}U Detector	^{238}U Detector	^{235}U/^{238}U Ratio[a]
Center pin	1.000	1.000	1.000
Center pin and six pins from inner ring	1.098	0.892	1.23
Center pin and six pins from middle ring	1.093	0.928	1.18
Center pin and six pins from outer ring	1.058	0.970	6.9

[a]The absolute magnitudes of the ^{235}U and ^{238}U detector responses are accurate to only ±20% since the masses of the fission-chamber coatings are not accurately known.

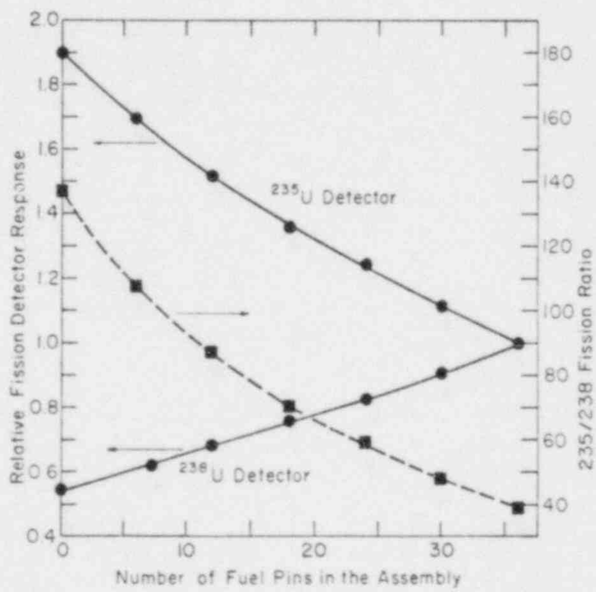

Fig. 70.
In-core detector response to fuel-pin removal from a 37-pin test assembly.

POOR ORIGINAL

TABLE VII

IN-CORE DETECTOR RESPONSE TO REMOVAL OF COMPLETE FUEL-PIN RINGS

Pins Removed	Relative Response		
	^{235}U Detector	^{238}U Detector	$^{235}U/^{238}U$ Ratio[a]
Center pin	1	1	39
Center pin and inner 6-pin ring	1.12	0.88	50
Center pin and inner 12-pin ring	1.17	0.86	53
Center pin and inner 18-pin ring	1.12	0.89	49

[a]The absolute magnitudes of the ^{235}U and ^{238}U detector responses are accurate to only $\pm 20\%$ since the masses of the fission-chamber coatings are not accurately known.

hence little difference between the ^{235}U and ^{238}U response, as fuel pins are removed.

Table VII shows the response of the centrally located fission chambers to removal of complete rings of fuel pins. The first ring contains 6 pins, the second 12, and the outside ring 18 pins. The fact that the fission chamber responses are relatively constant for these three changes indicates that the filtering effect of a complete ring of pins is independent of the diameter of the ring.

Our results indicate that in-core detectors can provide diagnostic information in multipin STF tests. It has been proposed that one or more fuel pins be replaced with "hardened" channels enclosing a line of alternate ^{235}U and ^{238}U fission chambers cooled by flowing argon gas. The ^{235}U detectors would monitor the local neutron flux driving the fuel pins and the ^{238}U detectors would sense the proximity of fuel. For the high power levels encountered in STF tests, it would be preferable to measure ion-current signals as a function of time rather than count rates.

VII. TRANSIENT OPERATION OF PARKA

The hodoscope scans and in-core detector tests were characterized by long count times with PARKA operating at low power. Such an operating mode, which may be adequate for testing concepts involving nuclear counting instruments, is not satisfactory for imaging experiments involving such concepts as the use of coded apertures. Almost by accident, we learned that PARKA might be used as a high-level, short-duration source. It was found that a single burst of Godiva, a prompt-burst reactor housed in the same experimental area as PARKA, induced radiation levels in PARKA comparable to those induced by a calibration run of PARKA for 10 min at 55 W. As a consequence, we became interested in the possibility of intentionally pulsing a subcritical PARKA with Godiva to induce short, intense transients in a test assembly without operating PARKA in a supercritical mode. Experiments were initiated to investigate the potential of this technique.

PARKA power had been calibrated by measuring the core fission distribution with uranium-aluminum flux wires and then determining an absolute value of fissions/g ^{235}U at one point in the core for some desired operating level and time. Standard procedures exist at the facility for this type of calibration. From these measurements it was determined that normal operating power for hodoscope scans wtih Hornyak Buttons is 550 W and that a typical Godiva burst resulted in an energy release of 30 kJ in PARKA.

Bursts with Godiva were made at two distances from PARKA and at two PARKA reactivities. Flux-wire activations at the center of Godiva were compared with those at the test-assembly center and in the PARKA core for each burst. Table VIII lists the relative fissions/g ^{235}U for these locations.

As expected, the variation of PARKA yield with distance from Godiva is seen to be less than the inverse-square law, because of the contribution from room-scattered neutrons. The yield varies inversely with the subcritical reactivity. Presumably the prompt yield during the short part of the transient varies inversely with

TABLE VIII

PARKA YIELDS FROM GODIVA BURSTS

Location	Relative Yield (fissions/g ^{235}U) PARKA reactivity = −5.7 \$ and PARKA-Godiva separation = 5.5 m	PARKA reactivity = −5.7 \$ and PARKA-Godiva separation = 2.3 m	PARKA reactivity = −3.6 \$ and PARKA-Godiva separation = 2.3 m
Godiva center	1.00	1.00	1.00
Test-assembly center	0.0043	0.014	0.023
PARKA core	0.0078	0.026	0.045

the reactivity interval from prompt-critical. This behavior is consistent with a PARKA pulse having a sharp leading edge followed by the equilibrium-mode prompt-neutron decay. Pulse shapes plotted in Fig. 71 show this to be the case except for an initial transient. These curves were obtained with a fission chamber located in the PARKA core and operated in the current mode.

PARKA kinetics are well known from measurements and calculations on PARKA and on similar systems during the Rover program. Prompt-neutron decay measurements on PARKA with the Rossi-α technique give a value of 40 μs for neutron mean lifetime τ. The computed effective delayed-neutron fraction γβ is 0.0074. Thus, the prompt-neutron decay constant at delayed critical α_{DC} is given by

$$\alpha_{DC} = -(1 - K_p)/\tau = \gamma\beta/\tau = -185\ s^{-1} \quad . \quad (8)$$

where K_p is the prompt-neutron multiplication factor. At other subcritical reactivities the decay constant is given by

$$\alpha = \alpha_{DC}\Delta K_p \quad , \quad (9)$$

where ΔK_p is the reactivity interval from prompt critical. For the PARKA reactivities at which the measurements were made, −5.7 and −3.6 \$, we obtain values for α of −1240 and −850 s^{-1}, respectively. Following initial transients, the equilibrium decay of PARKA then varies as $e^{\alpha t}$.

The actual magnitude of fissions/g ^{235}U in the test assembly at a separation of 2.3 m and a reactivity of −3.6 \$ is 1.4×10^{10}. This yield can be increased to 10^{11} fissions/g ^{235}U by operating Godiva closer to PARKA and at higher intensity. Of this yield, 8×10^{10} fissions/g

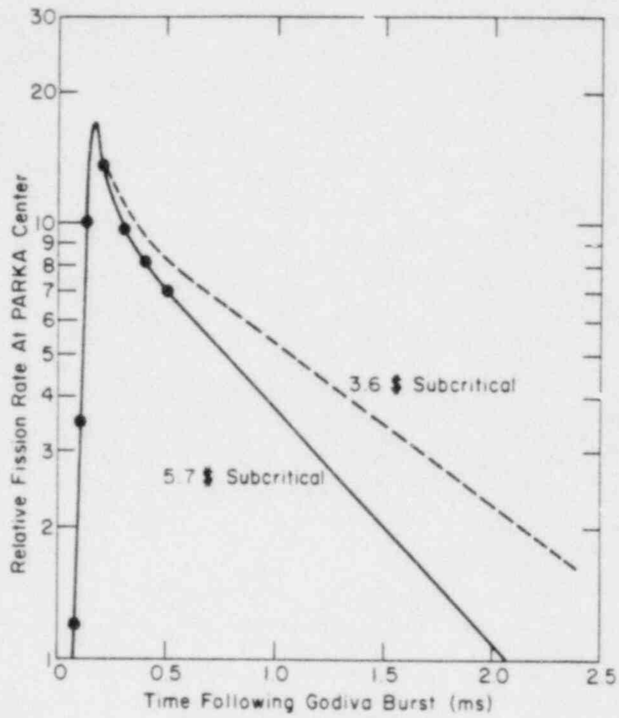

Fig. 71.
PARKA response to Godiva bursts at two different PARKA reactivities.

^{235}U is under the prompt-neutron pulse and 5×10^{10} fissions/g ^{235}U occurs in the first millisecond, corresponding to an average power density during this interval of 1.5 kW/g ^{235}U at the center of the test assembly. Increasing the PARKA reactivity increases the total energy under the prompt spike as its width increases but has little effect on the peak value of the power. In any event, it is feasible to stretch pulses to widths of ~10 ms by increasing PARKA reactivity. The peak power in small test assemblies can be increased by a factor of 10 to 15 kW/g ^{235}U by enclosing the assembly in a polyethylene flux trap at the center of PARKA.

To obtain more information about the response of PARKA to external pulses, we substituted a portable pulsed neutron source for Godiva. Here, a single Godiva pulse of near-fission-spectrum neutrons is replaced by many smaller pulses, shorter by an order of magnitude, of 14 MeV neutrons. The 14-MeV neutrons produce a somewhat different intial fission distribution in PARKA and hence, in principle, a different initial transient. The reactivity of PARKA was changed by adjusting the control rods rather than the number of graphite shim rods as in the measurements with Godiva bursts. In proposed diagnostic experiments, PARKA reactivity would be adjusted with the control rods.

The prompt-neutron-chain decay was measured by collecting counts in sequential time channels following each pulse from the nturon generator. The neutron detector, a BF_3 proportional counter, was located at the center of an array of 30 fuel pins (a 37-pin assembly with 7 center pins removed). Counting data are plotted in Fig. 72 for PARKA at delayed critical and at 1.8 \$ and 5.2 \$ below critical. To avoid a continuous increase in PARKA power during the measurements at delayed critical, pulsing was interrupted periodically and PARKA was taken subcritical to allow decay of the delayed neutrons. Counts resulting from the average power level are subtracted as background.

According to Eqs. 8 and 9, the prompt neutron decay constant α should vary linearly with the reactivity interval from prompt critical Δk_p, provided the neutron lifetime remains constant at the different reactivities. For PARKA, changing the position of boron vanes in the beryllium reflector does change the neutron lifetime significantly; therefore, α does not vary linearly with Δk_p Values for α observed here should be more precise than those predicted above. It is not expected that the decay of a PARKA pulse induced by a Godiva burst will differ from the decays shown in Fig. 72 except for the initial transient.

These pulsing experiments have established that (1) the initial PARKA pulse amplitude is independent of PARKA reactivity, (2) the total yield under the prompt-neutron pulse varies as $1/\alpha$ except for a small initial transient effect, (3) peak power levels in the test assembly as high as 10 kW/g ^{235}U can be attained by using maximum Godiva pulses and a flux trap around the assembly, and (4) the width of the PARKA pulses is in the range 1-10 ms. These pulses would be useful for transient testing of hodoscopes and for evaluation of coded-aperture techniques under realistic STF conditions.

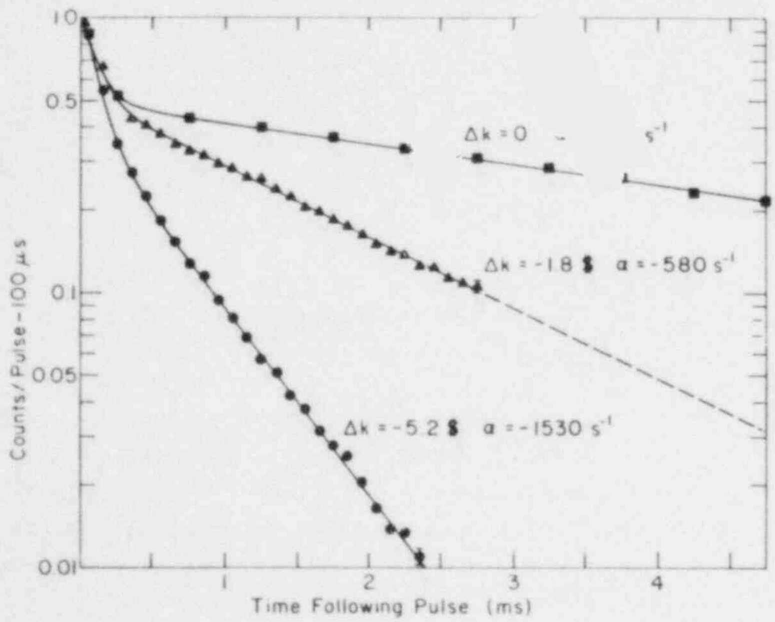

Fig. 72.
Decay of PARKA prompt neutrons induced by pulses from a 14-MeV neutron generator.

ACKNOWLEDGMENTS

The authors wish to thank the members of the LASL Critical Experiments and Diagnostics Group who contributed to this project, included A. R. Brown, C. C. Byers, M. B. Diaz, E. O. Ferdinand, G. E. Hansen, B. Peña, E. A. Plassman, R. L. White, R. E. Malenfant, and W. L. Talbert, Jr. We also wish to thank A. DeVolpi, C. L. Fink, and E. Rhodes of Argonne National Laboratory for many helpful discussions. The coded-aperture experiment at PARKA was planned by and executed under the direction of David A. McArthur of Sandia Laboratories, Albuquerque. Computer programming was accomplished by H. M. Forehand and B. Wilson. Test fuel pins were fabricated by LASL Group CMB-6 under supervision of Keith Davidson. We are also grateful to Donald G. Simons of the US Naval Surface Weapons Facility for the loan of the tantalum nitride target used for detector testing.

REFERENCES

1. G. I. Bell, J. E. Boudreau, T. McLaughlin, R. G. Palmer, V. Starkovich, W. E. Stein, M. G. Stevenson, and J. L. Yarnell, "Preliminary Report. Study of Fast Reactor Safety Test Facilities," Los Alamos Scientific Laboratory report LA-5978-MS (May 1975).

2. R. Avery *et al*, "Report on Experiment Needs and Facilities Study," Argonne National Laboratory report ANL/RAS 76-22 (September 1976).

3. H. U. Wider, M. G. Stevenson, and D. A. McArthur, "Material Diagnostic Requirements for STF," presentation at the Nuclear Energy Agency Specialists' Meeting on Fuel- and Clad-Motion Diagnostics for Fast Reactor Safety Test Facilities, Los Alamos, New Mexico, December 5-7, 1977 (unpublished).

4. W. E. Stein, V. Starkovich, and J. D. Orndoff, "X-Ray Monitoring of Fuel Motion," in "Transactions of the Second Technical Exchange Meeting on Fuel- and Clad-Motion Diagnostics for LMFBR Safety Test Facilities," Argonne National Laboratory report ANL/RAS 76-34 (1976).

5. G. J. Berzins and K. S. Han, "Pinhole Imaging of a Test Fuel Element at the Transient Reactor Test Facility," Nucl. Sci. Eng. **65**, 28-40 (1978).

6. J. G. Kelly and K. T. Stalker, "ACPR Upgrade Fuel-Motion Detection System" in "Transactions of the Second Technical Exchange Meeting on Fuel- and Clad-Motion Diagnostics for LMFBR Safety Test Facilities," Argonne National Laboratory report ANL/RAS 76-34 (1976).

7. S. A. Wright and S. A. Dupree, "In-Core Fuel-Motion Detection for Large Scale Tests," in "Transactions of the Second Technical Exchange Meeting on Fuel- and Clad-Motion Diagnostics for LMFBR Safety Test Facilities," Argonne National Laboratory report ANL/RAS 76-34 (1976).

8. A. DeVolpi, R. J. Pecina, R. T. Daly, D. J. Travis, R. R. Stewart, and E. A. Rhodes, "Fast-Neutron Hodoscope at TREAT: Development and Operation," Nucl. Technol. **27**, 449 (1975).

9. "Results of Fast Reactor Fuel Pin Inspection by Acoustical Holography," Final Report (March 15, 1977) LASL Contract LG7-42560-1, Holosonics, Inc., 2400 Stevens Drive, Richland, WA 95352 (unpublished).

10. T. R. Hill, "ONETRAN: A Discrete Ordinates Finite Element Code for the Solution of the One-Dimensional Multigroup Transport Equation," Los Alamos Scientific Laboratory report LA-5990-MS (June 1975).

11. W. F. Hornyak, "A Fast Neutron Detector," Rev. Sci. Instrum., **23**, No. 6, 264 (1952).

12. H. O. Menlove, R. A. Forster, R. H. Augustson, A. E. Evans, and R. B. Walton, "Characteristics of ^{4}He Gas Tubes for Fast-Neutron Detection," in "Nuclear Safeguards Research and Development Program Status Report, September-December 1970," Los Alamos Scientific Laboratory report LA-4605-MS (January 1971) p. 13.

13. F. D. Brooks, "A Scintillation Counter With Neutron and Gamma-Ray Discriminators," Nucl. Instrum. Methods, **4**, 151 (1959).

14. L. V. East and R. B. Walton, "Polyethylene Moderated ^{3}He Neutron Detectors," Nucl. Instrum. Methods, **72**, 161 (1969).

15. C. D. Swartz and G. E. Owen, "Recoil Detection in Scintillators," in *Fast Neutron Physics, Part I*, J. B. Marion and J. L. Fowler, Eds. (Interscience Publishers, New York, 1960).

16. C. L. Fink, A. DeVolpi, and G. Stanford, "Advances in Clad Blockage Detection," in "Transactions of the Second Technical Exchange Meeting on Fuel- and Clad-Motion Diagnostics for LMFBR Safety Test Facilities," Argonne National Laboratory report ANL/RAS 76-34 (1976).

17. O. H. Nestor and C. Y. Huang, "Bismuth Germanate: A High-Z Gamma-Ray and Charged-Particle Detector," IEEE Trans. Nucl. Sci., **NS-22**, 68-71 (February 1975).

18. A. E. Evans, B. Brown, and J. B. Marion, "Study of the $^{14}N(p,\gamma)^{15}O$ Reaction," Phys. Rev., **149**, 863-879 (1966).

19. L. V. Groshev, A. M. Demidov, L. N. Lutsenko, and V. I. Pelekhov, *Atlas of Gamma-Ray Spectra from Radiative Capture of Thermal Neutrons* (Pergamon Press, Inc., London, 1959), p. 82.

20. C. L. Fink, R. P. Hosteny, A. DeVolpi, E. A. Rhodes, and A. E. Evans, "Analysis of the 91-Pin Subassembly Tests at PARKA," presentation at the Nuclear Energy Agency Specialists' Meeting on Fuel- and Clad-Motion Diagnostics for Fast Reactor Safety Test Facilities, Los Alamos, New Mexico, December 5-7, 1977 (unpublished). ANL CONF. 91A |100,100| 10:49:12 (26 September 1977).

21. A. DeVolpi, C. L. Fink, E. A. Rhodes, R. Hosteny, H. V. Rhude, R. E. Boyar, L. J. Duncan, and A. E. Evans, "Fuel Displacement Diagnostics for a 91-Pin Subassembly," Trans. Am. Nucl. Soc., **28**, 499 (June 1978).

22. C. L. Fink, A. DeVolpi, E. A. Rhodes, and A. E. Evans, "Hodoscope Performance Tests on a 91-Pin Fuel Bundle at PARKA," IEEE Trans. Nucl. Sci., **NS-26**, No. 1, 827 (February 1979).

23. G. W. Grodstein, "X-Ray Attenuation Coefficients from 10 keV to 10 MeV," National Bureau of Standards circular 583 (1957), p. 37.

24. J. G. Kelly, K. T. Stalker, D. A. McArthur, K. W. Cha, and J. E. Powell, "Theory and Application of the Coded-Aperture Fuel-Motion Detection System," in "Proceedings of the International Meeting on Fast Reactor Safety Technology," Seattle, Washington, August 19-23, 1979 (American Nuclear Society, LaGrange Park, Illinois, 1979) Vol. V, p. 2302.

APPENDIX

PUBLICATIONS AND PRESENTATIONS OF WORK COVERED BY THIS REPORT

1. John Orndoff, "Simulation of LMFBR Test Facility Conditions with LASL Critical Assemblies," presentation at the Information Exchange Meeting on Fuel- and Clad-Motion Diagnostics in LMFBR Safety Test Facilities, sponsored by Sandia Laboratories, Albuquerque, New Mexico, November 11-12, 1975 (unpublished). LA-UR-75-2212.

2. John Orndoff and A. E. Evans, "STF Simulation with PARKA and Application to Diagnostic Instrumentation Evaluation," in "Transactions of the Second Technical Exchange Meeting on Fuel- and Clad-Motion Diagnostics in LMFBR Safety Test Facilities," Argonne National Laboratory report ANL/RAS 76-34 (1976).

3. A. E. Evans, J. D. Orndoff, and W. L. Talbert, Jr., "STF Diagnostic Instrumentation Evaluation with PARKA," presentation at the Nuclear Energy Agency Specialists' Meeting on Fuel- and Clad-Motion Diagnostics for Fast Reactor Safety Test Facilities, Los Alamos, New Mexico, December 5-7, 1977 (unpublished). LA-UR-77-2712.

4. C. L. Fink, R. P. Hosteny, A. DeVolpi, E. A. Rhodes, and A. E. Evans, "Analysis of the 91-Pin Subassembly at PARKA," presentation at the Nuclear Energy Agency Specialists' Meeting of Fuel- and Clad-Motion Diagnostics for Fast Reactor Safety Test Facilities, Los Alamos, New Mexico, December 5-7, 1977 (unpublished), ANL CONF. 91A [100,100] 10:49:12 (26 September 1977).

5. A. DeVolpi, C. L. Fink, E. A. Rhodes, R. Hosteny, H. V. Rhude, R. E. Boyar, L. J. Duncan, A. E. Evans, and J. Barton, "Fuel Displacement Diagnostics for a 91-Pin Subassembly," Trans. Am. Nucl. Soc. **28**, 499 (June 1978).

6. A. E. Evans, J. D. Orndoff, and W. L. Talbert, "Evaluation of LMFBR Fuel-Motion Diagnostics with PARKA," IEEE Trans. Nucl. Sci. **NS-26**, No. 1, 815 (February 1979).

7. A. E. Evans, J. D. Orndoff, and W. L. Talbert, "Evaluation of Hodoscopes for Fuel-Motion Measurement in Multipin Bundles," Trans. Am. Nucl. Soc. **30**, 465 (November 1978).

8. A. E. Evans and J. D. Orndoff, "Progress in Fuel-Motion Diagnostics Instrumentation at PARKA," in "Proceedings of the International Meeting on Fast Reactor Safety Technology," Seattle, Washington, August 19-23, 1979 (American Nuclear Society, LaGrange Park, Illinois, 1979) Vol. V, p. 2225.

9. A. E. Evans, "Gamma-Ray Response of a 38-mm Bismuth Germanate Scintillator," IEEE Trans. Nucl. Sci. **NS-27**, No. 1, 172 (February 1980).

10. A. E. Evans, "Application of Bismuth Germanate Scintillators to Detection of High-Energy Gamma Radiation," Trans. Am. Nucl. Sci. **33**, 693 (1979).

11. J. G. Kelly, K. T. Stalker, D. A. McArthur, K. W. Cha, and J. E. Powell, "Theory and Application of the Coded-Aperture Fuel-Motion Detection System," in "Proceedings of the International Meeting on Fast Reactor Safety Technology," Seattle, Washington, August 19-23, 1979 (American Nuclear Society, LaGrange Park, Illinois, 1979) Vol. V, p. 2302.

DISTRIBUTION

Nuclear Regulatory Commission, Bethesda, Maryland, R7	380
Technical Information Center, Oak Ridge, Tennessee	2
Los Alamos Scientific Laboratory, Los Alamos, New Mexico	50
Special Distribution	480

Special Distribution List

Argonne National Laboratory
Argonne, Illinois
Attn: David Rose, RAS
Alex DeVolpi, RAS
Charles Fink, RAS
Ed Rhodes, RAS
G. Stanford, RAS
R. Avery
R. J. Pecina
R. T. Daly
D. J. Travis
R. R. Stewart
R. P. Hosteny
S. A. Cox
L. W. Person
A. Klickman
P. Bertoncini
N. Lapinski

University of Maryland
Department of Physics
College Park, Maryland
Attn: W. F. Hornyak
Jerry B. Marion

Harshaw Chemical Co.
Crystal & Electronic Products Dept.
6801 Cochran Road
Solon, OH 44139
Attn: M. R. Farukhi
O. H. Nestor
C. Y. Huang

Sandia Laboratories
Albuquerque, New Mexico
Attn: James E. Powell
David A. MacArthur
J. G. Kelly
S. A. Wright
K. T. Stalker
S. A. Dupree
K. W. Cna
L. M. Choote
L. D. Posey
P. J. McDamal

US Naval Surface Weapons Center
White Oak, Silver Spring, MD 20910
Attn: Donald G. Simons, R-41

Nuclear Enterprises, Inc.
935 Terminal Way
San Carlos, CA 94070

University of Washington
Department of Nuclear Engineering
Seattle, Washington
Attn: Gene L. Woodruff
R. W. Albrecht

Electric Power Research Institute
3412 Hillgrove Ave.
Palo Alto, CA 94303
Attn: Walter B. Loewenstein

Hittman Nuclear & Development Corp.
9190 Red Branch Rd
Columbia, MD 21045
Attn: Fred Hittman

Canberra Industries, Inc.
45 Gracey Avenue
Meriden, CT 06450
Attn: L. V. East

Reuter-Stokes, Inc.
18530 South Miles Parkway
Warrensville Heights
Cleveland, OH 44128
Attn: Thomas Flemming
Joseph Skarupa

Science Applications, Inc.
1211 W. 22nd Street
Oak Brook, IL 60521
Attn: R. S. May

IRT Corporation
7650 Convoy Court
San Diego, California
Attn: John Barton
Richard L. Bramblett

Kernforschungszentrum Karlsruhe
Postfach 3640, D-7500
Karlsruhe, GERMANY
Attn: Kalus Böhnel
H. Blum

General Electric Co.
P. O. Box 780 M/C K-51
Wilmington, NC 28401
Attn: F. C. Schoenig, Jr.

Science Applications, Inc.
2680 Hanover Street
Palo Alto, CA 94303
Attn: T. Gozani

University of New Mexico
Department of Nuclear Engineering
Albuquerque, NM 87131
Attn: R. A. Knief

☆ U.S. GOVERNMENT PRINTING OFFICE: 1980—777-022/194